technische universität
dortmund

Arbeit zur Erlangung des akademischen Grades
Doktor der Naturwissenschaften

Studies of single top-quark production in association with a photon under updated reconstruction conditions at the ATLAS experiment

Nils Julius Abicht
geboren in Hamburg

2026

Arbeitsgruppe Kröninger
Fakultät Physik
Technische Universität Dortmund

Dissertation veröffentlicht in der Fakultät Physik der Technischen Universität Dortmund.

Erstgutachten:	Prof. Dr. Kevin A. Kröninger
Zweitgutachten:	Dr. Chris M. Delitzsch
Vorsitz der Prüfungskommision:	Prof. Dr. Christoph Lange
Vertretung der wiss. Mitarbeitenden:	Dr. Jörg Debus
Datum des Einreichens der Arbeit:	23. April 2026
Datum der mündlichen Prüfung:	09. Juli 2026

Abstract

This thesis presents studies of single top-quark production in association with a photon ($tq\gamma$), using $140\,\mathrm{fb}^{-1}$ of proton-proton collision data at a center-of-mass energy of 13 TeV, recorded by the ATLAS detector at the Large Hadron Collider during Run 2. With a predicted cross-section of the order of one picobarn, this process is among the rarest top-quark processes in the Standard Model and provides a direct probe of the electroweak coupling between the top quark and the photon. The inclusive $tq\gamma$ cross-section has previously been measured by the ATLAS collaboration and was found to be larger than the theoretical prediction, motivating further investigation. Essential components of the previous ATLAS measurement are revisited under updated reconstruction and software conditions. A dedicated signal modeling method is employed, combining next-to-leading-order Monte Carlo samples to consistently describe photon radiation in both the production and decay of the top quark. Background contributions from processes with misidentified or non-prompt photons are estimated using data-driven techniques. A Neural Network is trained to select a high-purity signal-enriched sample, enabling the study of the kinematic properties of the process. The resulting distributions are found to be in good agreement with theoretical predictions within the statistical uncertainties. The work presented in this thesis provides the foundation for a future differential cross-section measurement of single top-quark production in association with a photon.

Kurzfassung

Diese Arbeit präsentiert Studien zur Produktion einzelner Top-Quarks in Verbindung mit einem Photon ($tq\gamma$), basierend auf $140\,\mathrm{fb}^{-1}$ an Proton-Proton-Kollisionen bei einer Schwerpunktsenergie von 13 TeV, aufgezeichnet mit dem ATLAS-Detektor am Large Hadron Collider während Run 2. Mit einem Wirkungsquerschnitt der Größenordnung eines Pikobarn gehört dieser Prozess zu den seltensten Top-Quark-Prozessen im Standardmodell und erlaubt eine direkte Messung der elektroschwachen Kopplung zwischen Top-Quark und Photon. Der inklusive $tq\gamma$-Wirkungsquerschnitt wurde bereits von der ATLAS-Kollaboration gemessen und lag über der theoretischen Vorhersage, was weitere Untersuchungen motiviert. Wesentliche Bestandteile der vorherigen ATLAS-Messung werden unter aktualisierten Rekonstruktions- und Softwarebedingungen überarbeitet. Für das Signal-Sample wird eine spezielle Methode angewendet, bei der next-to-leading-order Monte-Carlo-Samples kombiniert werden, um die Abstrahlung von Photonen sowohl während der Produktion als auch während des Zerfalls des Top-Quarks konsistent zu beschreiben. Hintergrundbeiträge aus Prozessen mit falsch identifizierten oder nicht-prompten Photonen werden mittels datenbasierter Methoden abgeschätzt. Ein Neuronales Netz wird trainiert, um eine signalangereicherte Stichprobe zu selektieren, wodurch die Untersuchung der kinematischen Eigenschaften des Prozesses ermöglicht wird. Die resultierenden Verteilungen stimmen innerhalb der statistischen Unsicherheiten mit den theoretischen Vorhersagen überein. Die in dieser Arbeit präsentierten Ergebnisse bilden die Grundlage für eine zukünftige differentielle Wirkungsquerschnittsmessung der Produktion einzelner Top-Quarks in Verbindung mit einem Photon.

Contribution of the Author

The author contributed to the measurement of the photon identification efficiency within the ATLAS experiment. For this, the author updated the existing Matrix Method code for new reconstruction and software conditions, performed extensive validation, and resolved issues with the relevant derivation samples, leading to updated Run 2 recommendations. Additionally, the author maintained and updated the HGamSinglePhoton framework and relevant components of the HGamCore framework, and was responsible for producing photon-plus-jet and dijet Monte Carlo samples for the working group. For one year, the author also served as liaison between the ATLAS EGamma and Top Quark working groups, managing inter-group communication and fulfilling various software and analysis requests.

The analysis for the differential measurement of single top-quark production in association with a photon was carried out jointly by a small analysis team. The responsibilities were divided as follows:

- The author: signal modeling, signal stitching, estimation of $h \to \gamma$ fake backgrounds
- Lucas Cremer: estimation of $e \to \gamma$ fake backgrounds, Neural Network classifier, unfolding procedure
- Marina Andreß: contributions to Neural Network classifier, Graph Neural Networks studies

Contents

1 Introduction

Understanding the fundamental laws of nature is one of the central goals of particle physics. To achieve this, mathematical theories for the elementary particles and their interactions are formulated. These theories make predictions that can be tested in experiments. The agreement between experimental observations and theory determines whether a model is supported, needs to be refined, or must be replaced.

One of the most successful of these theories is the Standard Model (SM) of particle physics [1–3], which is a relativistic quantum field theory. It describes all known elementary particles and the electromagnetic, weak, and strong interactions. Many of its predictions, including the existence of additional quark generations such as the bottom quark, first observed via the Υ resonance [4], as well as the Higgs boson [5, 6], have been confirmed experimentally. The SM provides quantitatively precise predictions for a wide range of observables, and these predictions agree with experimental data at a remarkable level of precision [7].

Despite its success, the SM is incomplete. For example, it cannot explain the nature of dark matter or dark energy [8], it provides no mechanism for the observed matter-antimatter asymmetry [9], and it fails to incorporate gravity. These shortcomings motivate the search for physics beyond the Standard Model (BSM). BSM physics could appear in the form of new particles or new interactions, or through significant deviations from precise SM predictions.

Testing the SM predictions and probing for deviations requires the study of high-energy particle collisions, which are provided by accelerator facilities such as the Large Hadron Collider (LHC), located at the CERN laboratory. The LHC is currently the highest-energy particle collider ever constructed. During the data-taking period between 2015 and 2018 (Run 2), the LHC collided protons at a center-of-mass energy of 13 TeV, which has been increased to 13.6 TeV in the ongoing Run 3. Higher collision energy increases the reach for the production of potential new heavy particles and enhances the production rates of rare SM processes. During Run 2, the ATLAS experiment, one of the four major detectors at the LHC, recorded the 140 fb^{-1} of proton-proton collision data used in this thesis. Run 3 is expected to more than double the Run 2 dataset size, significantly extending the available statistics for rare-process studies.

Both the accelerator and the detector systems undergo continuous improvements. Various detector subsystems were refurbished or upgraded during long shutdown periods to ensure optimal performance in subsequent data-taking periods [10]. The reconstruction software is also updated regularly and incorporates improvements in areas such as charged-particle tracking, primary-vertex reconstruction, isolation definitions, and the identification of jets originating from bottom quarks [11–13]. Monte Carlo (MC) simulation software evolves as well, providing improved modeling of parton showers, hadronization, and underlying-event activity [14–16]. Such improvements allow more precise measurements and motivate revisiting analyses originally performed under earlier hardware and software conditions.

Within the SM, the top quark, which was discovered in 1995 by the DØ [17] and CDF [18] collaborations at the Tevatron, is of particular interest. It is by far the heaviest known elementary particle, and its large mass implies a strong coupling to the Higgs field [19]. Top-quark processes are therefore sensitive probes for BSM physics that modify the Higgs interaction or introduce new heavy particles that preferentially couple to heavier SM particles [20].

The t-channel production of a single top quark in association with a photon ($tq\gamma$) is one of the rarest top-quark processes in the SM. For the generated MC samples, the MC generator predicts a leading-order cross-section of 1.40 pb for the leptonic top-quark decay channel. This cross-section is evaluated in a parton-level phase space, requiring an isolated photon with a minimum transverse momentum of $p_{\mathrm{T}}^{\gamma} > 10\,\mathrm{GeV}$. For comparison, Figure 1.1 shows the cross-sections of other top-quark processes measured by the ATLAS collaboration. The $t\bar{t}$ process exceeds the $tq\gamma$ process by about three orders of magnitude. The fiducial (i.e. defined within analysis-specific kinematic selections) cross-sections shown depend strongly on the respective analysis selections. In terms of inclusive cross-sections, even the already rare $t\bar{t}\gamma$ process has a cross-section approximately four times larger than that of the $tq\gamma$ process. Rare processes are particularly interesting, as their small SM rates make them sensitive to potential BSM contributions that can lead to statistically significant deviations from the SM expectation, provided the experimental and theoretical uncertainties are sufficiently well controlled.

Additionally, the $tq\gamma$ process directly probes the electroweak coupling between the top quark and the photon and is sensitive to modifications induced by BSM physics. The CMS collaboration reported the first evidence for this process in 2018 [21]. In 2023, the ATLAS collaboration published the first observation and an inclusive cross-section measurement [22]. The measured cross-section lies, like the CMS result, about two standard deviations above the theory central value. The $tq\gamma$ measurement is not statistically limited and therefore a good candidate for a differential cross-section measurement. This thesis presents the groundwork for that measurement under updated reconstruction and software conditions.

Essential parts of the previous $tq\gamma$ analysis are revisited in this thesis. This includes the special stitching procedure applied to the signal MC sample, the estimation of backgrounds with non-prompt photons using data-driven techniques, and the Neural-Network-based separation of signal and background. In addition, the author presents results from work done within the ATLAS collaboration on data-driven photon identification efficiency measurements.

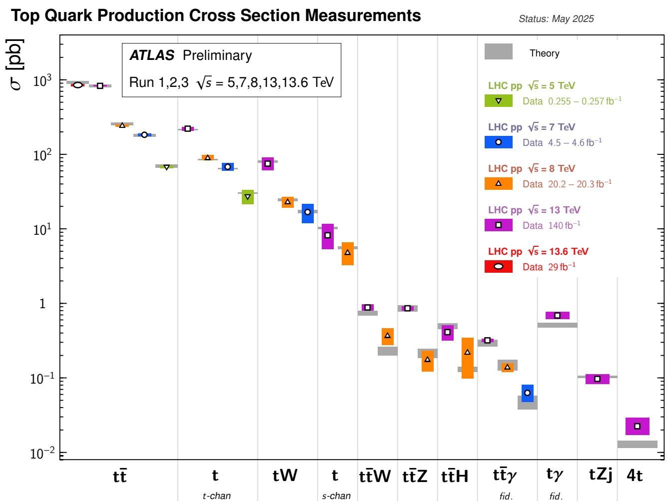

Figure 1.1: Overview of top-quark production cross-sections measured by the ATLAS collaboration for different data-taking periods. Colored markers indicate the measured cross-sections, while the gray bands show the corresponding Standard Model theoretical predictions. The values for top-quark pair production in association with a photon ($t\bar{t}\gamma$) and for single-top-quark production in association with a photon ($t\gamma$, denoted $tq\gamma$ in the rest of this thesis) are shown within the respective fiducial phase spaces of the individual analyses. Figure taken from Ref. [23].

The thesis is structured as follows: Chapter 2 gives a brief overview of the Standard Model, followed by a description of the LHC and the ATLAS detector in Chapter 3. The dataset and MC samples, including the stitching procedure for the signal sample, are described in Chapter 4. Chapter 5 details the reconstruction of physics objects and the changes introduced by recent software updates. Chapter 6 presents the data-driven photon identification efficiency measurements. The overall analysis strategy is outlined in Chapter 7, followed by the estimation of backgrounds with non-prompt photons in Chapter 8. Chapter 9 describes the Neural-Network-based signal separation, and Chapter 10 summarizes the presented results.

2 Top quarks and photons in the Standard Model of particle physics

The Standard Model of particle physics (SM) [1–3] is a relativistic quantum field theory. It describes fundamental particles, properties of these particles, and three out of the four known interactions between them, namely the strong, weak, and electromagnetic interactions. Gravity is not included in the SM. To date, the SM is the most successful theory for describing experimental observations in high-energy physics. An overview of the SM particles and interactions can be seen in Figure 2.1.

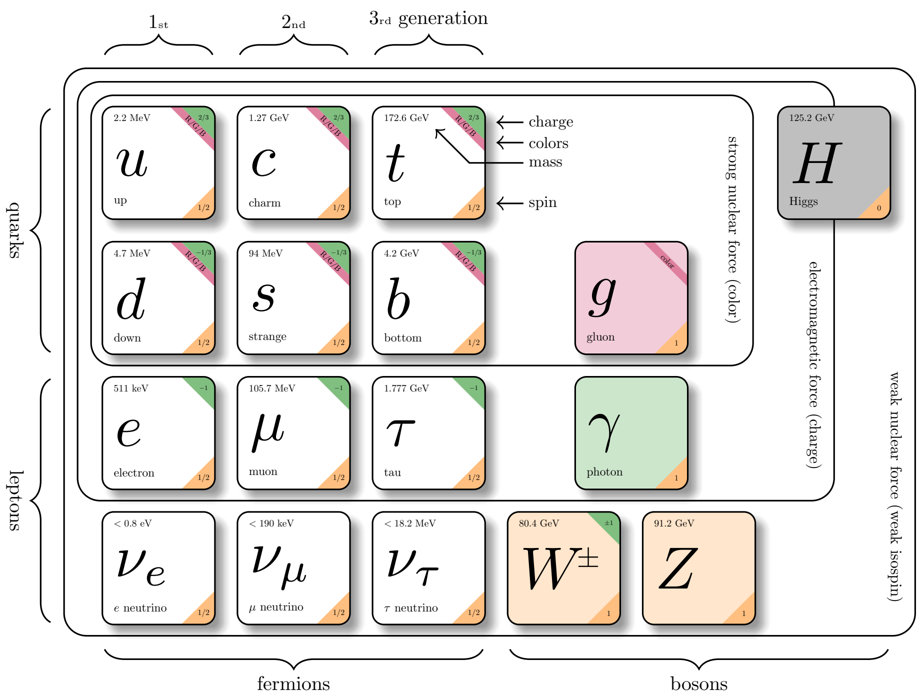

Figure 2.1: Illustration of the SM particles, some of their properties and their interactions. The graphic is adapted from Ref. [24] with property values taken from Ref. [7].

2.1 Fermions

Fermions, characterized by their half-integer spin, can be divided into two groups: quarks, which carry color charge, and leptons, which do not. Color charge is the quantum number that determines whether a particle participates in the strong interaction, as described in more detail in Section 2.2. Distinct particles can be understood as localized excitations of their respective quantum fields. Each fermion corresponds to a specific field that defines the particle's properties and possible interactions.

Quarks are organized into generations, each containing an up-type-down-type quark doublet. The up-type quark in a doublet always carries an electric charge of $+2/3e$ while down-type quarks carry an electric charge of $-1/3e$. The existence of three generations of quarks has been experimentally observed. The first generation consists of the up and down quarks (u and d). The second generation consists of the charm and strange quarks (c and s). The third generation consists of the top and bottom quarks (t and b). The generations are ordered by mass, with quarks in the first generation being the lightest and quarks in the third generation being the heaviest.

Similar to quarks, leptons are organized into generations that are ordered by mass. Each generation consists of a doublet comprising a lepton with an electric charge of $-1e$ and a corresponding neutrino with neutral electric charge. The existence of three generations of leptons has been experimentally observed. The first generation consists of the electron and the electron neutrino (e and ν_e). The second generation consists of the muon and the muon neutrino (μ and ν_μ). The third generation consists of the tau and tau neutrino (τ and ν_τ).

For each fermion, there exists a corresponding antiparticle with the same mass but with certain quantum numbers reversed, such as the electric charge and, in the case of quarks, the color charge.

2.2 Gauge bosons as mediators of interactions

Interactions in the SM are defined by the gauge symmetry group $\mathrm{SU}(3)_C \times \mathrm{SU}(2)_L \times \mathrm{U}(1)_Y$. Each symmetry term implies a corresponding conservation law, in which a specific quantity is preserved under the associated gauge transformations. For a field transforming under that symmetry, this conservation applies not only globally but also to local particles involved in the transformation. Therefore, in order to account for the transformation and maintain local invariance, gauge fields and their associated gauge bosons are introduced. The gauge bosons couple to particles affected by a transformation and thereby mediate the interactions. Interaction probabilities depend, among other factors, on the strength of the coupling of gauge bosons to interacting particles, known as coupling constants. Each interaction has a different coupling constant, which also depends on the energy scale at which the interaction occurs. After electroweak symmetry breaking, discussed in Section 2.3, the gauge symmetries give rise to the strong, weak, and electromagnetic interactions observed in nature. In the following, interactions are described in terms of the physical gauge bosons after electroweak symmetry breaking.

The strong interaction corresponds to the $\mathrm{SU}(3)_C$ symmetry group of quantum chromodynamics (QCD) and is mediated by gluons (g). Gluons are massless and, like all SM gauge bosons, they are spin-1 particles. They couple to the color charge C, which is the conserved quantity of the strong interaction. Since gluons carry color charge themselves, they couple not only to quarks but also to other gluons. Color charge has three possible states and corresponding anti-color states. In nature, only color-neutral states are observed, a phenomenon known as confinement. A color-neutral state can arise from combinations where either the three (anti-)colors or colors with corresponding anti-colors cancel each other out. Quarks, which themselves are not color-neutral, form color-neutral bound states called hadrons through a process known as hadronization. Hadrons have been most commonly observed in the form of baryons, which are composed of three (anti-)quarks, or mesons, which are composed of a quark and an anti-quark. The strong interaction is the only SM interaction whose coupling constant α_S decreases with increasing energy. This behavior is a consequence of a distinctive property of QCD known as asymptotic freedom. While quarks are confined at low energy scales, above energy scales of $\Lambda \approx 1\,\mathrm{GeV}$ they can be interpreted as approximately free. However, even at high energy scales, where $\alpha_\mathrm{S} \approx 0.1$, the strong interaction is the dominant interaction for most processes.

The weak interaction arises from the electroweak $\mathrm{SU}(2)_L \times \mathrm{U}(1)_Y$ symmetry group after spontaneous symmetry breaking. The L in $\mathrm{SU}(2)_L$ indicates that this symmetry acts only on fermions with left-handed chirality (and anti-fermions with right-handed chirality). The weak isospin T and the weak hypercharge Y are the quantum numbers associated with the $\mathrm{SU}(2)_L$ and $\mathrm{U}(1)_Y$ symmetry groups, respectively. The weak interaction is mediated by the $W^\pm$ and Z bosons. Unlike the other SM gauge bosons, the $W^\pm$ and Z bosons have non-zero mass. The weak interaction is the only SM interaction that allows transitions between different types (flavors) of quarks. While suppressed, quarks can transition between generations. For leptons, flavor-changing weak interactions occur only within a generation, i.e. between a charged lepton and its corresponding neutrino. Neutrinos interact only via the weak interaction in the SM and can change flavor through neutrino oscillations [25, 26]. Because of the mass of the weak gauge bosons, the weak interaction is short-range and strongly suppressed at low energies. At energies around the weak gauge boson masses, however, the weak interaction is the second strongest interaction, with an effective coupling strength of $\alpha_{\mathrm{w}} \approx 1/30$.

The electromagnetic (EM) interaction arises after electroweak symmetry breaking and is mediated by the massless photon (γ), corresponding to the unbroken $\mathrm{U}(1)_{\mathrm{EM}}$ symmetry group. This group emerges from the electroweak $\mathrm{SU}(2)_L \times \mathrm{U}(1)_Y$ group after symmetry breaking. The conserved quantity to which the photon couples is the electric charge $Q = T_3 + \frac{Y}{2}$, where T_3 denotes the third component of the weak isospin. Unlike the gauge bosons of the strong and the weak interactions, the photon does not self-couple. The coupling strength of the electromagnetic interaction, α_{EM}, increases slightly with increasing energy, but at energies accessible in present-day high-energy collider experiments, it remains relatively constant at around $\alpha_{\mathrm{EM}} \approx 1/128$.

2.3 The Higgs mechanism

For the $\mathrm{SU}(2)_L \times \mathrm{U}(1)_Y$ symmetry group, gauge invariance forbids explicit mass terms for gauge bosons as well as fermions, which does not match experimental observations. To resolve this, the scalar Higgs field is introduced, which has a non-zero vacuum expectation value. Through its interaction with the electroweak gauge fields, this leads to spontaneous breaking of the $\mathrm{SU}(2)_L \times \mathrm{U}(1)_Y$ symmetry group. As a result, linear combinations of the electroweak gauge fields give rise to the physical gauge bosons observed in nature, namely the weak $W^{\pm}$ and Z bosons as well as the electromagnetic photon. The $W^{\pm}$ and Z bosons acquire mass through their interaction with the Higgs field. The remaining unbroken $\mathrm{U}(1)_{\mathrm{EM}}$ symmetry leaves the photon massless and ensures the conservation of electric charge in electromagnetic interactions. Fermions gain mass via Yukawa couplings to the Higgs field. The strength of these couplings varies between different fermions, leading to the observed mass spectrum. The resonant particle of the Higgs field, the spin-0 Higgs boson, was discovered in 2012 by both the ATLAS [5] and the CMS experiment [6].

2.4 Single top-quark production in association with a photon

The top quark, being the heaviest SM particle, is of particular interest due to its large Yukawa coupling to the Higgs field. Production of a single top quark in association with a photon is an SM process with a small predicted cross-section at the energy scale of present-day high-energy particle colliders. Studying this process provides a unique test of the top-photon coupling via the electromagnetic interaction. Moreover, it allows precise tests of the top quark's properties, such as its electric and magnetic dipole moments [27, 28]. Any discrepancies with SM predictions could hint at new physics beyond the SM.

Single top quarks can be produced through the t-, tW-, or s-channel. In the s-channel, a W boson mediates the interaction and decays into a top quark and a bottom quark. Top quarks decay almost exclusively via the weak interaction into a bottom quark and a W boson. For the single-top s-channel, this typically results in a final state with two bottom quarks. Because of that, the final state can resemble top quark pair production ($t\bar{t}$). The predicted s-channel cross-section for proton-proton (pp) collisions at a center-of-mass collision energy $\sqrt{s} = 13\,\text{TeV}$ is $\sigma = 10.3^{+0.4}_{-0.4}\,\text{pb}$ [29]. In the tW-channel, a bottom quark and a gluon interact to produce a top quark together with a W boson. After the top quark decays, the final state includes two W bosons, again resembling $t\bar{t}$ production. The predicted tW-channel cross-section for pp collisions at $\sqrt{s} = 13$ TeV is $\sigma = 79.5^{+2.9}_{-2.8}\,\text{pb}$ [30]. In the t-channel, a bottom quark interacts with another quark via a W boson to produce a top quark. This channel typically produces one bottom quark from the top-quark decay, at most one charged lepton, and a light spectator quark. The t-channel is the single-top production mode with the largest predicted cross-section for pp collisions at $\sqrt{s} = 13$ TeV of $\sigma = 214.2^{+4.1}_{-2.6}\,\text{pb}$ [31]. Its distinct topology allows better separation from $t\bar{t}$ events.

Because of the higher cross-section and the event topology that can more easily be separated from the $t\bar{t}$ process, this analysis focuses on t-channel production. The associated photon can be radiated from any charged particle involved in the interaction, such as the top quark, the W bosons, or any initial- or final-state quark. The W boson from the top-quark decay can decay either leptonically into a charged lepton and a neutrino or hadronically into a pair of quarks. To suppress the large background from purely hadronic processes, this analysis selects events where the W boson decays leptonically. The corresponding leading-order Feynman diagram of the process (the $tq\gamma$ process) is shown in Figure 2.2.

2.4.1 Background processes

In addition to the signal process, several other SM processes can produce final states containing charged leptons, neutrinos, and bottom quarks, thereby resulting in event topologies similar to that of the $tq\gamma$ process. Such background processes may contain photons that originate directly from the hard interaction, referred to as prompt photons, or events may contain photons from hadron decays or other secondary processes (non-prompt photons), or particles, most commonly electrons or hadrons, that are misidentified as photons (fake photons). Even processes that do not produce the same set of final state particles exactly can contribute to the background if some particles in an event are not correctly identified.

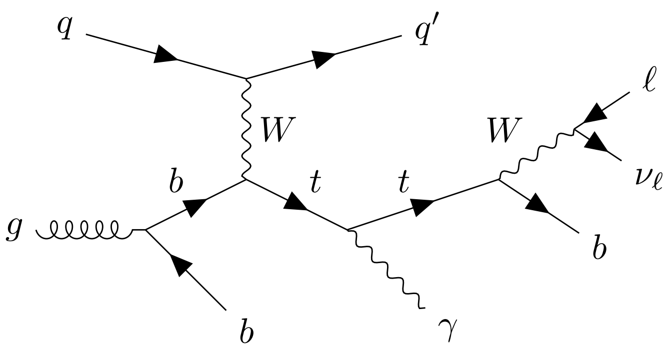

Figure 2.2: Leading-order Feynman diagram for t-channel single top-quark production in association with a photon. A bottom quark (b) from the initial state interacts with a spectator quark (q) via the exchange of a virtual W boson, producing a top quark (t). The top quark subsequently decays into a bottom quark, a charged lepton (ℓ), and a neutrino (ν_ℓ). The photon (γ) can be radiated from any charged particle in the process, including the top quark, the W boson, or the initial- or final-state quarks.

A dominant background originates from top-quark pair production. In particular, semileptonic $t\bar{t}$ events, where one W boson decays leptonically and the other hadronically, produce a final state containing one charged lepton, one neutrino, and two bottom quarks, together with additional quarks from the hadronic W boson decay. Although no prompt photon is produced in the hard interaction, non-prompt and fake photons may appear in $t\bar{t}$ events. Given the large $t\bar{t}$ production cross-section, which even for the semileptonic decay channel alone exceeds that of the $tq\gamma$ process by more than two orders of magnitude, such events constitute a significant background.

Another major background is top-quark pair production in association with a photon ($t\bar{t}\gamma$). This process has a cross-section of the same order of magnitude as the $tq\gamma$ process and contains a genuine prompt photon in the final state. Since the remainder of the event topology is equivalent to that of $t\bar{t}$ production, $t\bar{t}\gamma$ events can closely mimic the $tq\gamma$ signal.

Further background contributions arise from electroweak processes with a prompt photon, most notably $W\gamma$ and $Z\gamma$ production in association with quarks. In $W\gamma$ events, the W boson can decay leptonically, producing a charged lepton and a neutrino, similar to the signal final state. $Z\gamma$ events contribute when the Z boson decays into neutrinos, producing missing energy, or into charged leptons if one lepton is not correctly identified, resulting in a partially similar topology.

Finally, processes without a prompt photon can contribute to the background through non-prompt or fake photons. These processes include W and Z production in association with quarks. While the event topology is generally less similar to the $tq\gamma$ signal, the contribution arises when particles are not correctly identified. Having a final state signature similar to the signal process, production of single top quarks also contributes as a background.

2.4.2 Previous measurement by the ATLAS collaboration

The $tq\gamma$ process has previously been measured using the full Run 2 dataset recorded by the ATLAS experiment at $\sqrt{s} = 13$ TeV [22]. In that analysis, a fiducial cross-section measurement was performed in the leptonic decay channel of the top quark. A schematic overview of the analysis strategy is shown in Figure 2.3. Events were categorized into two signal regions according to the presence of a characteristic spectator quark produced in the t-channel exchange. The first signal region contained events without such a signature (no-spectator SR), while the second required at least one such signature (spectator SR). In addition, two control regions enriched in the dominant prompt-photon backgrounds, $t\bar{t}\gamma$ and $W\gamma$ production, were defined.

Two Neural Network (NN) classifiers were trained independently in the two signal regions. The NNs combined several kinematic and topological observables into a single discriminating NN output variable. Two inclusive $tq\gamma$ cross-sections were extracted using separate simultaneous binned likelihood fits with two slightly different signal definitions. As input to both fits, the NN output distributions in the two signal regions and in the $t\bar{t}\gamma$ control region were used, where high NN output values correspond to an increased $tq\gamma$ signal fraction. In addition, the inclusive event yield in the $W\gamma$ control region was used as input to the fits.

For such fits, a likelihood is constructed as a product of Poisson probabilities $\mathcal{P}_{r,b}$ over all bins b of all regions r. Each $\mathcal{P}_{r,b}$ defines the probability to obtain the observed event count in data, given the expected yields from signal and background processes. The expected yields are derived from simulation and parametrized in terms of several parameters that affect both the normalization and the shape of the predicted distributions. The fit determines the parameter values that maximize the likelihood and therefore best describe the observed data yields. For the inclusive $tq\gamma$ measurement, these parameters included an overall normalization factor for the $tq\gamma$ contribution $\mu_{tq\gamma}$, a normalization factor for the $t\bar{t}\gamma$ process, and a normalization factor for the $W\gamma$ process. Systematic and statistical uncertainties were incorporated as additional parameters in the likelihood model. These parameters, in contrast to the normalization parameters, are constrained by probability distributions, such that deviations from their nominal values reduce the likelihood value according to the associated uncertainties.

Comparing the obtained likelihoods with those from fits performed under the no-signal hypothesis, the no-signal hypothesis was rejected with a significance of 9.3σ, representing the first observation of the $tq\gamma$ process. From the $\mu_{tq\gamma}$ values determined by the fits, inclusive cross-sections were measured. The results were found to be about two standard deviations above the central value of the SM predictions. The measurement precision was primarily limited by systematic uncertainties, with the largest contribution arising from the uncertainty related to the modeling of the $t\bar{t}\gamma$ background. These observations motivate further studies of the $tq\gamma$ process, in particular differential measurements that probe the kinematic and topological properties of the process and may provide increased sensitivity to deviations from SM predictions.

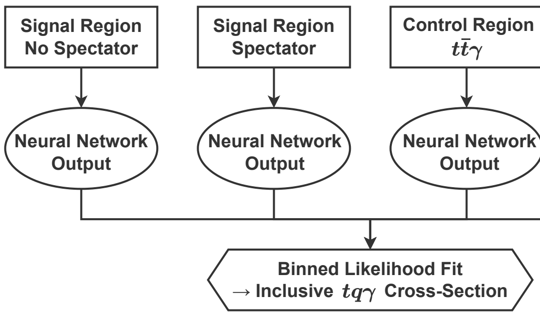

Figure 2.3: Schematic overview of the analysis strategy used in the previous inclusive $tq\gamma$ measurement [22]. Events are categorized into signal and control regions. Depending on the region, either the Neural Network output distribution or the inclusive event yield is used as input to a simultaneous binned likelihood fit, from which the inclusive $tq\gamma$ cross-section is extracted.

3 Experimental setup

3.1 Proton collisions at the CERN accelerator complex during Run 2

In order to test the predictions of the SM, to perform precision measurements of its parameters, and to search for physics beyond the Standard Model, one approach is to produce a variety of particles in a controlled experimental environment where their properties can be precisely measured. The Large Hadron Collider (LHC) [32], situated at CERN in Geneva, Switzerland, serves this purpose. Here, high-energy protons, or other particles if required, are brought into collision. A portion of the collision energy is converted into rest mass energy, facilitating the production of possibly even the heaviest SM particles. With a circumference of 26.7 km and a center-of-mass collision energy for protons in Run 2 of 13 TeV, the LHC is the largest and highest-energy particle collider worldwide.

Achieving collisions of protons at energies that high requires the sequential acceleration of the protons through a series of pre-accelerators at the CERN accelerator complex. A schematic depiction of its layout is shown in Figure 3.1. For Run 2, hydrogen atoms that are stripped of their electrons are used as a source of protons. These protons are injected into the Linear Accelerator 2 (LINAC2), where they are brought to an energy of 50 MeV. Subsequently, the protons are successively accelerated to up to 1.4 GeV in the Proton Synchrotron Booster (BOOSTER), up to 25 GeV in the Proton Synchrotron (PS), and up to 450 GeV in the Super Proton Synchrotron (SPS). As the final stage of the accelerator complex, the LHC, a ring accelerator and collider, further increases the proton energy to the nominal collision energy. The protons circulate in opposite directions in the two separate beam pipes before being collided at one of the four particle interaction points. The protons are grouped into discrete *bunches*. During Run 2, these bunches are crossed at the interaction points with a bunch crossing rate of up to 40 MHz.

Four different detectors are positioned around the interaction points. The ALICE detector [33] specializes in heavy ion collisions and focuses on the study of quark-gluon plasma. The LHCb detector [34] is specifically designed to study

b-hadrons, which are especially important for understanding matter-antimatter asymmetry. Both the CMS detector [35] and the ATLAS detector [36–39] are versatile general-purpose detectors that study a wide range of particle physics phenomena.

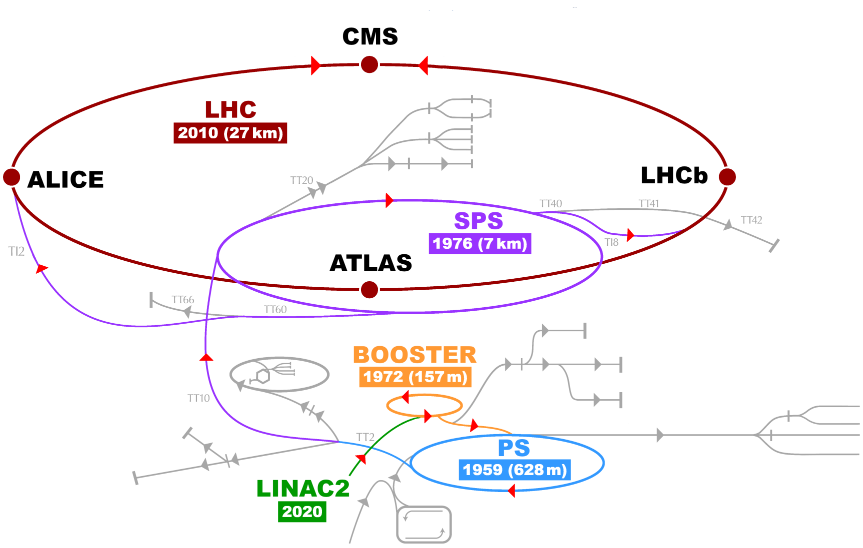

Figure 3.1: The CERN accelerator complex. Protons are accelerated through the injector chain, consisting of the Linear Accelerator 2 (LINAC2, shown in green), the Proton Synchrotron Booster (PSB, shown in orange), the Proton Synchrotron (PS, shown in blue), and the Super Proton Synchrotron (SPS, shown in purple), before being injected into the final stage, the Large Hadron Collider (LHC, shown in red). The LHC hosts four major experiments, the ALICE, the ATLAS, the CMS, and the LHCb experiments. Graphic adapted from Ref. [40].

The instantaneous luminosity $\mathcal{L}_{\text{inst}}$ at a collider quantifies the number of interactions N per time t for a given process with cross-section σ via

$$\mathcal{L}_{\text{inst}} = \frac{1}{\sigma}\frac{\mathrm{d}N}{\mathrm{d}t}. \tag{3.1}$$

At the LHC, $\mathcal{L}_{\text{inst}}$ depends on the number of particle bunches per beam, the number of particles per bunch, the revolution frequency of the circulating beams, as well as the geometry of the bunches at the interaction point. During Run 2, the LHC operated with up to 2544 proton bunches per beam, each typically containing about 10^{11} protons, circulating at a revolution frequency of about 11.2 kHz. This configuration allowed the LHC to reach peak instantaneous luminosities of up to $21.0 \cdot 10^{33}\,\mathrm{cm}^{-2}\mathrm{s}^{-1}$ [41, 42].

3.2 The ATLAS Detector

3.2.1 General layout

A schematic cut-away view of the detector can be seen in Figure 3.2. The detector has a cylindrical layout, symmetric around the beam axis. It is designed to provide nearly complete coverage of the 4π solid angle around the interaction point. Gaps are only present for essential components such as the beam pipe itself, support structures, and infrastructure such as electronics and cabling. This design minimizes the risk of particles escaping detection through gaps.

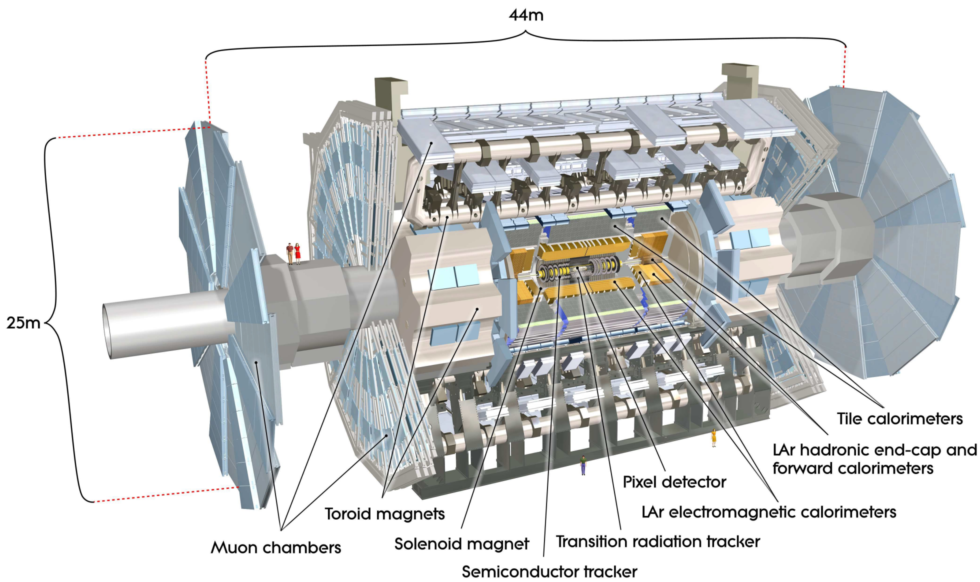

Figure 3.2: Schematic cut-away view of the ATLAS detector. Figures of people are shown for scale [36].

Descriptions of the detector geometry are based on a right-handed coordinate system with the origin at the nominal interaction point. In this system, the z-axis aligns with the beam axis. The positive x-axis extends inward from the interaction point, and the positive y-axis points upward. Cylindrical coordinates are commonly used, where the azimuthal angle ϕ is defined in the x-y plane around the z-axis, and the radial distance R denotes the distance from the z-axis. The polar angle θ is defined relative to the z-axis, from which the pseudorapidity $\eta = -\ln\tan(\theta/2)$ is derived. The detector covers pseudorapidities up to $|\eta| = 4.9$. Observables such as the transverse energy E_T and the transverse momentum p_T are defined in the transverse

x-y plane. Distances in the η-ϕ space are given by $\Delta R = \sqrt{\Delta\eta^2 + \Delta\phi^2}$. Using η instead of θ entails the advantage that differences $\Delta\eta$ and angular separations ΔR are approximately invariant under Lorentz boosts along the beam axis for highly relativistic particles.

The detector is divided into two main sections, commonly referred to as the barrel region and the end-cap regions. The barrel region comprises the cylindrical section that extends around the beam axis, while the end-caps are the disk-shaped sections at each end of the cylinder. Both sections consist of several detector components, which allow the detection of all SM particles, with the exception of neutrinos. These components are described in the following sections.

3.2.2 Inner Detector

The Inner Detector (ID) is the detector component closest to the interaction point, designed to reconstruct tracks of charged particles. A schematic cut-away view is shown in Figure 3.3. The ID covers a pseudorapidity range of $|\eta| < 2.5$ and consists of three main sub-detectors, arranged in layers, as shown in Figure 3.4.

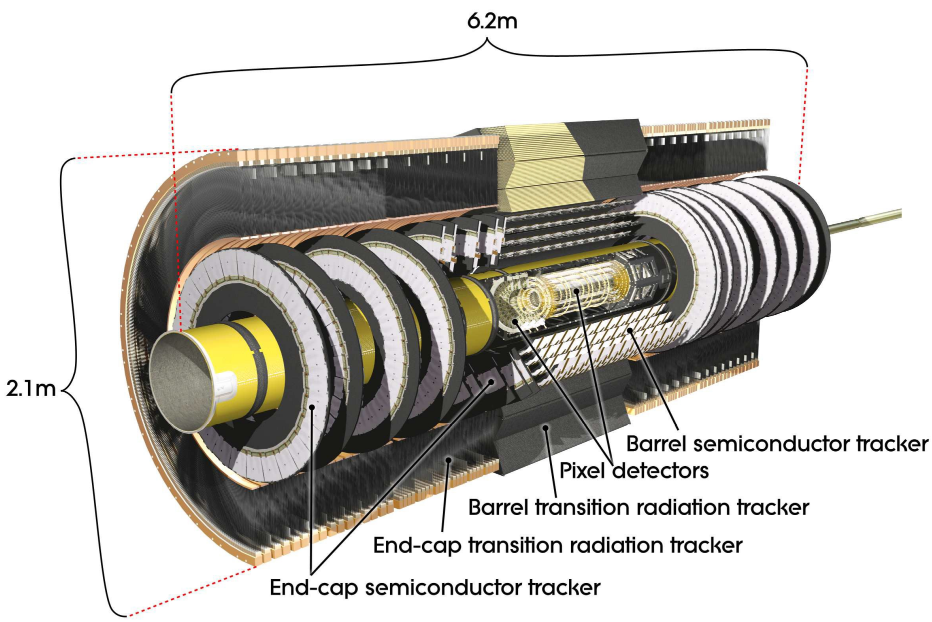

Figure 3.3: Schematic cut-away view of the ATLAS Inner Detector [36].

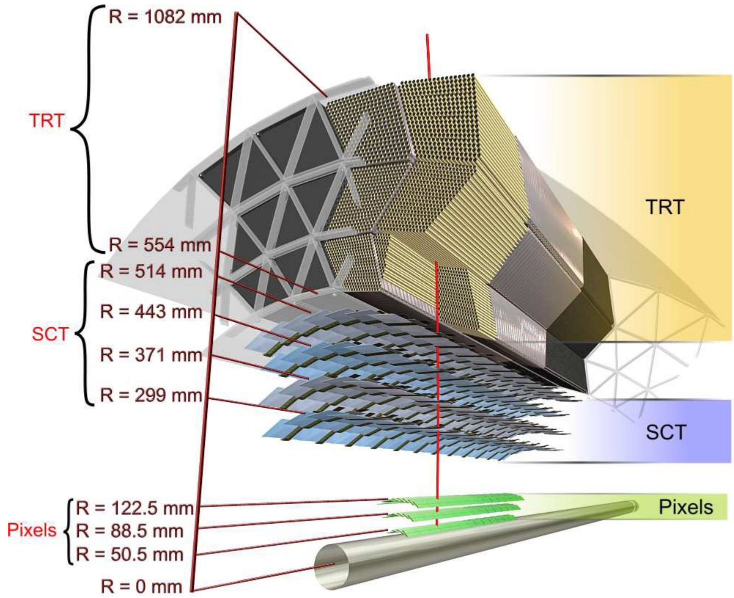

Figure 3.4: Illustration showing the arrangement and dimensions of the various Inner Detector layers in the barrel region [36].

The innermost sub-detector is the Pixel Detector, a silicon semiconductor tracker. It contains three pixel layers in both the barrel region and the end-cap regions. The barrel region also features an additional layer closest to the beam, the Insertable B-Layer (IBL) [37–39]. The Pixel Detector has a spatial resolution of 10 µm in azimuthal direction and 115 µm in z direction (barrel region) and R direction (end-cap regions).

Surrounding the Pixel Detector is the SemiConductor Tracker (SCT). This sub-detector consists of four layers of silicon micro-strip sensors in the barrel region and nine layers in each end-cap region. The SCT provides a resolution of 17 µm in the azimuthal direction and 580 µm in z direction (barrel region) and R direction (end-cap regions).

The outermost sub-detector is the Transition Radiation Tracker (TRT), which extends to $|\eta| < 2$. The TRT consists of straw tubes filled with a gas mixture that become ionized as charged particles pass through. When a charged particle crosses the boundary between materials with different dielectric constants, it emits transition radiation in the form of photons. The comparatively light electrons tend to emit more photons than heavier hadrons. By detecting ionization and transition radiation, the TRT provides tracking information and helps distinguish electrons from hadrons.

As charged particles traverse the ID, they leave distinct hits in each of the sub-detectors. A track can have up to four hits in the pixel detector, up to four hits in the SCT, and as many as 36 hits in the TRT. These hits are reconstructed into tracks, which are a crucial part of the overall object reconstruction and also allow for the determination of primary and secondary vertices with high precision.

Additionally, the ID is surrounded by a solenoid magnet that produces a 2 T axial magnetic field, which bends the trajectories of charged particles, enabling the measurement of their charge and momentum.

3.2.3 Calorimeters

Surrounding the Inner Detector is the calorimeter system, which is divided into two main components: the electromagnetic calorimeter (ECAL) and the hadronic calorimeter (HCAL). These sub-detectors allow the measurement of the energy and position of electrons, photons, hadrons, as well as particles that might decay into one of the above before reaching the calorimeter system, as is e.g. most often the case for tau leptons. A schematic cut-away view of the calorimeters can be seen in Figure 3.5.

To minimize punch-through, where high-energy particles might pass through the calorimeter without being stopped, the calorimeter uses a sampling design. This involves alternating layers of different absorber materials and active material. The absorber material forces incoming particles to interact and produce showers of secondary particles. The active material then detects these showers either through scintillation or by measuring the ionization produced by the shower particles. The position and shape of the measured energy depositions, combined with the tracking information from the Inner Detector, enables precise identification and reconstruction of the corresponding particles, as discussed in more detail in Chapter 5.

The ECAL in the barrel region uses liquid argon as active material with lead as absorber. It has an accordion geometry, which avoids cracks in the azimuthal direction. The ECAL is divided into three layers with different granularity. The first layer has very fine segmentation in η direction. It is crucial for photon identification, since it helps distinguish prompt photons, which originate directly from the hard interaction, from overlapping photons produced by hadron decays or radiation. The second layer, which contains the largest amount of absorber material, collects most of the shower energy. The third layer is the coarsest layer and helps to absorb high-energy showers that would otherwise extend beyond the ECAL depth. In the barrel region, the typical cell granularity is of the order $\Delta\eta \times \Delta\phi \approx 0.025 \times 0.025$ in the second layer and significantly finer in the first layer. A presampler in front of the barrel ECAL, covering $|\eta| < 1.8$, corrects for energy lost in the detector components preceding the calorimeter. The electromagnetic end-caps (EMEC) extend the ECAL coverage up to $|\eta| \approx 3.2$. The EMEC uses the same three-layer structure as the barrel ECAL, with adapted granularity to match the changing particle densities and radiation conditions at large $|\eta|$.

The HCAL lies directly behind the electromagnetic calorimeter. In the barrel region, including the extended barrel which covers up to $|\eta| < 1.7$, steel is used as absorber material and scintillating tiles as active material. The light produced in the tiles is collected by photomultipliers on both sides. The granularity is coarser than in the ECAL because hadronic showers are usually wider and their internal structure fluctuates more, which limits the benefit of fine segmentation. In the end-cap regions, the hadronic end-cap calorimeters (HECs) use copper absorber plates and liquid argon as active material. The HECs provide hadronic energy measurements up to $|\eta| < 3.2$.

At very small angles with respect to the beam axis, the forward calorimeters (FCALs) extend the calorimetry into the high-η region. The FCALs use liquid argon with dense absorber materials, such as copper or tungsten, and combine electromagnetic and hadronic calorimeter functionality. Together with the barrel and end-cap calorimeters, nearly full calorimeter coverage up to $|\eta| < 4.9$ is provided.

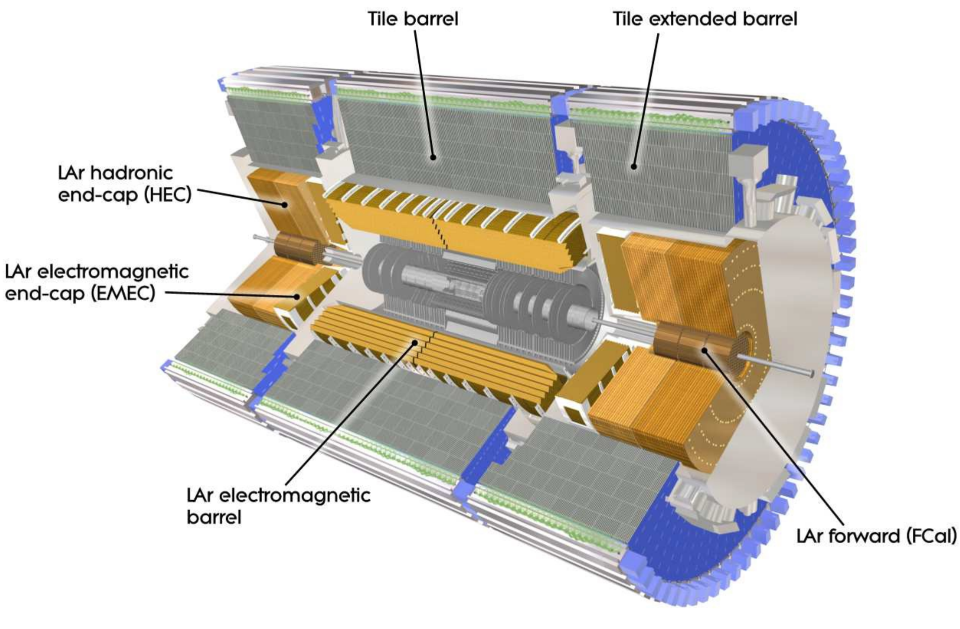

Figure 3.5: Schematic cut-away view of the ATLAS calorimeter system [36].

3.2.4 Muon spectrometer system

The outermost part of the ATLAS detector is the muon spectrometer, which is cylindrical around the beam axis. The system consists of superconducting air-core toroid magnets along with three layers of tracking chambers, covering both the barrel region and the end-cap regions. The primary purpose of the muon spectrometer is to determine the trajectories, the charge, and the momentum of charged particles that exit the calorimeter system. The spectrometer provides coverage up to $|\eta| < 2.7$. A schematic cut-away view of the muon system is shown in Figure 3.6.

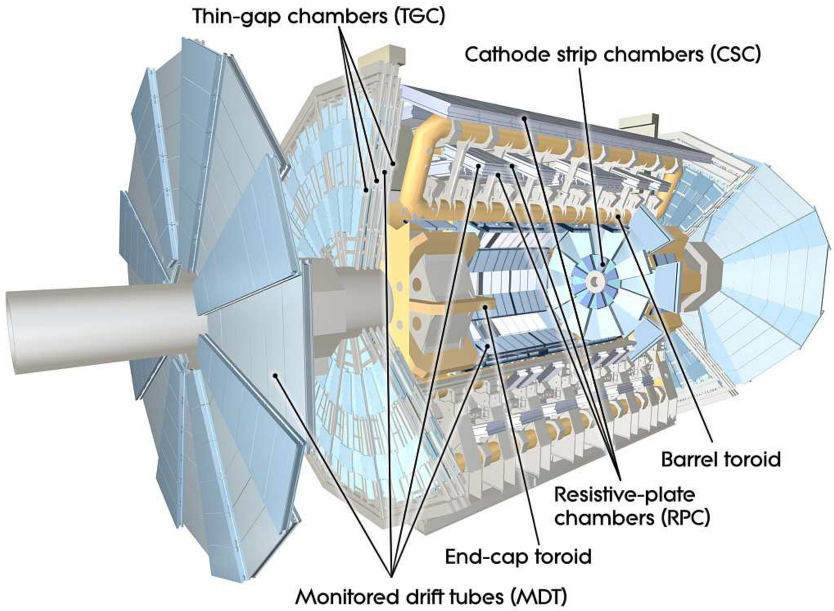

Figure 3.6: Schematic cut-away view of the ATLAS muon spectrometer system [36].

All active detector elements within the muon spectrometer rely on the ionizing effect of passing particles. The tracking information is primarily provided by Monitored Drift Tubes. However, in the range of $2.0 < |\eta| < 2.7$, the innermost layer of the end-caps is equipped with Cathode Strip Chambers, which are designed to withstand higher radiation and offer improved time resolution for the high particle rates in this region. Both types of tracking chambers specialize in measuring the position of muons in the bending plane (the η coordinate).

For $|\eta| < 2.4$, the spectrometer also includes trigger chambers: Resistive Plate Chambers in the barrel region and Thin Gap Chambers in the end-caps. These trigger chambers provide rapid track information with a latency of less than a nanosecond, enabling the identification of potentially interesting events, as detailed in Section 3.2.5. Additionally, the trigger chambers complement the tracking chambers by measuring the position of particles in the non-bending plane (the ϕ coordinate).

The combination of the Inner Detector, the calorimeters, and the muon spectrometer allows for the detection of all SM particles except neutrinos. As a result, the ATLAS detector is capable of measuring the missing transverse momentum $E_{\mathrm{T}}^{\mathrm{miss}}$, defined as the negative vector sum of reconstructed transverse momenta in an event, which can then be attributed to non-interacting particles such as neutrinos.

3.2.5 Trigger system

The ATLAS trigger system [43] is essential for efficiently processing and recording only those events that exhibit characteristics deemed relevant for further analysis. This involves selecting events with specific features, such as high-energy particles or significant missing transverse momentum. Given the LHC's bunch crossing rate of up to 40 MHz, it is crucial to filter out less significant events. Otherwise, the immense volume of data would overwhelm both computational and storage capabilities.

The trigger system operates in two stages: the Level-1 (L1) trigger and the High-Level Trigger (HLT). The L1 trigger is a hardware-based system that processes granular information from the calorimeters and the muon spectrometer, selecting up to 100 kHz of events per second, which are then passed to the HLT.

The HLT is a software-based system that processes more detailed information from all detector systems described above. It performs a refined selection of events, with an average output rate of 1.2 kHz being stored for detailed offline analysis.

4 Analyzed dataset and Monte Carlo samples

4.1 Data

For the differential measurement of the $tq\gamma$ process, the full Run 2 dataset recorded with the ATLAS detector during the LHC data-taking periods between 2015 and 2018, with a center-of-mass collision energy of 13 TeV, is used. A measure for the amount of recorded particle collisions is the integrated luminosity

$$\mathcal{L}_{\text{int}} = \int \frac{1}{\sigma} \frac{\mathrm{d}N}{\mathrm{d}t} \,\mathrm{d}t = \frac{N}{\sigma}, \tag{4.1}$$

where N is the number of events for a given cross-section σ. The Run 2 dataset corresponds to an integrated luminosity of $(140.1 \pm 1.2)\,\mathrm{fb}^{-1}$ [41].

4.2 Monte Carlo simulations for signal and background processes in high-energy physics

In high-energy physics measurements, the term *signal* refers to the process of interest, while all other processes are labeled as *background*. To obtain a dataset with high signal purity and efficiency, selection criteria are applied. These selections accept events that match the signal's signature in the detector, requiring the reconstruction of specific particles with specific properties. This reliably rejects many background processes. However, some background events may still pass the selection. This occurs when background processes have detector signatures similar to the signal or when particles are misidentified, resulting in background events mimicking the signal.

Monte Carlo (MC) simulations play a key role in optimizing selection criteria, estimating background contributions, and comparing observed data with theoretical predictions. MC simulation is a computational technique used to accurately model complex systems and processes through random sampling. At the ATLAS experiment, MC simulations model various aspects of particle interactions. This starts with the hard scattering of the two colliding protons. In the following, the modeling of the hard-scattering process is described first, before addressing subsequent stages such as parton showering and hadronization.

Predictions for particle interactions cannot be directly calculated analytically. To describe the electromagnetic and weak interactions between particles, perturbation theory can provide an accurate approximation. The coupling constant in these interactions is expanded in a series where each successive term becomes smaller and eventually negligible. For the strong interaction, perturbation theory is applicable only at high energy scales, where the strong coupling constant becomes small and quarks can be treated as asymptotically free. At low energy scales, known as the non-perturbative regime, alternative approaches are required.

Colliding protons, and hadrons in general, consist of valence quarks, sea quarks, and gluons, collectively referred to as partons. Valence quarks are the quarks that define a hadron. In the case of protons, these are two up quarks and one down quark. An indefinite number of sea quarks and gluons arises from quantum fluctuations in the proton's vacuum state. The distribution of partons within a proton is described by parton distribution functions (PDFs), $f_a(x_a, \mu)$, which represent the probability density of finding a parton of type a with momentum fraction x_a at a given energy scale μ. PDFs have to be determined experimentally for different values of μ.

During high-energy collisions, partons from both protons interact, with their momenta distributed according to the underlying PDFs. The factorization theorem [44] allows the separation of the cross-section into a perturbative and a non-perturbative part. For a process with two initial and n final state particles, this can be written as

$$\sigma = \sum_{a,b} \int_0^1 \mathrm{d}x_a \, \mathrm{d}x_b \, f_a(x_a, \mu_F) \, f_b(x_b, \mu_F) \, \frac{1}{2x_a x_b s} \int \mathrm{d}\Phi_n \, |\mathcal{M}|^2. \tag{4.2}$$

The sum runs over all possible parton types a and b that can participate in the hard-scattering process. The PDFs f_a and f_b, evaluated at a factorization energy scale μ_F, are integrated over the momentum fractions x_a and x_b, representing the non-perturbative component of the cross-section. The factor $\frac{1}{2x_a x_b s}$ accounts for the flux of the incoming partons, normalizing the cross-section by the momentum fractions of the interacting partons and the squared center-of-mass energy s. The integral over the differential phase space element of the final state particles $\mathrm{d}\Phi_n$ corresponds to the perturbative part of the cross-section. It accounts for all possible kinematic configurations of the final state particles, including their momenta and angular distributions. Finally, $|\mathcal{M}|^2$ is the squared matrix element, derived from all Feynman diagrams of the process, up to a given order of accuracy in α_S (typically leading order (LO) or next-to-leading order (NLO)), encoding the probability amplitude for the partons to scatter into the specified final state.

While the factorization theorem allows for a description of the hard-scattering process, the resulting partons undergo further processes that must also be modeled. The color-charged partons radiate additional gluons or quark-anti-quark pairs in a process known as the parton shower. This emission can occur either as initial-state radiation, or as final-state radiation. Unlike the hard-scattering process, which typically involves a small number of high-energy particles, the parton shower generates a large number of lower-energy particles as the partons cascade. With successive emissions, the energy of the emitted particles decreases, eventually reaching a non-perturbative regime where quarks are no longer asymptotically free and are confined into hadrons. This transition is referred to as hadronization. To model the parton shower and hadronization, parton shower algorithms are employed, most commonly using the Lund string model [45, 46] or the cluster model [47, 48]. These algorithms simulate the sequential radiation of partons using probabilistic methods, accounting for both perturbative and non-perturbative effects. This ensures a realistic description of the transition from partons to the observed hadrons.

In addition to the primary hard scatter, other partons from the colliding protons can interact, contributing to what is known as the *underlying event*. These interactions are typically lower in energy compared to the hard scatter. The underlying event, as well as contributions from interactions in the same or neighbouring bunch crossings (pile-up) are often modeled for Run 2 with the MC generator PYTHIA version 8.186 [49], configured according to the A3 tune [50] and using the NNPDF2.3LO [51] parton distribution function (PDF) set. Simulated events are weighted to reproduce the distribution of the average number of interactions per bunch crossing observed in data.

For the MC event generation, the frameworks MADGRAPH [52] or POWHEG BOX [53–56] are often used for calculating hard-scatter events with leading-order or higher precision. These events are interfaced to PYTHIA [49] or HERWIG [57] for the modeling of the parton shower and hadronization. The EVTGEN [58] program is frequently employed for simulating subsequent decays of hadrons containing bottom or charm quarks. SHERPA [59] serves as an alternative multi-purpose event generator that encompasses all aspects of event simulation, from matrix elements to final-state particle interactions. The ATLAS detector response is simulated using the GEANT4 [60] framework, which models in detail the interaction of particles with the detector material. Alternatively, for faster simulations, FASTSIM [61] is used, providing a parameterized approximation of the ATLAS calorimeter response. A detailed description of the different MC samples used in this thesis is provided in the following sections.

4.3 Signal modeling

The $tq\gamma$ process at LO is illustrated by the Feynman diagram shown in Figure 2.2. In practice, the photon can be radiated not only during the production of the top quark, but also from any charged decay product of the top quark, such as the bottom quark, the W boson, or the charged lepton.

While MadGraph5_aMC@NLO models photon radiation during the production stage at NLO precision, the subsequent decay of the top quark is not simulated at the matrix-element level. Instead, the decay is handled by MadSpin [62], which does not include photon radiation from top-quark decay products.

To address this limitation, a *stitching* procedure is applied. Events are selected from a single-top-quark t-channel NLO sample (effectively the signal process without an explicit photon), where a photon is radiated during the decay via the parton shower. These events are then combined with the dedicated $tq\gamma$ NLO sample that models radiation during production. In this way, a signal sample is obtained that includes photon radiation from both the production and decay stages of the top quark, modeled at NLO precision. A $tq\gamma$ LO sample, which includes photon radiation in both production and decay, is used for validation and cross checks of the stitched sample.

Details on the individual signal samples are given in Section 4.3.1 (for the LO and NLO $tq\gamma$ samples) and Section 4.3.2 (for the single-top-quark t-channel NLO sample). The stitching procedure and the resulting combined sample are described in Section 4.3.3.

4.3.1 Single-top-quark-plus-photon LO and NLO samples

Single-top-quark t-channel events in association with a photon were simulated at both LO and NLO in QCD, following the strategy described above. Both samples were produced using MadGraph5 3.3.1 [52], with the NNPDF3.0nlo [63] PDF set. For the NLO sample, QCD corrections were included via the aMC@NLO framework. Parton showering and hadronization were simulated with Pythia 8.308 [14] configured with the A14 tune [64] and the NNPDF2.3lo PDF set [51]. Top quarks were decayed at LO precision in both samples, using MadSpin [62] for the NLO sample, and directly at the matrix-element level for the LO sample. Bottom- and charm-hadron decays were modeled with the EvtGen program [58], using version 1.7.0 for the NLO sample and version 2.1.0 for the LO sample. Both samples were normalized to the respective cross-sections provided by the generator, which are 1.40 pb for the LO sample and 1.13 pb for the NLO sample.

An alternative parton shower NLO sample was produced using the same setup, but interfaced to HERWIG 7.2.3 [57, 65, 66] instead of PYTHIA, with the NNPDF3.0NLO [63] PDF set and the HERWIG 7.2 default set of tuned parameters [65, 66].

4.3.2 Single-top-quark t-channel NLO sample

The single-top t-channel process was modeled using the POWHEG BOX V2 [53–56] generator at NLO in QCD with the NNPDF3.0NLO [63] PDF set. For parton showering and hadronization, PYTHIA 8.230 [67] was used, configured with the A14 tune [64] and the NNPDF2.3LO [51] PDF set. Bottom- and charm-hadron decays were modeled with the EVTGEN 1.6.0 program [58]. The sample was normalized to the NLO theoretical cross-sections calculated with HATHOR 2.1 [68, 69], corresponding to 136.02 pb for single-top production and 80.95 pb for single-anti-top production.

An alternative parton shower sample was produced using the same setup, but interfaced to HERWIG 7.1.6 [57, 65, 66] instead of PYTHIA, with the NNPDF3.0NLO [63] PDF set and the HERWIG 7.1 default set of tuned parameters [65, 70].

4.3.3 Combined signal sample

To construct a stitched $tq\gamma$ sample from the available NLO and LO MC samples, events are classified based on whether the photon originates from the production or decay part of the process. This classification is performed using truth-level information and invariant mass comparisons of reconstructed particle-level objects with parton-level reference masses.

Parton level refers to the stage in event simulation where unstable particles (e.g. top quarks or W bosons) are present and decayed according to theoretical models, but before parton showering and hadronization. This level describes the hard scattering process and immediate decays.

Particle level (PL) refers to the set of stable (lifetime $\tau > 30$ ps) final-state particles that are present after the simulation of hadronization, parton showering, and hadronic decays has been performed. PL definitions are designed to closely resemble experimental observables.

To classify photons as originating from top-quark production or decay, particle-level objects are defined according to the following criteria:

Photons

- $p_{\mathrm{T}}^{\gamma} > 20\,\mathrm{GeV}$
- $|\eta^{\gamma}| < 2.5$
- $p_{\mathrm{T}}^{\mathrm{cone20}} < 0.1 \cdot p_{\mathrm{T}}^{\gamma}$ (isolation variable $p_{\mathrm{T}}^{\mathrm{cone20}}$ defined in Section 5.2)
- Must be a prompt photon (i.e. not from hadron decays or final-state radiation from hadrons)

Leptons (electron or muon)
Leptons, including electrons and muons originating from tau-lepton decays, are defined at particle level using dressed momenta, where the four-momenta of photons within $\Delta R = 0.1$ of the lepton, likely radiated from the lepton, are added to the lepton's four-momentum.

- $p_{\mathrm{T}}^{\ell} > 10\,\mathrm{GeV}$
- $|\eta^{\ell}| < 2.47$ (electrons), < 2.5 (muons)

Neutrinos

- $p_{\mathrm{T}}^{\nu} > 5\,\mathrm{GeV}$
- $|\eta^{\nu}| < 4.99$

Jets

- $p_{\mathrm{T}}^{\mathrm{jet}} > 25\,\mathrm{GeV}$
- $|\eta^{\mathrm{jet}}| < 4.5$

A procedure to match parton to particle level objects is applied as follows:

Photon: The highest-p_{T} PL photon is selected.

Lepton: The parton-level lepton from the top-quark decay is used as a reference. The closest PL lepton in ΔR is selected.

Neutrino: The parton-level neutrino is used as a reference. The closest PL neutrino in ΔR is selected.

Jet originating from a bottom quark (*b*-jet):

- The parton-level b-hadron from the top-quark decay is selected.

- Particle-level b-hadrons (so-called *ghosts* [71]) are included in the jet clustering with negligible momentum, allowing them to be associated with jets without affecting the jet momentum. The closest jet in ΔR with at least one ghost-matched b-hadron with $p_{\mathrm{T}}^{\mathrm{ghost}} > 5\,\mathrm{GeV}$ is selected.
- If no such jet exists, the closest unmatched PL jet is selected.

From the selected PL objects, four invariant mass combinations are computed for the photon (γ), the lepton (ℓ), the neutrino (ν) and the b-jet (b): $m^{\ell\nu}$, $m^{\ell\nu\gamma}$, $m^{\ell\nu b}$, and $m^{\ell\nu b\gamma}$. Depending on the photon's origin, either $m^{\ell\nu}$ or $m^{\ell\nu\gamma}$ approximates the parton-level W boson mass m^{W}_{parton}, and either $m^{\ell\nu b}$ or $m^{\ell\nu b\gamma}$ approximates the top-quark mass m^{t}_{parton}. The classification is based on:

$$|m^{\ell\nu b\gamma} - m^{t}_{\mathrm{parton}}| < |m^{\ell\nu b} - m^{t}_{\mathrm{parton}}| \tag{4.3}$$
$$|m^{\ell\nu\gamma} - m^{W}_{\mathrm{parton}}| < |m^{\ell\nu} - m^{W}_{\mathrm{parton}}| \tag{4.4}$$

If either of these conditions is satisfied, the invariant mass including the photon is closer to the corresponding parton-level mass. The photon is consequently classified as originating from the top-quark decay. This classification is applied to the $tq\gamma$ NLO sample to select production photons and to the tq sample to select decay photons. Despite the $tq\gamma$ NLO sample containing only production events, the classification is applied nevertheless to prevent any overlap with the tq sample. The resulting selected events are merged into a stitched sample that covers the complete production and decay $tq\gamma$ process. The $tq\gamma$ LO sample is used in the following for cross checks and validation.

Figure 4.1 shows the PL invariant mass distributions for events classified as decay for the tq NLO and $tq\gamma$ LO samples. The $m^{\ell\nu}$ distribution peaks near the W boson mass, reflecting events where the photon was likely not radiated during the W decay. A broad tail below the peak indicates cases where photon radiation occurred during the W decay, leading to smaller values of $m^{\ell\nu}$. In contrast, the $m^{\ell\nu\gamma}$ distribution peaks near the W mass when the photon originates from the W decay, and shows a broad tail above the peak when the photon was radiated elsewhere (e.g. from the bottom quark). The top-quark-related mass $m^{\ell\nu b}$ shows a broad distribution below the top mass due to missing photon contributions, while $m^{\ell\nu b\gamma}$ exhibits a sharp peak at the top mass when the photon is properly included. The ratio between the $tq\gamma$ LO and tq NLO samples remains relatively flat across the relevant peak and tail regions. An overall offset above unity, due to the larger NLO cross-section, is present in all subsequent ratio distributions. The normalization differences with respect to the $tq\gamma$ LO sample correspond to factors of about 1.21 for production events, 1.42 for decay events, and 1.24 for the complete stitched sample. A noticeable slope remains in the $m^{\ell\nu b\gamma}$ ratio, which warrants further validation.

Figure 4.2 shows the analogous distributions for events classified as production in the $tq\gamma$ NLO and LO samples. Here, $m^{\ell\nu}$ and $m^{\ell\nu b}$ display sharp peaks at the W and top-quark masses, consistent with the absence of photon radiation in the decay. Corresponding distributions including the photon, $m^{\ell\nu\gamma}$ and $m^{\ell\nu b\gamma}$, display broader shapes shifted above the nominal masses due to the photon's presence. The ratios are flat, indicating good agreement between the LO and NLO samples in this phase space region.

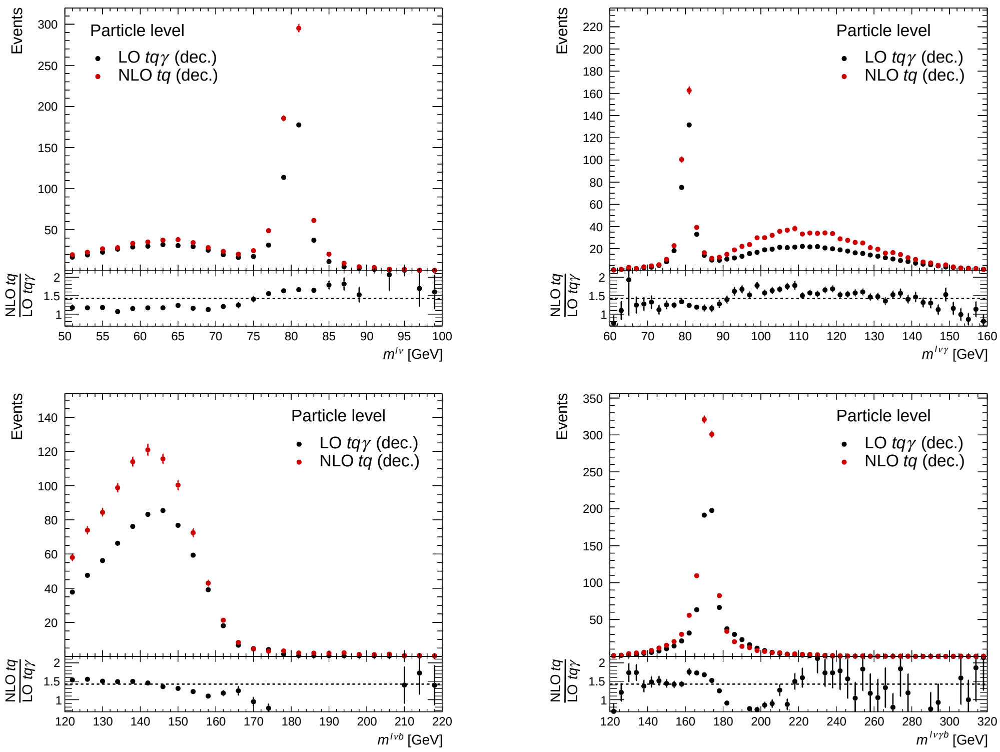

Figure 4.1: Particle-level invariant mass distributions for events classified as decay for the tq NLO and the $tq\gamma$ LO samples. The upper row presents distributions related to the W boson decay products, with $m^{\ell\nu}$ (left) and $m^{\ell\nu\gamma}$ (right), while the lower row shows the corresponding top-quark decay products, $m^{\ell\nu b}$ (left) and $m^{\ell\nu b\gamma}$ (right). The dotted lines in the ratios indicate the normalization factor between the LO and NLO contributions.

Figure 4.3 compares the stitched sample, constructed to cover the full $tq\gamma$ process, with the $tq\gamma$ LO sample as well as the individual stitched-sample constituents (production-classified $tq\gamma$ NLO and decay-classified tq NLO events). The combined invariant mass distributions exhibit the expected features. For $m^{\ell\nu}$ and $m^{\ell\nu b}$, sharp peaks from production and broad lower tails from decay are observed, while for $m^{\ell\nu\gamma}$ and $m^{\ell\nu b\gamma}$, sharp peaks from decay and broad upper tails from production are observed. Overall there is good agreement between the stitched and LO samples. While a slope remains in the $m^{\ell\nu b\gamma}$ ratio, it does not adversely affect key kinematic distributions at reconstruction or particle level, as confirmed by Figure 4.4 for p_{T}^{γ}, and by Appendix A (Figures A.1 and A.2) for p_{T}^{ℓ}, $p_{\mathrm{T}}^{\ell\nu}$, $p_{\mathrm{T}}^{\ell\nu b}$, $p_{\mathrm{T}}^{\ell\nu\gamma}$, $\Delta R(\gamma,\ell)$, $\Delta R(\gamma,b)$, and $\Delta R(\ell,b)$.

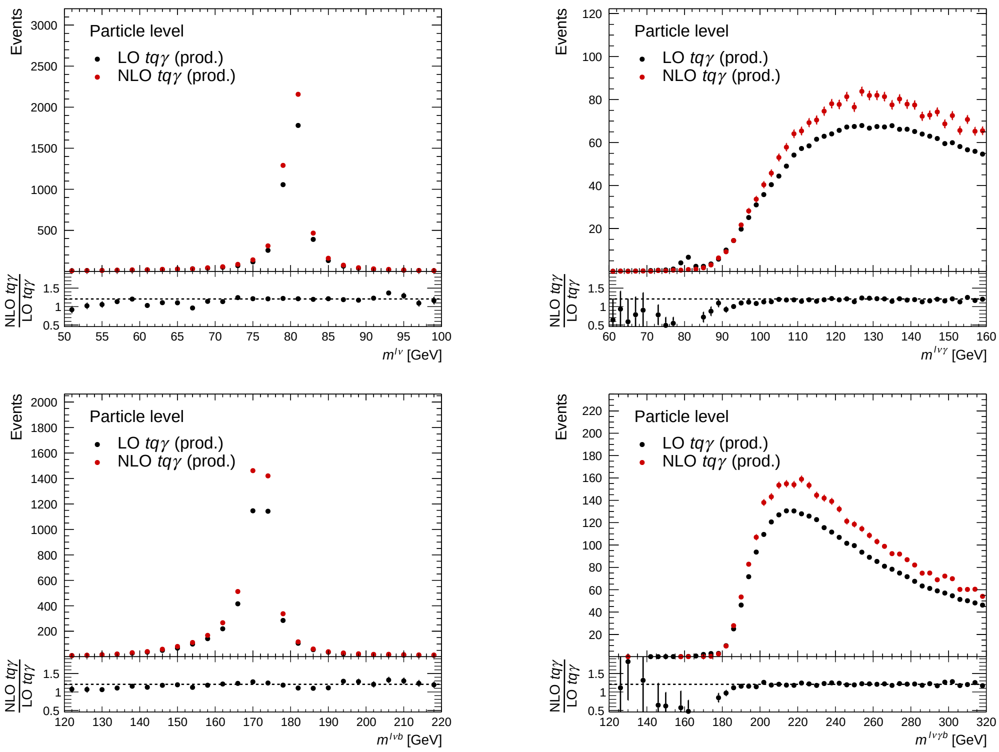

Figure 4.2: Particle-level invariant mass distributions for events classified as production for the $tq\gamma$ NLO and LO samples. The upper row presents distributions related to the W boson decay products, with $m^{\ell\nu}$ (left) and $m^{\ell\nu\gamma}$ (right), while the lower row shows the corresponding top-quark decay products, $m^{\ell\nu b}$ (left) and $m^{\ell\nu b\gamma}$ (right). The dotted lines in the ratios indicate the normalization factor between the LO and NLO contributions.

These invariant mass distributions confirm that the classification procedure successfully separates photon radiation from production and decay. No significant deviations in kinematic properties compared to the LO sample are observed in the stitched sample, supporting its further use in this analysis.

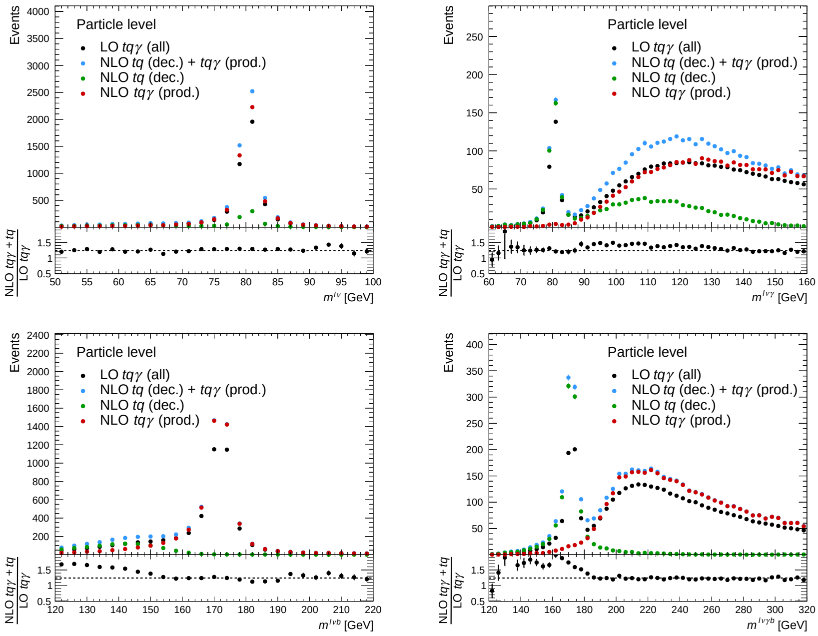

Figure 4.3: Particle-level invariant mass distributions for the $tq\gamma$ LO sample (black), the stitched sample (blue), and the tq NLO (green) and $tq\gamma$ NLO (red) constituents. The upper row presents distributions related to the W boson decay products, with $m^{\ell\nu}$ (left) and $m^{\ell\nu\gamma}$ (right), while the lower row shows the corresponding top-quark decay products, $m^{\ell\nu b}$ (left) and $m_{\ell\nu b\gamma}$ (right). The dotted lines in the ratios indicate the normalization factor between the LO $tq\gamma$ sample and the stitched NLO sample.

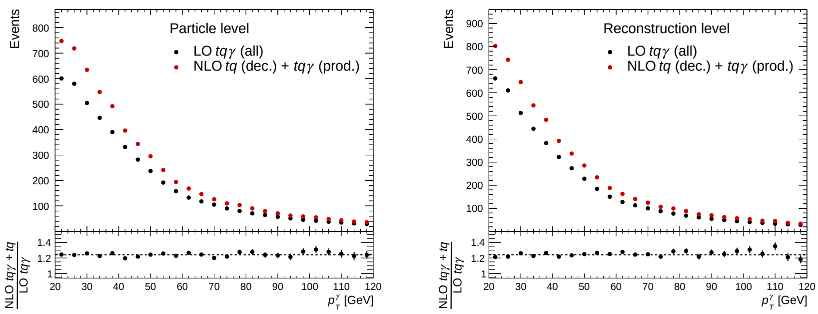

Figure 4.4: Particle-level (left) and reconstruction-level (right) photon transverse momentum p_{T}^{γ} for the $tq\gamma$ LO sample and the stitched signal sample. The lower panels show the ratios between the stitched and LO samples, which are generally flat, indicating that the stitching procedure does not distort this key kinematic property. The dotted lines in the ratios indicate the normalization factor between the LO $tq\gamma$ sample and the stitched NLO sample.

4.4 Background modeling

4.4.1 Top-quark-pair + photon sample

The $t\bar{t}\gamma$ process was modeled using two dedicated samples, one where the photon is radiated during the production of the top-quark pair (production sample) and one where the photon originates from the decay of the top quarks (decay sample). Both samples were generated with MadGraph5_aMC@NLO 2.7.3 [52] and the NNPDF3.0nlo [63] PDF set, and interfaced with Pythia 8.240 [67] for parton showering, using the A14 tune [64] and the NNPDF2.3lo [51] PDF set. Renormalization and factorization scales were set to half of the quadrature sum of the masses and transverse momenta of the particles generated at matrix element level. Bottom- and charm-hadron decays were modeled with the EvtGen 1.7.0 program [58]. The production sample was generated at NLO accuracy in QCD. The decay sample was generated at LO accuracy in QCD, due to the same constraints described in Section 4.3 for the signal sample. In the production sample, the top-quark decays were handled with MadSpin [62], while in the decay sample these decays (and any associated photon radiation) were performed directly in MadGraph5_aMC@NLO. Both samples were normalized to the cross-section provided by the generator. For the decay sample, a correction factor of 1.67 is applied so that the sum of the production and decay contributions matches the inclusive $t\bar{t}\gamma$ NLO prediction of $\sigma = 5.35\,\text{pb}$ according to Ref. [72].

Alternative parton shower samples were produced using the same setup, but interfaced to Herwig 7.2.1 [57, 65, 66] instead of Pythia, with the NNPDF3.0nlo [63] PDF set and the Herwig 7.1 default set of tuned parameters [65, 70].

4.4.2 Top-quark-pair sample

The $t\bar{t}$ process was modeled using the Powheg Box v2 [53–56] generator at NLO with the NNPDF3.0nlo [63] PDF set. The renormalization and factorization scales were set dynamically to $\mu_{\mathrm{R}} = \mu_{\mathrm{F}} = \sqrt{(m^t)^2 + (p_{\mathrm{T}}^t)^2}$, where m^t and p_{T}^t denote the mass and transverse momentum of the top quark. The events were interfaced to Pythia 8.230 [67] to model the parton shower, hadronization, and underlying event, using the A14 tune [64] and the NNPDF2.3lo [51] set of PDFs. Bottom- and charm-hadron decays were modeled with the EvtGen 1.6.0 program [58]. The sample where at least one of the top quarks decays hadronically was normalized to $\sigma = 453.64\,\text{pb}$, the theoretical cross-section at next-to-next-to-leading order (NNLO) in QCD, including the resummation of next-to-next-to-leading logarithmic (NNLL) soft-gluon terms, calculated using Top++ 2.0 [73]. The uncertainties arising from the PDF and the strong coupling constant are evaluated following the PDF4LHC15 prescription [74] using the MSTW2008NNLO [75, 76], CT10NNLO [77, 78], and NNPDF2.3LO [51] PDF sets. The total uncertainty on the cross-section of the inclusive sample is about 6%.

Alternative parton shower samples were produced using the same setup, but interfaced to Herwig 7.1.3 [57, 65, 70] instead of Pythia, with the NNPDF3.0NLO [63] PDF set and the Herwig 7.1 default set of tuned parameters [65, 70]. Additional samples with varied top-quark masses (172 GeV and 173 GeV instead of the nominal mass of 172.5 GeV) were also generated.

4.4.3 Single-top-quark samples

A total of three separate processes are used to describe single-top-quark production, which are the single-top t-channel process, s-channel process, and single-top production in association with a W boson (tW). The modeling of the single-top t-channel process has already been described in Section 4.3.2. The single-top s-channel process was modeled using the Powheg Box v2 [53–56] generator at NLO in QCD with the NNPDF3.0NLO [63] PDF set. For parton showering and hadronization, Pythia 8.230 [67] was used, configured with the A14 tune [64] and the NNPDF2.3LO [51] PDF set. Bottom- and charm-hadron decays were modeled with the EvtGen 1.6.0 program [58]. The single-top tW production was modeled at NLO in QCD as well but instead using Pythia 8.309 [14] and EvtGen 2.1.1 [58]. To avoid double counting of events that overlap with the $t\bar{t}$ process, the diagram removal scheme was applied [79]. All single-top-quark samples were normalized to their NLO theoretical cross-section prediction.

4.4.4 Vector-boson + jets + photon samples

Samples of $W\gamma$+jets and $Z\gamma$+jets events were simulated using Sherpa 2.2.14 [59, 80] with the Comix [81] and OpenLoops [82–84] libraries for matrix element calculations. The NNPDF3.0NNLO [63] PDF set was used. Matrix element calculations included contributions with up to one jet at NLO in QCD and up to four additional jets at LO, matched with the parton shower using the MEPS@NLO [85, 86] scheme and the CKKW merging prescription [87] to avoid double counting between matrix element and parton shower emissions. The simulation was interfaced to the Sherpa parton shower, and all samples were normalized to the cross-sections provided by the generator.

4.4.5 Vector-boson + jets samples

Samples of W+jets and Z+jets events were simulated using Sherpa 2.2.11 [59, 80] (version 2.2.14 for $Z \to \tau\tau$) with the Comix [81] and OpenLoops [82–84] libraries. The NNPDF3.0nnlo [63] PDF set was used, and matrix element calculations included up to two partons at NLO in QCD and up to five additional partons at LO, matched with the parton shower using the MEPS@NLO scheme [85, 86] and the CKKW prescription [87] to avoid double counting. The simulation was interfaced to the Sherpa parton shower, and all samples were normalized to the cross-sections provided by the generator.

The Z+jets samples using an alternative MC generator were simulated with MadGraph5_aMC@NLO 2.9.5 [52]. Matrix elements with one additional jet were simulated at NLO in QCD, and with up to three additional jets at LO. The events were interfaced to Pythia 8.245 for parton showering and hadronization, using the NNPDF2.3lo [51] PDF set with the A14 tune [64], and to EvtGen 1.7.0 [58] for bottom- and charm-hadron decays. The samples were normalized to the cross-sections provided by the generator.

4.5 Modeling of samples used for the photon ID efficiency measurement via the Matrix Method

4.5.1 Photon + jet samples

Photon + jet samples were produced using Pythia 8.244 [67], configured with the A14 tune [64] and the NNPDF2.3lo [51] PDF set for the matrix element calculation and the simulation of parton shower, hadronization, and decays with LO precision in QCD. Bottom- and charm-hadron decays were modeled with the EvtGen 1.7.0 program [58]. The samples were normalized to the cross-sections provided by the generator.

4.5.2 Dijet samples

The Dijet samples were produced using Pythia 8.186 [49], configured with the A14 tune [64] and the NNPDF2.3lo [51] PDF set for the matrix element calculation and the simulation of parton shower, hadronization, and decays with LO precision in QCD. Bottom- and charm-hadron decays were modeled with the EvtGen 1.2.0 program [58]. The samples were normalized to the cross-sections provided by the generator.

5 Object reconstruction

A wide range of particles is produced at the interaction point, many of which are short-lived and decay before reaching the ATLAS detector. The prompt particles (those that originate directly from the hard-scattering process or from the immediate decay of W, Z, and Higgs bosons and top quarks) that do reach the detector include electrons, muons, photons, neutrinos, and hadrons. Objects known as jets are reconstructed from collimated sprays of hadrons originating from quarks and gluons produced in the hard-scattering process. The process of object reconstruction involves identifying and classifying these particles using the information recorded in the Inner Detector, the calorimeters, and the muon spectrometer. Dedicated algorithms are designed to maximize identification efficiency while minimizing misidentification. The reconstruction of various physics objects is described in the following sections.

5.1 Tracks

The tracks of charged particles are reconstructed using hits from the Inner Detector (ID) subsystems (Section 3.2.2), as described in detail in Refs. [88, 89]. The reconstruction begins with the identification of hit clusters in the pixel and strip detectors, which are combined into track seeds. These seeds are extended outward through the silicon detectors and, when possible, into the transition radiation tracker. Candidate tracks are iteratively fitted with a Kalman filter [90] to refine the trajectory and momentum estimate. Ambiguities from overlapping track candidates are resolved using quality criteria based on the number of hits and the fit quality.

Reconstructed tracks are required to satisfy quality requirements. These typically include a minimum transverse momentum of a few hundred MeV, a pseudorapidity within the Inner Detector acceptance ($|\eta| < 2.5$), a sufficient number of hits in the silicon detectors (Pixel and SCT), constraints on the transverse and longitudinal impact parameters with respect to the primary vertex, and a reasonable fit quality. The resulting tracks are used in the reconstruction of higher-level objects such as charged leptons and jets.

Separately, additional tracks are reconstructed in the muon spectrometer system (Section 3.2.4). Hits from the muon chambers are combined to form track candidates, which are fitted to determine their trajectory and momentum. Quality criteria such as the number of associated hits and geometric consistency are applied to select well-reconstructed muon spectrometer tracks [91].

5.2 Object isolation

Isolation requirements are applied to electron, muon, and photon candidates in order to suppress non-prompt candidates originating from sources such as hadron decays inside jets or from pile-up interactions. Prompt candidates produced in hard-scattering processes are typically well isolated from other particles, while backgrounds are often accompanied by additional nearby track and calorimeter activity.

Isolation in the ATLAS detector is based on the activity measured in a cone of size ΔR around reconstructed objects. Both track-based and calorimeter-based isolation variables are used. Track-based isolation is constructed from the scalar sum of transverse momenta p_{T} of ID tracks satisfying quality requirements and associated with the primary vertex, within the cone and excluding tracks associated with the object itself. Calorimeter-based isolation variables are defined using the transverse energy E_{T} deposited in calorimeter cells within the cone around the object, excluding the object core and correcting for pile-up contributions.

For electrons and muons, track isolation requirements are commonly defined using variable-size cones that shrink with increasing transverse momentum, ensuring stable efficiency for high-p_{T} objects. For photons, fixed-cone isolation requirements are used. The track isolation variables are denoted by $p_{\mathrm{T}}^{\mathrm{cone}X}$ and $p_{\mathrm{T}}^{\mathrm{varcone}X}$, and analogously with E_{T} for calorimeter-based isolation variables, where X specifies the reference cone size. For fixed-cone isolation, the cone size is defined as $\Delta R = X/100$. For variable-cone isolation, the cone size is defined as

$$\Delta R = \min\left(\frac{10}{p_{\mathrm{T}}^{\mathrm{obj}}\ [\mathrm{GeV}]}, \frac{X}{100}\right), \tag{5.1}$$

where $p_{\mathrm{T}}^{\mathrm{obj}}$ is the transverse momentum of the reconstructed object. Different working points (WPs) define different thresholds on these quantities, providing a trade-off between background rejection and signal efficiency. In this thesis, the isolation WPs definded in Table 5.1 are used.

Table 5.1: Isolation working points used in this thesis. The definitions and numerical values follow Run 2 recommendations and Refs. [91, 92].

Candidate	Working point	Track requirement	Calorimeter requirement
electron (el)	*Tight_VarRad*	$p_{\mathrm{T}}^{\mathrm{varcone30}} < 0.06\, p_{\mathrm{T}}^{e}$	$E_{\mathrm{T}}^{\mathrm{cone20}} < 0.06\, p_{\mathrm{T}}^{e}$
muon (μ)	*Tight*	$p_{\mathrm{T}}^{\mathrm{varcone30}} < 0.04\, p_{\mathrm{T}}^{\mu}$	$E_{\mathrm{T}}^{\mathrm{cone20}} < 0.15\, p_{\mathrm{T}}^{\mu}$
photon (γ)	*FixedCutTight*	$p_{\mathrm{T}}^{\mathrm{cone20}} < 0.05\, p_{\mathrm{T}}^{\gamma}$	$E_{\mathrm{T}}^{\mathrm{cone40}} < 0.022\, p_{\mathrm{T}}^{\gamma} + 2.45\,\mathrm{GeV}$
photon (γ)	*FixedCutLoose*	$p_{\mathrm{T}}^{\mathrm{cone20}} < 0.05\, p_{\mathrm{T}}^{\gamma}$	$E_{\mathrm{T}}^{\mathrm{cone40}} < 0.065\, p_{\mathrm{T}}^{\gamma}$

5.3 Electrons and Photons

Electrons are reconstructed in the ATLAS detector by matching clusters of energy deposits in the electromagnetic calorimeter to charged-particle tracks reconstructed in the ID. The matching is based on the spatial compatibility between the extrapolated track and the cluster position, as well as consistency between the track momentum and the cluster energy. If multiple tracks are compatible with a given cluster, the best-matched candidate is selected using predefined quality criteria. The full reconstruction algorithm is described in detail in Ref. [93].

Electron isolation and identification criteria are applied to suppress backgrounds from sources such as hadrons misidentified as electrons, electrons originating from photon conversions, and electrons from heavy-flavor decays. In this thesis, electrons are required to satisfy the *Tight_VarRad* isolation WP defined in Table 5.1 and the *Tight* identification WP defined in Ref. [93]. The *Tight* identification WP combines information from track quality, track-to-cluster matching variables and high-level *shower shape variables* (SSVs) [93, 94]. The SSVs describe the lateral and longitudinal development of the calorimeter clusters, including variables describing the energy leakage into the hadronic calorimeter. The selection thresholds are optimized separately for different electron transverse momentum and pseudorapidity ranges.

Additional impact parameter requirements are applied to further suppress non-prompt electrons. These requirements are $|d_0/\sigma(d_0)| < 5$ and $|z_0| \sin\theta < 0.5\,\mathrm{mm}$, where d_0 is the transverse impact parameter, defined as the distance of closest approach of the track to the primary vertex in the transverse plane (the track perigee), $\sigma(d_0)$ its uncertainty, and z_0 the longitudinal impact parameter, defined as the separation along the beam axis between the primary vertex and the perigee point. Electron candidates are furthermore required to satisfy $p_{\mathrm{T}}^{e} > 10\,\mathrm{GeV}$ and to have an absolute pseudorapidity of the associated calorimeter cluster $|\eta_{\mathrm{cl}}^{e}| < 2.47$, excluding the transition region $1.37 < |\eta_{\mathrm{cl}}^{e}| < 1.52$ between the barrel and end-cap calorimeters.

Photon candidates are reconstructed from electromagnetic calorimeter clusters and are classified as unconverted or converted depending on whether a conversion into an $e^{+}e^{-}$ pair occurs before reaching the calorimeter. Unconverted photons leave no track in the ID. Converted photons are associated with one or two ID tracks consistent with a conversion vertex. Based on the number and type of associated tracks, converted photons are further classified into five distinct conversion types, summarized in Table 5.2.

Photon isolation and identification are performed using the *FixedCutTight* and *FixedCutLoose* isolation WPs defined in Table 5.1 and the *Loose* and *Tight* identification WPs from Ref. [93]. The identification WPs are based on cut-based selections on SSVs, with thresholds optimized separately for different photon transverse momentum and pseudorapidity ranges as well as separately for converted and unconverted photons. The *Tight* WP provides stronger rejection of backgrounds such as jets with large electromagnetic energy fractions and neutral meson decays, such as $\pi^0 \to \gamma\gamma$. The *Loose* WP provides high efficiency and is typically used for control regions enriched in non-prompt or misidentified photon candidates. Additionally, all photons are required to satisfy $p_{\mathrm{T}}^{\gamma} > 20\,\mathrm{GeV}$ and $|\eta_{\mathrm{cl}}^{\gamma}| < 2.37$.

Table 5.2: Photon conversion types, defined by the number and location of associated tracks in the Inner Detector. "Si" refers to silicon detectors (pixel and SCT), and "TRT" refers to the transition radiation tracker.

Conversion type	Number of tracks	Track properties
Unconverted	0	–
SingleSi	1	With SCT hits
SingleTRT	1	Only TRT hits
DoubleSi	2	Both with SCT hits
DoubleTRT	2	Both only with TRT hits
DoubleSiTRT	2	One with SCT hits, one with only TRT hits

5.4 Muons

Muons are reconstructed in the ATLAS detector by combining information from the Inner Detector and the muon spectrometer. Tracks in both subsystems are reconstructed independently and then matched. In this thesis, the *Tight* isolation WP defined in Table 5.1 and the *Medium* identification WP from Ref. [91] are used.

The *Medium* identification WP applies quality requirements on muon candidates, including requirements on the number of associated hits in the ID, the quality of the combined track fit used to match the ID and muon spectrometer tracks, and consistency between the two subsystem momentum measurements. Impact parameter requirements are applied to reject muons from sources such as hadron decays, pile-up and cosmic rays. These requirements are $|d_0/\sigma(d_0)| < 3$ for the transverse impact parameter d_0 and its significance $\sigma(d_0)$, and $|z_0|\sin\theta < 0.5\,\mathrm{mm}$ for the longitudinal impact parameter z_0. Additionally, muons are required to have transverse momentum $p_{\mathrm{T}}^{\mu} > 10\,\mathrm{GeV}$ and pseudorapidity $|\eta^{\mu}| < 2.5$.

5.5 Jets and *b*-tagging

Jets are collimated sprays of particles that arise from the hadronization and subsequent decays of quarks or gluons. Their reconstruction in the ATLAS detector uses the *particle flow* algorithm [95], which combines ID tracks and calorimeter energy clusters associated with jets. These objects are clustered into calorimeter jets using the anti-k_t algorithm [96] with a radius parameter of $R = 0.4$. In this analysis, jets are required to satisfy $p_{\mathrm{T}}^{\mathrm{jet}} > 25\,\mathrm{GeV}$ and $|\eta^{\mathrm{jet}}| < 4.5$. To suppress jets originating from pile-up interactions, a multivariate Jet Vertex Tagger (JVT) [97] is applied to jets with $p_{\mathrm{T}}^{\mathrm{jet}} < 60\,\mathrm{GeV}$ and $|\eta^{\mathrm{jet}}| < 2.4$.

Jets likely originating from hadrons containing a bottom quark (b-hadrons) are identified (b-tagged) using the GN2 algorithm [13]. GN2 is a Transformer-based jet flavor tagging algorithm that processes tracks associated with a jet as a sequence of inputs and learns from their spatial and kinematic relationships. Compared to other hadrons, b-hadrons have a relatively long lifetime, typically of around $\tau \approx 1.5\,\mathrm{ps}$ [7]. As a result, they often travel a measurable distance of order $\mathcal{O}(1\,\mathrm{mm})$ before decaying, leading to secondary vertices that can be reconstructed within the ID. The GN2 algorithm exploits this and other features, such as high track multiplicity and invariant mass of decay products, to assign a discriminant score to each jet. Different WPs are defined by applying thresholds on this score. Common choices in ATLAS studies are the 65%, 70%, 77%, 85%, and 90% WPs. These values refer to the efficiency of correctly identifying truth-labelled b-jets with transverse momentum $p_{\mathrm{T}}^{b} > 20\,\mathrm{GeV}$ in simulated $t\bar{t}$ events. For example, the 70% WP retains 70% of true b-jets, with stronger rejection of c-jets and light-flavor jets compared to looser WPs like 90%. In this analysis, the 70% efficiency WP is used as the primary b-jet definition. In simulated $t\bar{t}$ events, this WP corresponds to a c-jet mis-tag efficiency of about 2% and a light-flavor mis-tag efficiency of about 0.06%, equivalent to rejection factors of about 50 and 1700, respectively. Looser WPs are used in this analysis to define control regions and veto additional b-jets.

5.6 Missing transverse momentum

Neutrinos escape detection in the ATLAS detector due to their weakly interacting nature. Since the detector provides nearly full solid-angle coverage around the interaction point, their presence can be inferred from an imbalance in the total transverse momentum of visible particles in an event. This quantity, denoted as $E_{\mathrm{T}}^{\mathrm{miss}}$, is reconstructed as the magnitude of the negative vector sum of the transverse momenta of all calibrated physics objects, along with a term that accounts for low-p_{T} tracks not associated with any of these objects [98]:

$$E_{\mathrm{T}}^{\mathrm{miss}} = \left| \sum_{\text{objects}} \left(-\vec{p}_{\mathrm{T}}^{\,\text{object}} \right) + \sum_{\substack{\text{unused} \\ \text{tracks}}} \left(-\vec{p}_{\mathrm{T}}^{\,\text{track}} \right) \right| \tag{5.2}$$

5.7 Object overlap removal

Since different physics objects are reconstructed independently in the ATLAS detector while using the same detector signals, the same energy deposits or tracks can sometimes contribute to more than one object. For example, a single energy cluster in the calorimeter could be reconstructed simultaneously as an electron, a photon, and a jet. To avoid double counting and ensure a consistent event interpretation, a sequential *overlap removal* procedure is applied.

The procedure compares pairs of object types and removes one of the two objects if they are found to overlap geometrically, typically defined using the distance ΔR in (η, ϕ) space. The order of comparisons and the choice of which object to remove is predefined according to physics priority. For instance, jets overlapping with electrons within $\Delta R < 0.2$ are removed, while subsequently electrons overlapping with surviving jets within $\Delta R < 0.4$ are discarded. Similar rules are applied for muons, photons, and taus, ensuring that each reconstructed object in the final event is uniquely defined. The overlap removal procedure applied in this analysis follows the sequence outlined below:

1. Any calorimeter-tagged muon sharing a track with an electron is removed.
2. Any electron sharing a track with a muon is removed.
3. Jets within $\Delta R < 0.2$ of an electron are removed.
4. Electrons within $\Delta R < 0.4$ of surviving jets are removed.

5. Jets with fewer than three associated tracks within $\Delta R < 0.2$ of a muon are removed.
6. Muons within $\Delta R < 0.4$ of surviving jets are removed.
7. Tau leptons within $\Delta R < 0.2$ of an electron or a muon with $p_{\mathrm{T}}^{\mu} > 2\,\mathrm{GeV}$ are removed (for tau leptons with $p_{\mathrm{T}}^{\tau} > 50\,\mathrm{GeV}$, the muon must be a combined-type muon, i.e., reconstructed using both the Inner Detector and muon spectrometer).
8. Jets within $\Delta R < 0.2$ of a tau lepton are removed.
9. Photons within $\Delta R < 0.4$ of an electron or muon are removed.
10. Jets within $\Delta R < 0.4$ of a photon are removed.

5.8 Changes in the reconstruction software compared to the previous inclusive measurement

For this thesis, an updated ATLAS software release is used, corresponding to several changes in the reconstruction configuration. The main motivation for this transition is the need for robustness against the higher instantaneous luminosity and pile-up conditions anticipated for Run 3, as well as improvements in computational performance and long-term software maintainability. While the overall reconstruction strategy remains unchanged, the updated software incorporates numerous refinements and algorithmic updates across several detector subsystems. As a result, the reconstruction of higher-level objects such as leptons, photons, jets, and missing transverse momentum is affected.

A major set of updates concerns the reconstruction of tracks in the Inner Detector. Compared to the previous release, tighter requirements are applied to track candidates, including an increased minimum transverse momentum threshold (from previously 400 MeV to 500 MeV) and stricter conditions on the number of associated hits in the silicon detectors (requiring eight hits instead of previously seven). These changes suppress low-quality tracks, which predominantly originate from pile-up interactions or random combinations of detector hits [11]. The reconstruction of primary vertices is also improved by replacing the iterative vertex finder (IVF) [99] with the updated adaptive multi-vertex finder (AMVF) [12] algorithm, which employs an approach in which multiple vertex candidates compete for tracks. This algorithm enhances the separation of closely spaced vertices separated by a millimeter or less, which were previously often merged. The AMVF algorithm achieves an approximately 5% higher fraction of events in which the hard-scatter primary vertex is correctly identified and reconstructed. These enhancements in vertex resolution and purity are essential for accurate impact parameter-based selections and effective pile-up mitigation.

The previously described GN2 algorithm is another important addition in the updated reconstruction software, replacing the previously used DL1r flavor-tagging algorithm [100]. The DL1r feed-forward Neural Network algorithm relies on high-level input variables derived from the outputs of lower-level b-tagging algorithms [101–103]. In contrast, GN2 processes track and vertex information directly and can better exploit correlations between tracks within a jet, leading to significantly improved rejection of c-jets and light-flavor jets.

Overall, the updates introduced with the new reconstruction setup lead to improved vertex reconstruction, a reduced rate of misreconstructed *fake* tracks while maintaining a similar efficiency for tracks originating from the primary interaction, as well as improved energy and momentum measurements, especially in high-activity events. Due to the changed reconstruction conditions, the calibration, the identification criteria, and the WPs were redone and reoptimized by the ATLAS collaboration. Consequently, the full analysis chain, including the stitching procedure for the signal sample, as well as the estimation of backgrounds with non-prompt photons and the signal separation, is reimplemented and revalidated, as described in the following chapters.

6 Measurement of photon identification efficiencies with the ATLAS detector

Most photons reconstructed in the ATLAS detector are not prompt. Instead, they predominantly originate from hadronic processes such as neutral pion decays, or are misidentified objects like hadronic jets or electrons. To distinguish prompt photons from these backgrounds, a combination of isolation requirements and identification (ID) criteria is employed.

The methodology described in this chapter closely follows that of previously published ATLAS measurements of the photon identification efficiency performed using the full Run 2 dataset [92]. The presented measurement was performed in the context of the major software update described in Section 5.8, which affected various aspects of object reconstruction and necessitated substantial technical updates and validation to ensure consistency with the new framework and conditions.

The ATLAS photon ID is based on rectangular cuts applied to a set of shower shape variables (SSVs), which describe the lateral and longitudinal development of the electromagnetic shower in the calorimeter system. These variables are defined from clusters in the calorimeter system, as described in Section 5.3. An overview of the SSVs used in the *Tight* photon ID working point (WP) is given in Table 6.1.

The SSVs used in the *Tight* photon ID WP are grouped into two categories:

- **Narrow-strip variables**
  SSVs that describe the inner core of the calorimeter shower
  $(f_{\text{side}}, \omega_{s,3}, \Delta E, E_{\text{ratio}})$
- **Relaxed-tight variables**
  All remaining SSVs used in the *Tight* photon ID WP
  $(R_{\text{had}_{(1)}}, R_\phi, R_\eta, \omega_{\eta 2}, \omega_{s,\text{tot}}, f_1)$

The rectangular cuts on these variables are optimized in separate bins of photon conversion status, transverse energy E_{T}^{γ}, and absolute pseudorapidity $|\eta^{\gamma}|$, using the *Toolkit for Multivariate Data Analysis* (TMVA) package [104].

Due to known mismodeling of SSVs in simulation, corrections referred to as *fudge factors* [93, 105] are applied to photons in MC samples. These corrections shift the mean value of the SSV distributions as well as stretch their width to improve the agreement with the distributions observed in data. These corrections are derived in bins of the same kinematic and conversion categories as the photon ID cut values. The fudge factors improve the agreement between data and simulation but residual shape mismodeling or mismodeling of correlations between variables remains.

Therefore, in order to validate the photon ID performance in data and to derive data-to-MC scale factors that correct for residual mismodeling in simulation, the photon identification efficiency is measured using data-driven methods. The measurements are performed in eighteen E_{T}^{γ} bins, six bins of pseudorapidity of the calorimeter cluster associated with the photon $|\eta_{\mathrm{cl}}^{\gamma}|$, and separately for converted photons (those that convert into an $e^{+}e^{-}$ pair before reaching the calorimeter system) and unconverted photons:

- E_{T}^{γ} bin edges:
  $\{8, 10, 15, 20, 25, 30, 35, 40, 45, 50, 60, 80, 100, 125, 150, 175, 250, 350, \infty\}$ GeV
- $|\eta_{\mathrm{cl}}^{\gamma}|$ bins: $[0, 0.6), [0.6, 0.8), [0.8, 1.37), (1.52, 1.81), [1.81, 2.01), [2.01, 2.37]$
- photon conversion status: converted, unconverted

The $|\eta_{\mathrm{cl}}^{\gamma}|$ binning is chosen to follow the geometry of the ATLAS electromagnetic calorimeter and the distribution of passive material in front of it. The barrel region is divided into three $|\eta_{\mathrm{cl}}^{\gamma}|$ bins, separating the central barrel from regions with increasing material budget, while the end-cap region is similarly subdivided into three bins to account for changes in calorimeter geometry and material distribution at larger pseudorapidity. The barrel-end-cap transition region $(1.37 < |\eta_{\mathrm{cl}}^{\gamma}| < 1.52)$ is excluded due to reduced calorimeter coverage, strongly varying amounts of passive material, and generally degraded photon ID performance.

Three complementary methods are employed, respectively targeting the low, medium and high photon energy ranges. In the following, the former two methods are briefly summarized. The latter is described afterward in detail and results for the full Run 2 measurement under updated software and reconstruction conditions are presented. The combined results of all three methods provide a comprehensive measurement of the photon ID efficiency across the full kinematic range relevant for physics analyses performed by the ATLAS collaboration.

Table 6.1: Shower shape variables used for photon identification. For those computed in the first electromagnetic calorimeter layer, if the cluster spans multiple cells in the ϕ direction at a given η position, the two cells closest to the cluster barycenter in ϕ are merged and the variables are computed from this merged cell [93].

Category	Description	Name
Hadronic leakage	Ratio of E_T in the first layer of the hadronic calorimeter to E_T of the EM cluster (used over the ranges $\|\eta\| < 0.8$ and $\|\eta\| > 1.37$)	R_{had_1}
	Ratio of E_T in the hadronic calorimeter to E_T of the EM cluster (used over the range $0.8 < \|\eta\| < 1.37$)	R_had
ECAL middle layer	Ratio of the sum of the energies of the cells contained in a 3×7 $\eta \times \phi$ rectangle (measured in cell units) to the sum of the cell energies in a 7×7 rectangle, both centered around the most energetic cell	R_η
	Lateral shower width, $\sqrt{(\Sigma E_i \eta_i^2)/(\Sigma E_i) - (\Sigma E_i \eta_i)/(\Sigma E_i)^2}$, where E_i is the energy and η_i is the pseudorapidity of cell i and the sum is calculated within a window of 3×5 cells	$\omega_{\eta 2}$
	Ratio of the sum of the energies of the cells contained in a 3×3 $\eta \times \phi$ rectangle (measured in cell units) to the sum of the cell energies in a 3×7 rectangle, both centered around the most energetic cell	R_ϕ
ECAL strip layer	Total lateral shower width, $\sqrt{(\Sigma E_i (i - i_\mathrm{max}))/(\Sigma E_i)}$, where i runs over all cells in a window of $\Delta\eta \approx 0.0625$ and i_max is the index of the highest-energy cell	$\omega_{s,\mathrm{tot}}$
	Lateral shower width, $\sqrt{(\Sigma E_i (i - i_\mathrm{max}))/(\Sigma E_i)}$, where i runs over all cells in a window of 3 cells around the highest-energy cell	$\omega_{s,3}$
	Energy fraction outside core of three central cells, within seven cells	f_side
	Difference between the energy of the cell associated with the second maximum, and the energy reconstructed in the cell with the smallest value found between the first and second maxima	ΔE
	Ratio of the energy difference between the maximum energy deposit and the energy deposit in a secondary maximum in the cluster to the sum of these energies	E_ratio
	Ratio of the energy measured in the first layer of the ECAL to the total energy of the EM cluster	f_1

6.1 Low photon energies

At low photon transverse energies ($8\,\mathrm{GeV} \leq E_\mathrm{T}^\gamma \leq 100\,\mathrm{GeV}$), the photon ID efficiency is measured using the *Radiative Z Method* [94], which uses a sample enriched in prompt photons from Z boson decays ($Z \to \ell\ell\gamma$), where $\ell = (e, \mu)$. By selecting events with a well-identified dilepton pair and a photon, and requiring the three-body invariant mass $m_{ll\gamma}$ to be consistent with the Z boson mass, a high-purity prompt-photon sample is obtained.

First, the prompt-photon purity both before and after applying the photon ID cuts is estimated using two complementary methods, a template fit to the $m_{ll\gamma}$ distribution, and a fully data-driven method based on signal and control regions defined by photon isolation requirements. The two results are combined into a weighted average to obtain the final purity estimate. The photon ID efficiency $\varepsilon^{\mathrm{ID}}_{\mathrm{prompt}}$ is then computed as the fraction of prompt-photon events passing the ID criteria out of all prompt photons in the selected sample, according to

$$\varepsilon^{\mathrm{ID}}_{\mathrm{prompt}} = \frac{P^{\mathrm{ID}}_{\mathrm{prompt}} \cdot N^{\mathrm{ID}}_{\gamma}}{P_{\mathrm{prompt}} \cdot N_{\gamma}}. \tag{6.1}$$

Here and in the following, the superscript ID indicates that the *Tight* photon ID requirement is passed. The subscript γ represents all photon candidates, while the subscript *prompt* represents prompt photons. The subscript *fake* is used in the following to represent non-prompt and misidentified photons (fake photons). Accordingly, N_{γ} and N^{ID}_{γ} are the number of photon candidates before and after applying the *Tight* ID selection, respectively, and P_{prompt} and $P^{\mathrm{ID}}_{\mathrm{prompt}}$ are the corresponding prompt-photon purities in the full dataset. The same formula is also used by the medium- and high-photon-energy methods described in the following. To account for the mismodeling of photon ID efficiencies in simulation, data-to-MC scale factors (SFs) are computed as

$$\mathrm{SF}^{\mathrm{ID}}_{\mathrm{prompt}} = \frac{\varepsilon^{\mathrm{ID}}_{\mathrm{prompt}}}{\varepsilon^{\mathrm{ID,MC}}_{\gamma}}. \tag{6.2}$$

6.2 Medium photon energies

At intermediate photon transverse energies ($25\,\mathrm{GeV} \leq E^{\gamma}_{\mathrm{T}} \leq 150\,\mathrm{GeV}$), the photon ID efficiency is measured using the *Electron Extrapolation Method* [94], which exploits the similarity between electromagnetic showers initiated by photons and electrons in the ATLAS calorimeters. A clean sample of electron candidates is selected using a tag-and-probe technique [106] in $Z \to e^{+}e^{-}$ events, where one electron (the tag) passes tight electron ID and trigger requirements, and the other (the probe) is used to emulate a photon.

To estimate the photon ID efficiency for prompt photons, the SSVs of the probe electrons are transformed using a Smirnov transformation [107] derived from simulation, which for each SSV x maps the cumulative distribution function of electrons $\mathrm{CDF}_e(x)$, onto that of photons, $\mathrm{CDF}_\gamma(x)$, via a mapping $f(x)$ defined by $\mathrm{CDF}_e(x) = \mathrm{CDF}_\gamma(f(x))$, effectively transforming the probe electrons to have photon-like shower shapes. After applying these transformations, the photon ID criteria are applied to the probe electrons, and the efficiency is defined as the fraction of probe electrons that pass the photon ID criteria. Corrections are applied for background contamination and possible mismodeling in simulation.

6.3 High photon energies

At high photon transverse energies ($E_\mathrm{T}^\gamma \geq 25\,\mathrm{GeV}$), the photon ID efficiency is measured using the *Matrix Method* (sometimes called *Inclusive Photons Method*) [94, 108]. This method exploits differences in the track isolation properties between prompt photons and fake photons to extract the purity of selected photon samples and thereby determine the efficiency of the *Tight* photon ID selection, according to Equation (6.1).

The purities are derived using photon track-isolation efficiencies $\hat{\varepsilon}$:

$$P_\mathrm{prompt} = \frac{\hat{\varepsilon}_\gamma - \hat{\varepsilon}_\mathrm{fake}}{\hat{\varepsilon}_\mathrm{prompt} - \hat{\varepsilon}_\mathrm{fake}}, \tag{6.3}$$

$$P_\mathrm{prompt}^\mathrm{ID} = \frac{\hat{\varepsilon}_\gamma^\mathrm{ID} - \hat{\varepsilon}_\mathrm{fake}^\mathrm{ID}}{\hat{\varepsilon}_\mathrm{prompt}^\mathrm{ID} - \hat{\varepsilon}_\mathrm{fake}^\mathrm{ID}}. \tag{6.4}$$

A photon candidate is considered to be isolated if there are no tracks with a transverse momentum $p_\mathrm{T}^\mathrm{track} > 1\,\mathrm{GeV}$ within a radius of $R = 0.4$ around the candidate.

The track isolation efficiencies for all photon candidates, $\hat{\varepsilon}_\gamma$ and $\hat{\varepsilon}_\gamma^\mathrm{ID}$, are measured in data. The corresponding efficiencies for prompt photons, $\hat{\varepsilon}_\mathrm{prompt}$ and $\hat{\varepsilon}_\mathrm{prompt}^\mathrm{ID}$, are obtained from simulation, using the γ+jet MC samples described in Section 4.5.1. The track isolation efficiencies for fake photons are estimated using a data-driven approach. This is motivated by the rapidly decreasing fraction of fake photons at high photon transverse energies, which makes the generation of MC samples with sufficient statistical precision impractical. In addition, the fake-photon contributions and their isolation properties are not reliably modeled in simulation. Therefore, the fake-photon track isolation efficiencies are determined in data using non-*Tight*-ID regions, enriched in fake photons, as described below.

From the narrow-strip and relaxed-tight SSVs, four orthogonal regions are defined based on which subset of the *Tight* ID cuts is passed:

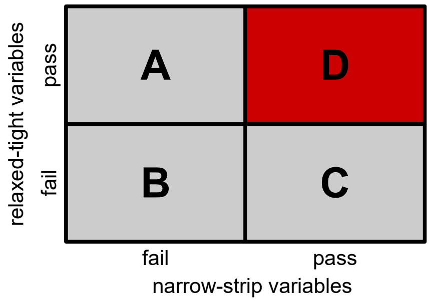

- Region D: passes both narrow-strip and relaxed-tight cuts, i.e. passes the full *Tight* ID WP.
- Regions A, B, and C are enriched in fake photons.

To determine the fake-photon track isolation efficiencies in the inclusive photon sample (regions A, B, C and D) and the *Tight*-passing sample (region D), the following approximations are made:

$$\hat{\varepsilon}_{\text{fake}} = \frac{\hat{N}^{\text{ABCD}}_{\text{fake}}}{N^{\text{ABCD}}_{\text{fake}}} \approx \frac{\hat{N}^{\text{ABC}}_{\text{fake}}}{N^{\text{ABC}}_{\text{fake}}} = \frac{R^{\text{ABC}}_{\gamma} \cdot \hat{\varepsilon}^{\text{ABC}}_{\gamma} - P_{\text{prompt}} \cdot R^{\text{ABC}}_{\text{prompt}} \cdot \hat{\varepsilon}^{\text{ABC}}_{\text{prompt}}}{R^{\text{ABC}}_{\gamma} - P_{\text{prompt}} \cdot R^{\text{ABC}}_{\text{prompt}}} \tag{6.5}$$

$$\hat{\varepsilon}^{\text{ID}}_{\text{fake}} = \frac{\hat{N}^{\text{D}}_{\text{fake}}}{N^{\text{D}}_{\text{fake}}} \approx \frac{\hat{N}^{\text{A}}_{\text{fake}}}{N^{\text{A}}_{\text{fake}}} = \frac{R^{\text{A}}_{\gamma} \cdot \hat{\varepsilon}^{\text{A}}_{\gamma} - P_{\text{prompt}} \cdot R^{\text{A}}_{\text{prompt}} \cdot \hat{\varepsilon}^{\text{A}}_{\text{prompt}}}{R^{\text{A}}_{\gamma} - P_{\text{prompt}} \cdot R^{\text{A}}_{\text{prompt}}} \tag{6.6}$$

Here, the superscripts A, B, C and D as well as combinations of those represent the corresponding regions. R^X_Y represents ratios of total or prompt photon candidates in the respective regions relative to the full sample. The ratios R^X_γ and the efficiencies $\hat{\varepsilon}^X_\gamma$ are measured in data, the ratios R^X_{prompt} and the efficiencies $\hat{\varepsilon}^X_{\text{prompt}}$ are obtained from simulation, using the γ+jet MC samples described in Section 4.5.1. The approximation in Equation (6.5) exploits that the majority of fake photons populate regions A, B, and C, such that contributions from region D can be neglected in the calculation of the fake-photon track isolation efficiency. The approximation in Equation (6.6) exploits the weak correlation between photon track isolation and narrow-strip SSVs, which arises because the narrow-strip variables describe the inner core of the photon candidate's calorimeter shower while isolation is instead sensitive to the outer activity. These assumptions are tested in simulation and a corresponding uncertainty is assigned, see Section 6.3.4.

An equation that is quadratic in $\hat{\varepsilon}_{\text{fake}}$ can be derived from Equations (6.5) and (6.6). Of the two mathematical solutions, the larger solution is unphysically large for fake photons, often even exceeding the corresponding $\hat{\varepsilon}_{\text{prompt}}$ values of prompt photons, and is therefore discarded. The smaller solution is used to calculate P_{prompt}. Subsequently, $\hat{\varepsilon}^{\text{ID}}_{\text{fake}}$, $P^{\text{ID}}_{\text{prompt}}$, $\varepsilon^{\text{ID}}_{\text{prompt}}$, and $\text{SF}^{\text{ID}}_{\text{prompt}}$ are calculated.

The full Run 2 dataset, described in Section 4.1, and the γ+jet and dijet MC samples, described in Section 4.5, are used for the measurement. Only events where

- at least one of the high level photon triggers described in Ref. [109] is passed,
- the *FixedCutLoose* photon isolation and *Loose* ID requirements described in Sections 5.2 and 5.3 are passed,
- and at least one photon candidate with transverse momentum $p_{\mathrm{T}}^{\gamma} \geq 25\,\mathrm{GeV}$ is present,

are used. Only the highest-p_{T}^{γ} photon candidate in an event is used for the calculations.

Corrections to account for this preselection, mismodeling in simulation, as well as the handling of special edge cases are described in Sections 6.3.1 through 6.3.3, uncertainties considered for the efficiency measurement in Section 6.3.4, and results are presented in Section 6.3.5.

6.3.1 Correction to account for preselection

The Matrix Method aims to measure the photon ID efficiency relative to the full sample of reconstructed prompt and isolated photons. However, the sample used is preselected using inclusive photon triggers and the *Loose* ID criteria, which both bias the sample toward well-identified photons. Consequently, the measured efficiency is not directly representative for the full reconstructed photon population.

To account for this, a correction factor f^{pre} is defined to extrapolate the efficiency from the preselected sample to the full one. This correction is derived from simulation and defined as the prompt-photon efficiency of the *Tight* ID WP relative to all prompt photons, divided by the corresponding *Tight*-to-*Loose*-plus-trigger ratio:

$$f^{\mathrm{pre}} = \left(\frac{N^{Tight}_{\mathrm{prompt,MC}}}{N_{\mathrm{prompt,MC}}} \right) \cdot \left(\frac{N^{\mathrm{trigger},Tight}_{\mathrm{prompt,MC}}}{N^{\mathrm{trigger},Loose}_{\mathrm{prompt,MC}}} \right)^{-1}, \tag{6.7}$$

where the superscripts indicate which requirements are passed. f^{pre} therefore rescales the efficiency measured in the preselected region to estimate the true efficiency with respect to the full sample without preselection. The factor is used to adapt Equation (6.1) to

$$\varepsilon^{\mathrm{ID}}_{\mathrm{prompt}} = \frac{P^{\mathrm{ID}}_{\mathrm{prompt}} \cdot N^{\mathrm{trigger},Tight}_{\gamma}}{P_{\mathrm{prompt}} \cdot N^{\mathrm{trigger},Loose}_{\gamma}} \cdot f^{\mathrm{pre}}, \tag{6.8}$$

with f^{pre} typically being close to unity at high energies, where the trigger and *Loose* ID requirements have almost 100% efficiency. At lower photon energies, f^{pre} becomes non-negligible, with typical values around 0.95 in the lowest E_{T}^{γ} bins. Separate correction factors are computed for converted and unconverted photons in bins of transverse energy and absolute pseudorapidity.

6.3.2 Exception handling for negative values of track isolation efficiencies

In some bins, the calculated track isolation efficiencies for fake photons, $\hat{\varepsilon}_{\mathrm{fake}}$ and $\hat{\varepsilon}_{\mathrm{fake}}^{\mathrm{ID}}$, can become negative. This can occur due to statistical fluctuations in the estimate of P_{prompt}, particularly in high-E_{T}^{γ} bins in which both $\hat{\varepsilon}_{\mathrm{fake}}$ and $\hat{\varepsilon}_{\mathrm{fake}}^{\mathrm{ID}}$ are expected to be close to zero and statistics are limited. As negative efficiencies are unphysical, an exception handling procedure is applied.

For each bin affected by a negative efficiency, a pseudo-experiment (PE) procedure is performed to recover a physically meaningful estimate. A total of 10,000 PEs are conducted separately for data and for the γ+jet MC sample. In each PE, a number of events N_{PD}^{i} is sampled using bootstrap resampling with replacement, where N_{PD}^{i} is drawn from a Poisson distribution centered on the nominal number of events in the corresponding bin. For each PE, all quantities required to evaluate $\hat{\varepsilon}_{\mathrm{fake}}$ and $\hat{\varepsilon}_{\mathrm{fake}}^{\mathrm{ID}}$, as defined in Equations (6.5) and (6.6), are computed.

In a second step, two multivariate normal distributions are constructed using the mean values and covariance matrices obtained from these data and MC PEs. New values for the input variables are sampled from the respective distributions. For each such set of variables, $\hat{\varepsilon}_{\mathrm{fake}}$ and $\hat{\varepsilon}_{\mathrm{fake}}^{\mathrm{ID}}$ are recalculated. If either of the two is negative, the sample is rejected. This process is repeated until 10,000 pairs of non-negative efficiencies are obtained.

The mean values of these filtered distributions are used in place of the original values for $\hat{\varepsilon}_{\mathrm{fake}}$ and $\hat{\varepsilon}_{\mathrm{fake}}^{\mathrm{ID}}$ in the subsequent Matrix Method calculations. Out of the 156 bins in the measurement, two bins required this exception handling procedure. These bins are listed in Table 6.2. An investigation of the variable values contributing to the negative efficiencies in these bins revealed no systematic behavior, supporting the assumption that the negative efficiencies arise purely from statistical fluctuations.

Table 6.2: Matrix Method bins (photon conversion type, absolute pseudorapidity $|\eta_{\mathrm{cl}}^{\gamma}|$ and transverse energy E_{T}^{γ}) where at least one of the computed non-prompt photon track isolation efficiencies is negative and exception handling is applied.

conversion type	$\lvert\eta_{\mathrm{cl}}^{\gamma}\rvert$ bin	E_{T}^{γ} bin [GeV]
unconverted	[1.81, 2.01)	[250, 350)
unconverted	[1.81, 2.01)	[350, 1500)

6.3.3 Correction to account for mismodeling of prompt-photon leakage into non-*Tight*-identification regions

The estimation of $\hat{\varepsilon}_{\text{fake}}$ and $\hat{\varepsilon}^{\text{ID}}_{\text{fake}}$ via Equations (6.5) and (6.6) relies on simulation to subtract the contribution from prompt photons in the non-*Tight*-ID regions. However, the fraction of prompt photons passing or failing the individual photon ID SSV requirements, and consequently the leakage of prompt photons into these non-ID regions, may be mismodeled in simulation.

To correct for this potential mismodeling, an iterative procedure is applied to the prompt-photon leakage ratios $R^{\text{ABC}}_{\text{prompt}}$ and $R^{\text{A}}_{\text{prompt}}$. First, a scale factor for prompt photons failing the *Tight* ID WP is derived from the scale factor for *Tight* ID efficiency, $\text{SF}^{\text{ID}}_{\text{prompt}}$ (see Equation (6.2)):

$$\text{SF}^{\text{nonID}}_{\text{prompt}} = \frac{1 - \text{SF}^{\text{ID}}_{\text{prompt}} \cdot \varepsilon^{\text{ID}}_{\text{prompt,MC}}}{1 - \varepsilon^{\text{ID}}_{\text{prompt,MC}}}, \tag{6.9}$$

where $\varepsilon^{\text{ID}}_{\text{prompt,MC}}$ is the *Tight* ID efficiency for prompt photons in simulation.

The correction proceeds via the following iterative steps, starting from an initial value of $\text{SF}^{\text{nonID}}_{\text{prompt},0} = 1$:

$$1: \quad R^{\text{BC}}_{\text{prompt},i} = R^{\text{ABC}}_{\text{prompt},i} - R^{\text{A}}_{\text{prompt},i} \tag{6.10}$$
$$2: \quad R^{\text{ABC}}_{\text{prompt},i+1} = \text{SF}^{\text{nonID}}_{\text{prompt,i}} \cdot R^{\text{ABC}}_{\text{prompt},i} \tag{6.11}$$
$$3: \quad R^{\text{A}}_{\text{prompt},i+1} = R^{\text{ABC}}_{\text{prompt},i+1} - R^{\text{BC}}_{\text{prompt},i} \tag{6.12}$$
$$4: \quad \text{Compute } \varepsilon^{\text{ID}}_{\text{prompt},i+1},\ \text{SF}^{\text{ID}}_{\text{prompt},i+1},\ \text{SF}^{\text{nonID}}_{\text{prompt},i+1} \tag{6.13}$$

This procedure is repeated until $\varepsilon^{\text{ID}}_{\text{prompt},i}$ converges. Fifteen iterations have been found to be sufficient to achieve convergence in all bins. The initial value is taken as the nominal result, while the difference to the converged value is used to assess the associated uncertainty.

6.3.4 Uncertainties

Several sources of uncertainty are considered and are described in the following. The total uncertainty is computed as the sum in quadrature of the individual components, assuming that the different sources are uncorrelated. Breakdowns of the individual uncertainties across the different bins for the presented measurement are shown in Figure 6.4 and in Appendix B.

Statistical
Two separate uncertainties are derived. One arising from the limited size of the dataset, referred to as statistical uncertainty, and one from the limited size of the γ+jet MC sample, referred to as MC statistical uncertainty. Both are estimated using PEs conducted in the same way as described in Section 6.3.2. For each PE, the photon *Tight* ID efficiency $\varepsilon^{\mathrm{ID}}_{\mathrm{prompt}}$ is calculated. A number of 200 PEs for both data and simulation was found to be sufficient to obtain Gaussian-shaped distributions of $\varepsilon^{\mathrm{ID}}_{\mathrm{prompt}}$ that remain stable when increasing the number of PEs. The standard deviations of these distributions are taken as the corresponding statistical uncertainties. Examples of the resulting distributions obtained for the presented measurement are shown in Figure 6.1.

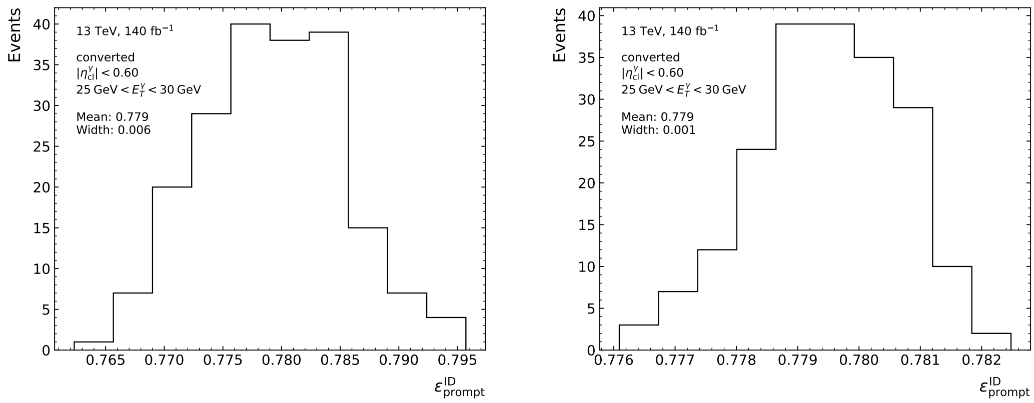

Figure 6.1: Distributions of the photon identification efficiencies from the pseudo-experiments used to estimate the uncertainties arising from limited statistics in data (left) and Monte Carlo (right), shown exemplary for converted photons with $|\eta^{\gamma}_{\mathrm{cl}}| < 0.6$ and $25\,\mathrm{GeV} < E^{\gamma}_{\mathrm{T}} < 30\,\mathrm{GeV}$.

Track isolation requirement
To assess the impact of the track isolation cone size, the nominal cone radius of $R = 0.4$ is reduced to 0.3. The absolute difference in the resulting photon *Tight* ID efficiency is taken as the associated uncertainty.

Correction for preselection
The correction factor f^{pre} is derived from the γ+jet MC sample. Sources of uncertainty include the mismodeling of the trigger efficiency and the *Loose* photon ID efficiency in this sample, as well as limited statistics. However, the trigger efficiencies in the relevant kinematic phase space are close to 100% in both data and simulation and are therefore neglected. The impact of the possible mismodeling of the *Loose* ID efficiency is assessed based on the corresponding scale factors $\mathrm{SF}^{Loose}_{\mathrm{prompt}}$ measured

with the Radiative Z Method described in Section 6.1. These SFs show sizeable fluctuations and only cover the range up to $E_{\mathrm{T}}^{\gamma} \leq 100\,\mathrm{GeV}$. To extrapolate beyond this region, a fit of the form

$$\mathrm{SF}_{\mathrm{prompt}}^{Loose}(E_{\mathrm{T}}^{\gamma}) = \frac{a}{\log(E_{\mathrm{T}}^{\gamma})} + 1 \tag{6.14}$$

is performed, separately for converted and unconverted photons in each $|\eta_{\mathrm{cl}}^{\gamma}|$ bin. This functional form is chosen because it has only one free parameter, reducing the risk of overfitting to statistical fluctuations, it naturally approaches unity at high E_{T}^{γ} where the *Loose* ID efficiency is expected to be close to 100%, and it provides a stable extrapolation beyond the measured E_{T}^{γ} range.

The largest deviation of the fit, including its 1σ confidence interval, from the nominal value of 1 is taken as the uncertainty due to *Loose* ID mismodeling. This is then combined in quadrature with the statistical uncertainty from the γ+jet MC sample. The resulting total uncertainty is applied to f^{pre}, and the photon *Tight* ID efficiency is recalculated for the up and down variations. The maximum deviation from the nominal result is assigned as the systematic uncertainty on the *Tight* ID efficiency. Examples of $\mathrm{SF}_{\mathrm{prompt}}^{Loose}$ values, the corresponding fits and the resulting correction factors used for this measurement are shown in Figure 6.2.

Correction for prompt-photon leakage
To assess the impact of potential mismodeling of prompt-photon leakage into the non-*Tight*-ID regions, the absolute difference between the initial photon ID efficiency and the efficiency after the final iteration of the correction procedure is taken as the associated uncertainty. Examples of the evolution of $\varepsilon_{\mathrm{prompt},i}^{\mathrm{ID}}$ during the iterative correction procedure are shown in Figure 6.3.

Fudge factors
To account for the uncertainties associated with the fudge factors, each corrected SSV is varied by adding the corresponding fudge factor uncertainty. Since some SSVs are strongly correlated, the variations are applied in four sets: (R_{had}) for the hadronic leakage, (R_{ϕ}) for the shower width in ϕ direction, ($R_{\eta}, \omega_{\eta 2}$) for the shower width in η direction, and ($\omega_{s,3}, \omega_{s,\mathrm{tot}}, F_{\mathrm{side}}$) for the lateral shower width in the strip layer. These sets ensure that strongly correlated variables describing similar aspects of the calorimeter shower are varied together. For each set, the photon ID efficiency is recalculated, and the difference from the nominal value is taken as the associated uncertainty. The total fudge-factor uncertainty is obtained as the quadratic sum of the four contributions.

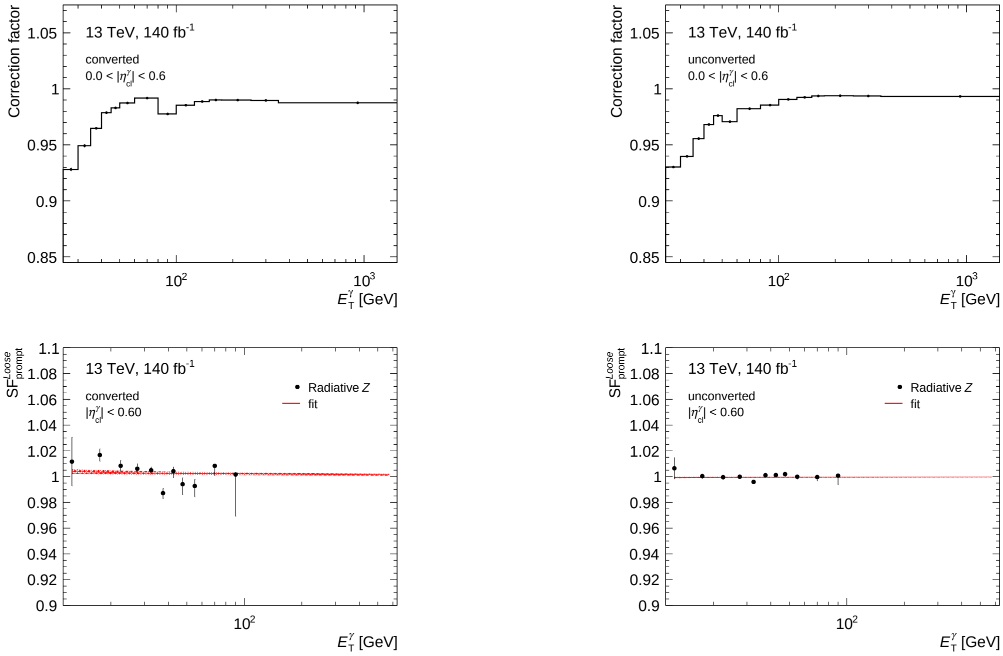

Figure 6.2: Upper row: nominal correction factors used to account for the Matrix Method preselection, shown for converted (left) and unconverted (right) photons with exemplary pseudorapidity $|\eta_{\mathrm{cl}}^{\gamma}| < 0.6$. Statistical uncertainties are included but too small to be visible. Lower row: corresponding scale factors with statistical uncertainties for the *Loose* photon ID efficiency obtained via the Radiative Z Method, together with the fit function from Equation (6.14) and its 1σ confidence band.

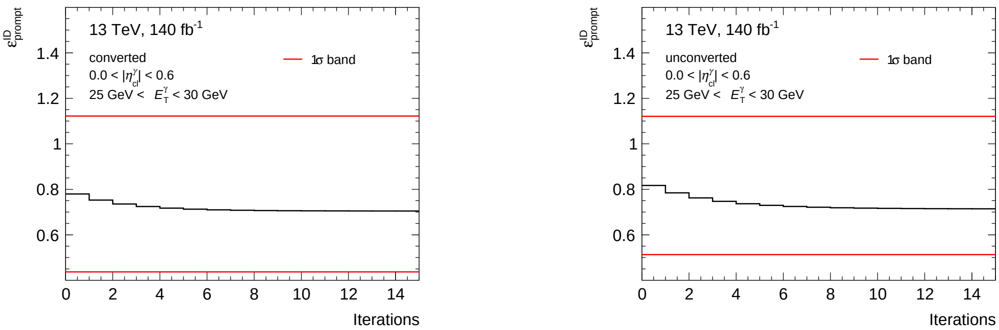

Figure 6.3: Iterative evolution of $\varepsilon_{\mathrm{prompt}}^{\mathrm{ID}}$, shown for converted (left) and unconverted (right) photons with exemplary pseudorapidity $|\eta_{\mathrm{cl}}^{\gamma}| < 0.6$ and transverse energy $25\,\mathrm{GeV} < E_{\mathrm{T}}^{\gamma} < 30\,\mathrm{GeV}$. Total uncertainties from other sources are indicated by the red band.

Non-closure

The assumption that the narrow-strip variables and the photon track isolation requirement are only weakly correlated, which is used in Equation (6.6), is tested using the fake-photon dijet MC sample, described in Section 4.5.2. Due to the limited MC statistics, the study is performed inclusively across all photon energies.

In the dijet sample, the following quantities are computed, which without any correlation would both be expected to be close to zero:

$$\Delta\hat{\varepsilon}_{\text{fake}} = \frac{|\hat{\varepsilon}^{\text{ABCD}}_{\text{fake}} - \hat{\varepsilon}^{\text{ABC}}_{\text{fake}}|}{\hat{\varepsilon}^{\text{ABCD}}_{\text{fake}}} \tag{6.15}$$

$$\Delta\hat{\varepsilon}^{\text{ID}}_{\text{fake}} = \frac{|\hat{\varepsilon}^{\text{D}}_{\text{fake}} - \hat{\varepsilon}^{\text{A}}_{\text{fake}}|}{\hat{\varepsilon}^{\text{D}}_{\text{fake}}}. \tag{6.16}$$

To assess the impact of potential correlation (non-closure), the track isolation efficiencies of fake photons $\hat{\varepsilon}_{\text{fake}}$ and $\hat{\varepsilon}^{\text{ID}}_{\text{fake}}$ are independently varied up and down, resulting in four variations. The photon *Tight* ID efficiency is recomputed for each. The absolute differences from the nominal result for the two variations that lead to a higher ID efficiency are combined in quadrature, and the same is done for the two that decrease it. The larger of these two combinations is assigned as the non-closure uncertainty on the photon *Tight* ID efficiency. The obtained values for $\Delta\hat{\varepsilon}_{\text{fake}}$ and $\Delta\hat{\varepsilon}^{\text{ID}}_{\text{fake}}$ are shown in Table 6.3.

Table 6.3: Values of $\Delta\hat{\varepsilon}_{\text{fake}}$ and $\Delta\hat{\varepsilon}^{\text{ID}}_{\text{fake}}$ with statistical uncertainties, obtained from the dijet Monte Carlo sample, used to estimate the Matrix Method non-closure uncertainty.

$\lvert\eta^{\gamma}_{\text{cl}}\rvert$ bin	converted		unconverted	
	$\Delta\hat{\varepsilon}_{\text{fake}}$ [%]	$\Delta\hat{\varepsilon}^{\text{ID}}_{\text{fake}}$ [%]	$\Delta\hat{\varepsilon}_{\text{fake}}$ [%]	$\Delta\hat{\varepsilon}^{\text{ID}}_{\text{fake}}$ [%]
[0.0, 0.6)	10.7 ± 1.1	5.9 ± 0.9	11.2 ± 0.6	6.4 ± 0.6
[0.6, 0.8)	9.3 ± 2.2	4.6 ± 1.7	10.0 ± 1.1	5.7 ± 0.9
[0.8, 1.37)	7.0 ± 1.0	5.2 ± 0.8	7.5 ± 0.7	5.0 ± 0.7
[1.52, 1.81)	7.2 ± 1.1	4.6 ± 0.9	7.5 ± 1.3	5.1 ± 1.2
[1.81, 2.01)	8.0 ± 1.5	4.5 ± 1.3	8.3 ± 1.5	5.2 ± 1.4
[2.01, 2.37)	7.8 ± 1.2	5.6 ± 1.1	7.2 ± 1.1	4.7 ± 1.0

6.3.5 Results: photon identification efficiencies

The measured photon ID efficiencies $\varepsilon^{\mathrm{ID}}_{\mathrm{prompt}}$ and scale factors $\mathrm{SF}^{\mathrm{ID}}_{\mathrm{prompt}}$, together with a breakdown of the associated uncertainties, are shown for converted and unconverted photons with $|\eta^{\gamma}_{\mathrm{cl}}| < 0.6$ in Figure 6.4. Results for all other $|\eta^{\gamma}_{\mathrm{cl}}|$ bins are shown in Appendix B and are also considered in the following discussion.

At low E^{γ}_{T}, the photon ID efficiency measured in data is smaller than in simulation. This leads to scale factors starting around 0.90 to 0.95 in the lowest bins, and gradually approaching unity for $E^{\gamma}_{\mathrm{T}} > 100\,\mathrm{GeV}$. This behavior is expected. At low E^{γ}_{T}, photon showers in the electromagnetic calorimeter are broader and more affected by fluctuations. Simulation slightly idealizes the shower shapes, leading to an overestimation of the ID efficiency. At higher E^{γ}_{T}, the showers become narrower, the SSVs are better modeled, and the data and simulation efficiencies converge.

In the lowest E^{γ}_{T} bin (25 GeV to 30 GeV), the ID efficiencies are around 80% for most $|\eta^{\gamma}_{\mathrm{cl}}|$ bins. For medium E^{γ}_{T} (around 150 GeV to 250 GeV), efficiencies increase from about 96% up to 98% for converted photons and from about 92% up to 96% for unconverted photons, depending on the $|\eta^{\gamma}_{\mathrm{cl}}|$ bin. At low E^{γ}_{T}, unconverted photons have slightly higher ID efficiencies than converted photons because of their narrower calorimeter showers. At medium to high E^{γ}_{T}, converted and unconverted photons produce showers of more similar width, and converted photons exhibit slightly higher efficiencies.

The non-closure uncertainty is dominant at low E^{γ}_{T}. As shown in Table 6.3, the deviations $\Delta\hat{\varepsilon}_{\mathrm{fake}}$ and $\Delta\hat{\varepsilon}^{\mathrm{ID}}_{\mathrm{fake}}$ differ from zero by several times their statistical uncertainty, indicating a non-negligible correlation between the track isolation criterion and the narrow-strip SSVs. The observed non-closure is not specific to any particular narrow-strip SSV. Instead, it is observed consistently across all narrow-strip SSVs, pointing to a more global correlation between the track isolation requirement and the calorimeter-based photon ID.

As discussed in Section 5.8, the reconstruction software has undergone considerable changes since earlier Matrix Method measurements, in particular with respect to track reconstruction. Given the number and scope of these changes, it is difficult to attribute the observed increase in correlation to a single modification. Nevertheless, it is plausible that the improved rejection of fake tracks and the increased robustness against pile-up tracks and energy contributions enhance the coupling between track-based isolation criteria and the calorimeter-based narrow-strip SSVs.

The impact of this correlation on the non-closure uncertainty is particularly pronounced at low E^{γ}_{T}. In this region, the separation power of the track isolation criterion between prompt and fake photons is reduced. The prompt-photon track isolation efficiency remains relatively constant at around 70% across the full E_{T}^{γ} range. In contrast, while the fake-photon efficiency approaches zero at high E_{T}^{γ}, it reaches values of up to about 50% in the lowest E_{T}^{γ} bins, resulting in a comparatively small difference between the prompt- and fake-photon efficiencies.

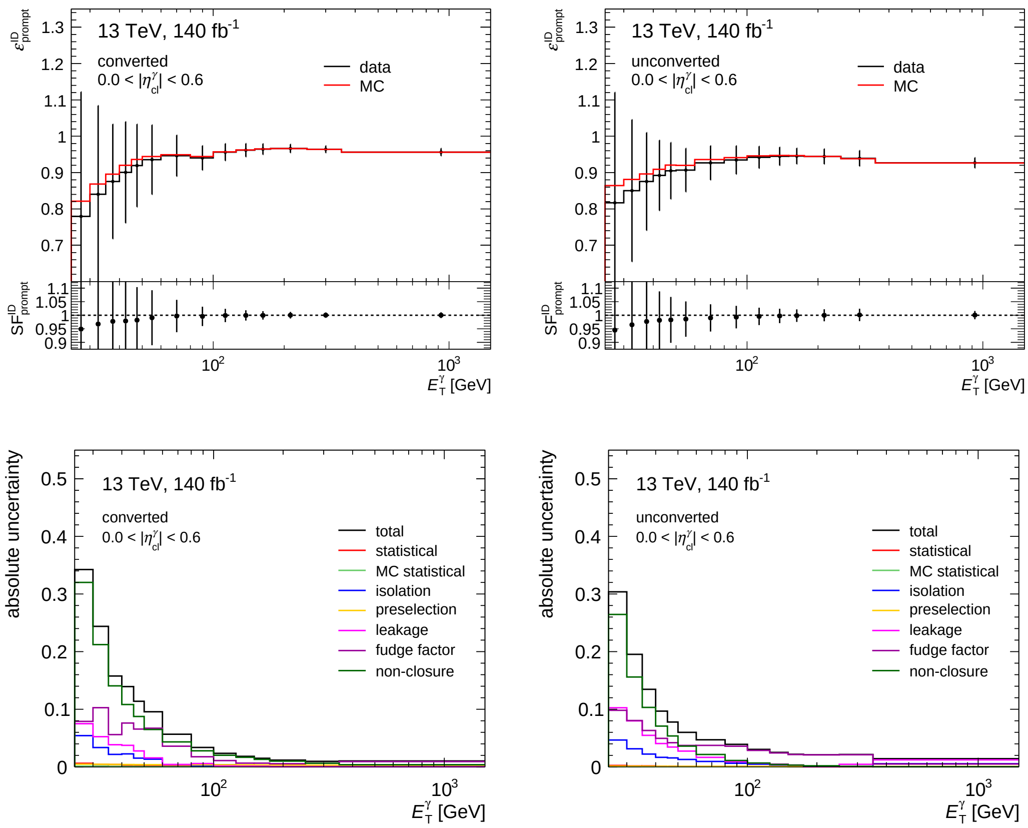

Figure 6.4: Prompt photon identification efficiencies with total uncertainties in data and simulation and resulting scale factors for $|\eta_{\mathrm{cl}}^{\gamma}| < 0.6$ (upper row) for converted photons (left) and unconverted photons (right). Corresponding breakdowns of individual uncertainties in the lower row.

As a consequence, the expressions in Equations (6.3) and (6.4) become increasingly sensitive to upward variations of $\hat{\varepsilon}_{\mathrm{fake}}$ and $\hat{\varepsilon}_{\mathrm{fake}}^{\mathrm{ID}}$. In the low-$E_{\mathrm{T}}^{\gamma}$ regions, such variations can bring the denominator of the equations close to zero, leading to numerical instabilities. The resulting non-closure uncertainty should therefore be regarded as highly conservative in this phase-space region.

Another large contribution is the fudge factor uncertainty. It becomes one of the dominant uncertainties for unconverted photons at high E_{T}^{γ}. The magnitude of this uncertainty should be regarded as conservative, since the fudge factors were still undergoing significant developments at the time of this measurement. As a result, the variations likely overestimate the true impact of the fudge factor uncertainties.

Track isolation uncertainties also play a significant role at low E_{T}^{γ}. The uncertainty associated with the correction for prompt-photon leakage is of comparable size and, for unconverted photons, is dominant in some high-E_{T}^{γ} bins.

The results obtained with the Radiative Z Method, the Electron Extrapolation Method, and the Matrix Method are combined using the BLUE method [110]. An example bin of the combination is shown in Figure 6.5. At low E_{T}^{γ}, the Matrix Method carries little statistical weight in the combination due to its large uncertainty and is therefore only included for $E_{\mathrm{T}}^{\gamma} > 50\,\mathrm{GeV}$, while the other two methods provide sufficient coverage at lower energies. In the regions where the different methods overlap, they agree well within their respective uncertainties, resulting in a consistent and comprehensive measurement of the photon ID efficiency across a large E_{T}^{γ} spectrum. The good agreement in the overlap regions suggests that the underlying assumptions of the Matrix Method remain valid despite the non-negligible correlations observed between the track isolation criterion and the narrow-strip variables.

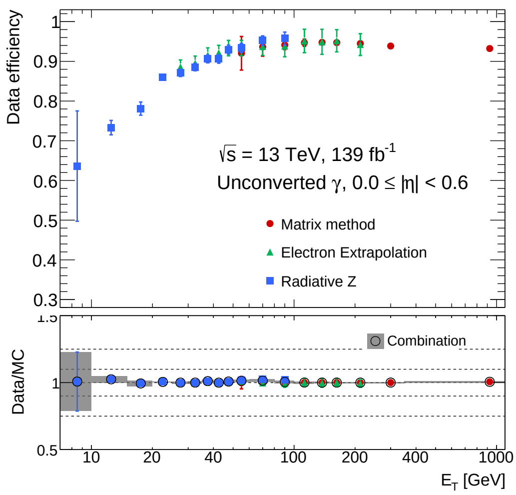

Figure 6.5: Photon identification efficiency measured with the Matrix Method, Radiative Z Method and Electron Extrapolation Method as a function of the transverse photon energy, shown here for unconverted photons with $|\eta| < 0.6$. The lower panel displays the corresponding scale factors, including the combined weighted average with its total uncertainty. Figure courtesy of Francisco Alonso.

7 Analysis Strategy

The previous chapters have introduced the theoretical foundations of the SM (Chapter 2) and the single top-quark production mechanisms (Section 2.4), as well as the experimental setup at the LHC and the ATLAS detector (Chapter 3). The following chapter provides an overview of the strategy for the measurement of the differential cross-section of the t-channel single top-quark process in association with a photon ($tq\gamma$) in the leptonic decay channel of the top quark. The dataset and the MC samples used for the measurement have been described in Section 4.1 and Section 4.4.

7.1 Event Selection

The measurement is performed in the semileptonic decay channel of the top quark. The expected detector signature is characterized by:

- one isolated high-p_{T} photon,
- a forward jet associated with the spectator quark (typically a valence quark from the incoming proton, carrying significant longitudinal momentum),
- at least one b-jet (from the top-quark decay),
- a charged lepton (electron or muon),
- missing transverse momentum from the undetected neutrino.

Using the object definitions described in Chapter 5, an event selection is constructed to target the characteristic topology of the $tq\gamma$ process and to define a signal region enriched in signal events. To suppress background contributions from Z+jets events, in which the Z boson decays into an electron pair and one electron is misidentified as a photon, events with an invariant mass of the electron-photon system $m_{e\gamma}$ within a window around the Z boson mass, $81\,\mathrm{GeV} < m_{e\gamma} < 101\,\mathrm{GeV}$, are rejected.

The signal region requires exactly one b-tagged jet at the 70% efficiency working point (WP) and vetoes additional b-tagged jets at the looser 85% WP, reflecting the presence of a single b-jet from the top-quark decay in the $tq\gamma$ process and suppressing backgrounds containing two top quarks. Two orthogonal control regions are defined to constrain the dominant prompt-photon backgrounds, $t\bar{t}\gamma$ and $W\gamma$+jets. The b-tag multiplicity requirements are modified to enrich the respective backgrounds while maintaining a topology close to that of the signal region. The exact definitions of all analysis regions are summarized in Table 7.1.

Table 7.1: Definitions of the analysis regions (see Chapter 5 for object definitions).

Requirement	Signal region	$t\bar{t}\gamma$ control region	$W\gamma$+jets control region
Photons	exactly 1 ($p_{\mathrm{T}}^{\gamma} \geq 20\,\mathrm{GeV}$)		
Leptons	exactly 1 ($p_{\mathrm{T}}^{\ell} \geq 28\,\mathrm{GeV}$)		
	no additional lepton with $p_{\mathrm{T}}^{\ell} \geq 10\,\mathrm{GeV}$		
$E_{\mathrm{T}}^{\mathrm{miss}}$	$\geq 30\,\mathrm{GeV}$		
$m_{e\gamma}$	not in $[81, 101]$ GeV		
Jets	≥ 1 ($p_{\mathrm{T}}^{\mathrm{jet}} \geq 25\,\mathrm{GeV}$)	≥ 2 ($p_{\mathrm{T}}^{\mathrm{jet}} \geq 25\,\mathrm{GeV}$)	≥ 1 ($p_{\mathrm{T}}^{\mathrm{jet}} \geq 25\,\mathrm{GeV}$)
b-tags	$= 1$ (70% WP)	$= 1$ (70% WP)	$= 0$ (70% WP)
	$= 1$ (85% WP)	≥ 2 (85% WP)	≥ 1 (85% WP)

7.2 Event categorization

Since the event topology features a photon, processes in which an electron or a hadron is misidentified as a photon form major background contributions. In simulation, events are categorized according to the truth particle[1] associated with the reconstructed photon and referred to as either:

- $e \to \gamma$ *fake*:
  - the truth particle is an electron, or
  - the truth particle is a photon but a truth electron is present within $\Delta R = 0.05$, in which case the photon is likely radiated from the electron.
- $h \to \gamma$ *fake*:
  - the truth particle is a hadron, or
  - the truth particle originates from a hadron.
- otherwise: *prompt*.

The contributions from events with $e \to \gamma$ or $h \to \gamma$ fake photons are typically not modeled with sufficient accuracy in simulation. To correct for that, data-driven methods are used to determine scale factors for both of the fake-photon categories,

[1]Here, "truth" refers to the particle-level information from the MC simulation.

described in Sections 8.1 and 8.2. The obtained scale factors are applied to MC events belonging to the respective fake-photon category.

7.3 Signal identification and beyond

After establishing the event selection and background estimation, a Neural Network (NN) is trained to discriminate between signal and background events (Chapter 9). A cut on the output of this classifier is used to subdivide the signal region into a region containing events that fail the cut (the *NN fail* region) and a region containing events that pass the cut (the *NN pass* region), resulting in a greatly increased signal purity for the latter. A schematic overview of the analysis strategy is shown in Figure 7.1.

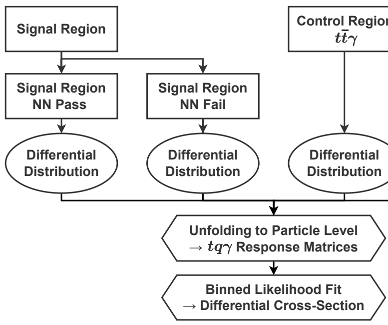

Figure 7.1: Schematic overview of the analysis strategy. Events are categorized into two signal regions based on the Neural Network (NN) output and into control regions enriched in $t\bar{t}\gamma$ and $W\gamma$ events. Reconstruction-level distributions in all regions are used as input to a simultaneous binned likelihood fit. The signal contribution at particle level is connected to the reconstruction level via response matrices obtained from simulation. The fit extracts the differential signal normalisation factors and the corresponding cross-section for the $tq\gamma$ process at particle level.

Differential cross-section measurements are performed for different reconstruction-level observables, each employing a separate binned likelihood fit, as described in Section 2.4.2, performed simultaneously across all four analysis regions. The signal contributions are modeled at particle level and connected to reconstruction level via response matrices $R_{ib,r}$, derived from simulation for each region r. The matrix elements define the probabilities for events generated in a particle-level bin i to be reconstructed in bin b, including the detector acceptance and selection efficiency. A separate normalization parameter $\mu_i^{tq\gamma}$ is introduced for each particle-level bin. For observables that are not defined at reconstruction level in certain regions, such as observables related to the top quark in the $W\gamma$ control region, a response matrix is constructed that instead connects the particle-level distribution to a common alternative observable, the reconstruction-level p_{T}^{γ} distribution. While such response matrices exhibit significant off-diagonal contributions, this choice allows a consistent treatment of the signal contribution across all regions. It also retains sensitivity to the composition of background processes such as $t\bar{t}\gamma$ and $W\gamma$, therefore improving the constraints on the corresponding normalization parameters in the fit. The fit determines the values of all fit parameters that maximize the likelihood[2], taking into account the folding (i.e. detector response) of the particle-level signal contributions via the response matrix. The fit is performed using the TRExFitter framework [111], which employs the Minuit package [112] to determine the parameter values that best describe the data.

The likelihood function is constructed as a product of Poisson probabilities and constraint terms (Pois) and Gaussian constraints ($\mathcal{N}$) over all particle-level bins i and reconstruction-level bins b in all regions r,

$$\begin{aligned}\mathcal{L}(\boldsymbol{n}^{\mathrm{data}} \mid \boldsymbol{\mu}, \boldsymbol{\theta}, \boldsymbol{\gamma}) = &\prod_{b,r} \mathrm{Pois}\big(n_{b,r}^{\mathrm{data}} \mid n_{b,r}^{\mathrm{pred}}(\boldsymbol{\mu}, \boldsymbol{\theta}, \boldsymbol{\gamma})\big)\\ &\cdot \prod_{k} \mathcal{N}(\theta_k \mid 0, 1)\\ &\cdot \prod_{i,b,r} \mathrm{Pois}\big(\tau_{ib,r}^{tq\gamma} \mid \gamma_{ib,r}^{tq\gamma} \cdot \tau_{ib,r}^{tq\gamma}\big) \cdot \prod_{b,r} \mathrm{Pois}\big(\tau_{b,r}^{\mathrm{bkg}} \mid \gamma_{b,r}^{\mathrm{bkg}} \cdot \tau_{b,r}^{\mathrm{bkg}}\big), \qquad (7.1)\end{aligned}$$

where $\boldsymbol{\mu}$, $\boldsymbol{\theta}$, and $\boldsymbol{\gamma}$ denote the sets of all corresponding parameters, $\boldsymbol{n}^{\mathrm{data}}$ denotes all observed numbers of events $n_{b,r}^{\mathrm{data}}$, and $n_{b,r}^{\mathrm{pred}}$ denotes the predicted yield in bin b of region r. The predicted yields are given by

$$\begin{aligned}n_{b,r}^{\mathrm{pred}}(\boldsymbol{\mu}, \boldsymbol{\theta}, \boldsymbol{\gamma}) = &\sum_{i} \gamma_{ib,r}^{tq\gamma}\, R_{ib,r}(\boldsymbol{\theta})\, \mu_i^{tq\gamma}\, n_i^{tq\gamma}\\ &+ \gamma_{b,r}^{\mathrm{bkg}} \left[\mu^{t\bar{t}\gamma}\, n_{b,r}^{t\bar{t}\gamma}(\boldsymbol{\theta}) + \mu^{W\gamma}\, n_{b,r}^{W\gamma}(\boldsymbol{\theta}) + n_{b,r}^{\mathrm{other}}(\boldsymbol{\theta})\right], \qquad (7.2)\end{aligned}$$

where $\mu_i^{tq\gamma}$ are normalization parameters corresponding to the particle-level signal contribution in bin i, and $n_i^{tq\gamma}$ are the particle-level signal yields in simulation, which are mapped to reconstruction-level yields via the response matrix $R_{ib,r}(\boldsymbol{\theta})$. The dominant prompt-photon background contributions from $t\bar{t}\gamma$ and $W\gamma$ production $n_{b,r}^{t\bar{t}\gamma}(\boldsymbol{\theta})$ and $n_{b,r}^{W\gamma}(\boldsymbol{\theta})$ are modeled at reconstruction level with normalization parameters $\mu^{t\bar{t}\gamma}$ and $\mu^{W\gamma}$, respectively, while all other background contributions

[2] In practice, the fit is performed by minimizing the negative logarithm of the likelihood, which improves numerical stability and is equivalent to maximizing the likelihood.

are included in $n_{b,r}^{\text{other}}(\boldsymbol{\theta})$. The normalization parameters $\boldsymbol{\mu}$ are unconstrained in the likelihood, i.e. no constraint terms are applied in Equation (7.1).

Systematic uncertainties σ_k^{syst}, arising from sources such as modeling, analysis-specific effects, and calibration measurements, are incorporated via nuisance parameters θ_k, which modify the predicted yields. For each source of uncertainty k, alternative distributions corresponding to variations of $\pm\sigma_k^{\text{syst}}$ are used as additional inputs to the fit. Interpolation between the nominal and varied distributions is used to parametrize the yields as a function of θ_k, where $\theta_k = 0$ corresponds to the nominal prediction and $\theta_k = \pm 1$ to the $\pm\sigma_k^{\text{syst}}$ variations. These variations can affect both the normalization and the shape of the distributions. The nuisance parameters are constrained by Gaussian terms $\mathcal{N}(\theta_k \mid 0, 1)$, which represent the uncertainties as likelihood contributions during the fit.

The $\boldsymbol{\gamma}$ parameters allow the predicted yields in each bin to fluctuate according to the statistical uncertainties of the simulated samples. Introducing separate parameters for each individual background process would lead to an impractically large number of parameters. Therefore, inclusive parameters $\gamma_{b,r}^{\text{bkg}}$ are used, which scale the total background contribution per bin b and region r. These parameters are constrained according to Equation (7.1) by Poisson terms with fixed values $\tau_{b,r}^{\text{bkg}} = (n_{b,r}^{\text{MC}}/\sigma_{b,r}^{\text{stat}})^2$, derived from the simulated yields $n_{b,r}^{\text{MC}}$ and the corresponding statistical uncertainties $\sigma_{b,r}^{\text{stat}}$. Smaller statistical uncertainties correspond to larger values of $\tau_{b,r}^{\text{bkg}}$ and therefore to stronger constraints on $\gamma_{b,r}^{\text{bkg}}$. For the $tq\gamma$ signal, separate parameters $\gamma_{ib,r}^{tq\gamma}$ are introduced for each response between particle-level bin i and reconstruction-level bin b. These $\gamma_{ib,r}^{tq\gamma}$ are constrained by corresponding values $\tau_{ib,r}^{tq\gamma}$, which are derived from the signal yields and statistical uncertainties associated with each response. Since, for a given particle-level bin, each reconstruction-level bin receives only a fraction of the events, the statistical uncertainty is dominated by the reconstruction-level contribution, and the particle-level statistical uncertainty is neglected.

The subdivision of the signal region into the *NN fail* and *NN pass* regions enhances the sensitivity of the fit to the signal contribution. In particular, the *NN pass* region, with its higher signal purity, is expected to provide strong constraints on the signal normalization parameters. The main result of the fit is a set of signal normalization parameters at particle level. The measured differential $tq\gamma$ cross-section $\sigma_i^{tq\gamma,\text{meas}}$ in bin i is obtained by scaling the corresponding particle-level cross-section in simulation, $\sigma_i^{tq\gamma,\text{MC}}$, with the fitted normalization parameter $\mu_i^{tq\gamma,\text{fit}}$, according to

$$\sigma_i^{tq\gamma,\text{meas}} = \mu_i^{tq\gamma,\text{fit}} \cdot \sigma_i^{tq\gamma,\text{MC}}. \tag{7.3}$$

8 Data-driven estimation of backgrounds with misidentified or non-prompt photons

Backgrounds involving misidentified or non-prompt photons are typically difficult to model accurately using Monte Carlo (MC) simulation. In this analysis, background contributions arising from electrons misidentified as photons ($e \to \gamma$ fakes) and hadronic objects misidentified as photons ($h \to \gamma$ fakes) are therefore estimated using dedicated data-driven methods. These methods are tailored to the specific features of the analysis and are described in the following sections.

8.1 Estimation of background contribution from electrons misidentified as photons

Electrons and photons are both reconstructed from clusters of energy deposits in the electromagnetic calorimeter (see Section 5.3). Because of their similar properties, electrons may falsely be reconstructed as photons. This can happen for several reasons. The electron track may fail to be reconstructed, it may be misclassified as originating from a photon conversion, or the electron may radiate a photon via bremsstrahlung that is then misidentified as a prompt photon. To correct for possible differences between data and MC, scale factors $\mathrm{SF}^{e\to\gamma}$ are derived and applied to all MC events that are, as described in Section 7.2, classified as $e \to \gamma$ fakes.

8.1.1 Methodology

The probability for an electron to be reconstructed as a photon, denoted as $P^{e\to\gamma}$, is estimated in Z+jets events as

$$P^{e\to\gamma} = \frac{N(Z \to e\gamma)}{2 \cdot N(Z \to ee)}, \tag{8.1}$$

where $N(X)$ is the number of events reconstructed in the corresponding final-state configuration. The factor of two in the denominator accounts for the possibility that either electron in the $Z \to ee$ decay may be reconstructed as a photon. A data-to-MC scale factor is then defined according to Equation (8.1) as

$$\mathrm{SF}^{e\to\gamma} = \frac{P^{e\to\gamma}_{\mathrm{data}}}{P^{e\to\gamma}_{\mathrm{MC}}} = \frac{N_{\mathrm{data}}(Z \to e\gamma)}{N_{\mathrm{MC}}(Z \to e\gamma)} \cdot \frac{N_{\mathrm{MC}}(Z \to ee)}{N_{\mathrm{data}}(Z \to ee)}. \tag{8.2}$$

For convenience, the two factors in Equation (8.2) are defined as

$$\mu^{Ze\gamma} = \frac{N_{\mathrm{data}}(Z \to e\gamma)}{N_{\mathrm{MC}}(Z \to e\gamma)}, \tag{8.3}$$

$$\mu^{Zee} = \frac{N_{\mathrm{data}}(Z \to ee)}{N_{\mathrm{MC}}(Z \to ee)}. \tag{8.4}$$

Two control regions (CRs) and one validation region (VR) with the nominal object definitions described in Chapter 5 are used:

- $Z \to e\gamma$ CR: one electron, one photon, zero b-tags (77% WP),
- $Z \to ee$ CR: two electrons, zero photons, zero b-tags (77% WP),
- $Z \to e\gamma$ VR: one electron, one photon, at least one b-tag (77% WP).

In all regions, events containing muons are rejected. As in the signal region summarized in Table 7.1, electrons are required to satisfy $p_{\mathrm{T}}^{e} > 28\,\mathrm{GeV}$, and events are rejected if additional electrons with $p_{\mathrm{T}}^{e} > 10\,\mathrm{GeV}$ are present. The invariant mass of the electron-photon or electron pair must satisfy $71\,\mathrm{GeV} < m_{e\gamma}, m_{ee} < 111\,\mathrm{GeV}$. Additionally, the missing transverse momentum is required to be below $30\,\mathrm{GeV}$, suppressing contributions from processes with genuine neutrinos, such as leptonically decaying top-quark processes, thereby increasing the purity of Z boson events. The separation between control and validation regions ensures that the scale factors are derived in an environment enriched with electrons as well as $e \to \gamma$ fakes, and tested in a topology closer to the signal region. The measurement is performed in six bins of absolute photon pseudorapidity of the associated calorimeter cluster $|\eta_{\mathrm{cl}}^{\gamma}|$, with bin edges given by

$$[0, 0.3), [0.3, 0.6), [0.6, 1.0), [1.0, 1.37), (1.52, 1.81), [1.81, 2.37),$$

and separately for the six photon conversion types defined in Table 5.2, giving a total of 36 bins. The $\mu^{Ze\gamma}$ and μ^{Zee} factors are extracted in the $Z \to e\gamma$ and $Z \to ee$ control regions, respectively:

- Distributions of $m_{e\gamma}$ in each bin, as well as the inclusive m_{ee} distribution, are taken from the nominal MC samples described in Section 4.4. The dominant contributions in both regions arise from Z+jets production.

- For each $|\eta_{\mathrm{cl}}^{\gamma}|$ and conversion-type bin, two binned likelihood fits to the observed data yields are performed, one in each control region. The fit procedure is similar to the procedure described in Section 7.3 but without any constrained nuisance parameters. The likelihoods are constructed as a product of Poisson probabilities over the histogram bins b,

$$\mathcal{L}^{Zee}(\boldsymbol{n}^{\mathrm{data}} \mid \mu^{Zee}) = \prod_b \mathrm{Pois}\big(n_b^{\mathrm{data}} \mid n_b^{\mathrm{pred}}(\mu^{Zee})\big), \tag{8.5}$$

$$\mathcal{L}^{Ze\gamma}(\boldsymbol{n}^{\mathrm{data}} \mid \mu^{Ze\gamma}, \mu^{B_3}, \boldsymbol{\beta}) = \prod_b \mathrm{Pois}\big(n_b^{\mathrm{data}} \mid n_b^{\mathrm{pred}}(\mu^{Ze\gamma}, \mu^{B_3}, \boldsymbol{\beta})\big), \tag{8.6}$$

  where $\boldsymbol{n}^{\mathrm{data}}$ denotes all observed numbers of events n_b^{data}, n_b^{pred} denotes the predicted number of events in bin b, and the normalization factor μ^{B_3} and the parameters $\boldsymbol{\beta}$ are used to model additional contributions in the $Z \to e\gamma$ region via a third-order Bernstein polynomial[1].

- In the $Z \to ee$ control region, the predicted yield is modeled as

$$n_b^{\mathrm{pred}} = \mu^{Zee} \cdot n_b^{Zee} + n_b^{\mathrm{bkg}}, \tag{8.7}$$

  where n_b^{Zee} denotes the contribution from the $Z \to ee$ events and n_b^{bkg} is the sum of all other background contributions. The parameter μ^{Zee} scales the overall normalization of the Z+jets contribution.

- In the $Z \to e\gamma$ control region, the predicted yield is modeled as

$$n_b^{\mathrm{pred}} = \mu^{Ze\gamma} \cdot n_b^{Ze\gamma} + n_b^{\mathrm{bkg}} + \mu^{B_3} \cdot B_3(\boldsymbol{\beta}, m_b), \tag{8.8}$$

  where $n_b^{Ze\gamma}$ denotes the contribution from the $Z \to e\gamma$ events and B_3 is the Bernstein polynomial described above, evaluated at the bin-center mass value m_b, and normalized to $[0, 1]$.

The parameter values of μ^{Zee}, $\mu^{Ze\gamma}$, μ^{B_3}, and the three $\boldsymbol{\beta}$ parameters that maximize the likelihood functions (8.5) and (8.6) are determined in the fits. Conceptually, μ^{Zee} primarily constrains the overall normalization of the Z+jets process using the $Z \to ee$ control region. The parameter $\mu^{Ze\gamma}$ then accounts for possible effects from the mismodeling of $e \to \gamma$ fakes. The final scale factors, derived from the obtained $\mu^{Ze\gamma}$ and μ^{Zee} values according to Equations (8.2) to (8.4), are applied to all $e \to \gamma$ fake background MC contributions.

[1] Bernstein polynomials are linear combinations of polynomials that can approximate the shape of any continuous function. Here, a third-order Bernstein polynomial of the form $B_3(\boldsymbol{\beta}, x) = \big(x^3 + \beta_2 \cdot 3x^2(1-x) + \beta_1 \cdot 3x(1-x)^2 + \beta_0 \cdot (1-x)^3\big)$ is used.

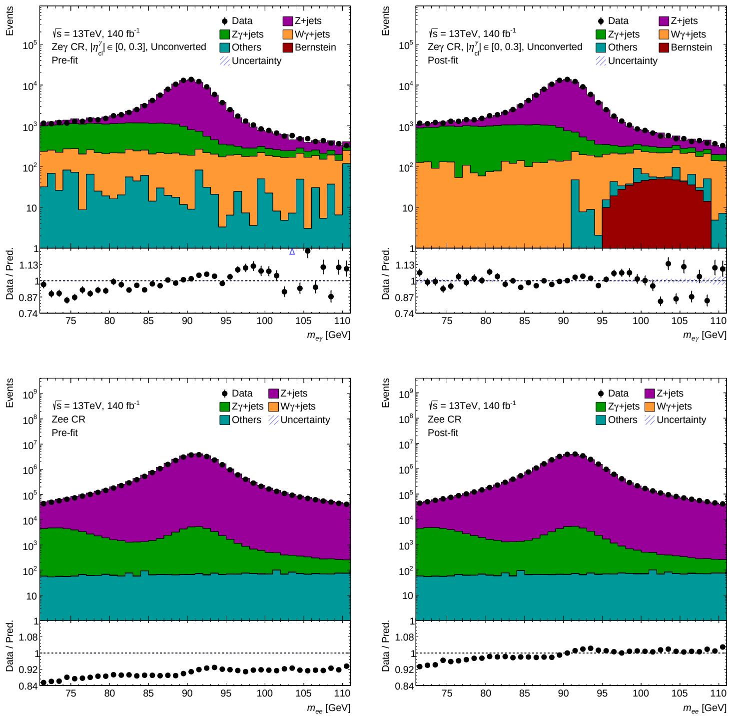

Figure 8.1: Invariant mass distributions in the $Z \to e\gamma$ control region (CR), exemplary for unconverted photons with pseudorapidity $\eta^{\gamma}_{\mathrm{cl}} < 0.3$ (top) and for the $Z \to ee$ CR (bottom), before (left) and after (right) the binned profile likelihood fit. Data (black points) are compared to the stacked MC contributions. The improved post-fit agreement confirms the validity of the fits.

8.1.2 Systematic uncertainties

Systematic uncertainties are estimated by repeating the measurement with alternative assumptions and evaluating the impact on the resulting scale factors. Unless stated otherwise, the absolute difference between the nominal result and the result obtained under the variation is taken as the corresponding uncertainty contribution. The individual contributions are added in quadrature to obtain the total systematic uncertainty, assuming that the different sources are uncorrelated. The variations considered are:

Generator modeling

The nominal Sherpa Z+jets sample is replaced with a sample with an alternative generator setup described in Section 4.4.5, using MadGraph5_aMC@NLO for the matrix element calculations and Pythia for the parton shower modeling.

Rare background modeling
The likelihood fits to the $m_{e\gamma}$ distributions are performed without the third-order Bernstein polynomials.

$Z\gamma$+jets and $W\gamma$+jets contributions
The likelihood fits to the $m_{e\gamma}$ and m_{ee} distributions are performed without including the $Z\gamma$+jets and $W\gamma$+jets MC contributions.

Photon energy calibration
The photon energy calibration is derived for prompt photons and may not fully apply to misidentified electrons. Following the common approach suggested by previous ATLAS studies, this uncertainty is evaluated using symmetric up and down variations of the fake photon energy by $\pm 1\%$. If the nominal result lies between the up and down variations, half of their difference is taken as the uncertainty. Otherwise, the larger deviation with respect to the nominal result is assigned.

Mass window
The invariant mass requirements on $m_{e\gamma}$ and m_{ee} in both CRs are varied from $[71, 111]$ GeV to $[81, 101]$ GeV.

8.1.3 Results: scale factors and uncertainties

The results of the likelihood fits to the $m_{e\gamma}$ and m_{ee} distributions in the $Z \to e\gamma$ and $Z \to ee$ control regions are shown in Figure 8.1. In both cases, the largest contribution arises from the Z+jets process, followed by $Z\gamma$+jets and, in the $Z \to e\gamma$ region, also a smaller $W\gamma$+jets component. Other backgrounds are negligible. The post-fit distributions show improved agreement between data and the combined MC prediction in normalization, and for $m_{e\gamma}$ also in shape, demonstrating that the likelihood fits successfully constrain the normalization factors μ^{Zee} and $\mu^{Ze\gamma}$.

The resulting scale factors $\mathrm{SF}^{e\to\gamma}$ with uncertainties are shown in Figure 8.2 and Table 8.1 as a function of photon pseudorapidity and conversion type. For unconverted and DoubleSi photons, the scale factors are relatively close to unity across all $|\eta^{\gamma}_{\mathrm{cl}}|$ bins, indicating good modeling of these well-reconstructed photon types. In contrast, SingleTRT (SingleSi) photons exhibit larger scale factors, up to about 1.6 (2.0) in the central region, indicating these bins are more sensitive to mismodeling. This is expected because single-track conversion photons closely resemble electrons and are therefore more affected by potential mismodeling of conversion-vertex reconstruction efficiencies and differences in material modeling. Intermediate scale factors are obtained for DoubleTRT and DoubleSiTRT photons, indicating partial mitigation of mismodeling effects due to the presence of two tracks, although the quality of TRT tracks is lower than that of Si tracks. In the central detector region, the presence of the Insertable B-Layer along with multiple high-precision pixel and SCT layers enables very accurate track reconstruction, so the electron-photon classification relies heavily on track-based information. The observed tendency for larger SFs in this region may therefore hint that potential mismodeling of track and vertex reconstruction has a strong effect on the electron-photon classification.

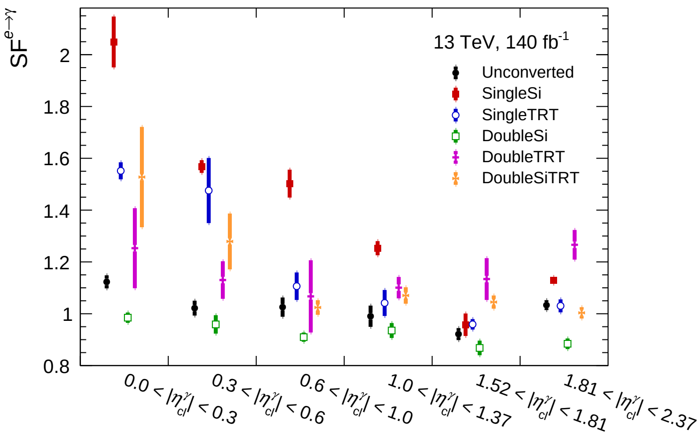

Figure 8.2: The $e \to \gamma$ scale factors $\mathrm{SF}^{e\to\gamma}$ with total statistical and systematic uncertainty as a function of photon pseudorapidity for different conversion types. The scale factors are derived from binned profile likelihood fits in the $Z \to e\gamma$ and $Z \to ee$ control regions.

The statistical uncertainty is generally small compared to the systematic components, reflecting sufficient control region statistics, particularly for the first four conversion types. Among the systematic uncertainties, the generator modeling uncertainty is often dominant. This is expected, since the matrix element and parton shower modeling significantly affect the event kinematics and radiation patterns. Variations in simulated jet activity, parton-level interactions, and photon radiation lead to changes in the reconstructed kinematics and identification efficiencies of leptons and photons, which in turn impact the shapes of the invariant mass distributions used in the likelihood fits. The mass window variation also contributes significantly to the total uncertainty in several bins. The photon energy calibration and rare background uncertainties contribute at an intermediate level, with some exceptions such as the rare background uncertainty for DoubleTRT photons in the lowest $|\eta_{\mathrm{cl}}^{\gamma}|$ bin. Variations from the $V\gamma$ contributions are generally subdominant. Overall, the total uncertainty is larger at small $|\eta_{\mathrm{cl}}^{\gamma}|$, particularly for DoubleTRT and DoubleSiTRT photons, where the lower event counts lead to larger relative fluctuations in the systematic variations. In most bins with $|\eta_{\mathrm{cl}}^{\gamma}| > 0.6$, the total uncertainty remains below 10%.

Table 8.1: The $e \to \gamma$ scale factor results and uncertainties for all photon absolute pseudorapidity $|\eta_{\text{cl}}^{\gamma}|$ and conversion type bins.

Conversion type	$\lvert\eta_{\text{cl}}^{\gamma}\rvert$	$\text{SF}^{e\to\gamma}$	stat.	shower	rare	$V\gamma$	energy	mass	total
Unconverted	[0.0, 0.3]	1.12	±0.01	±0.01	±0.01	±0.01	±0.01	±0.02	±0.03
	[0.3, 0.6]	1.02	±0.01	±0.02	±0.02	±0.01	±0.01	±0.01	±0.03
	[0.6, 1.0]	1.03	±0.01	±0.01	±0.02	±0.01	±0.01	±0.02	±0.04
	[1.0, 1.37]	0.99	±0.01	±0.03	±0.02	±0.01	±0.02	±0.01	±0.04
	[1.52, 1.81]	0.92	±0.01	±0.01	±0.02	±0.01	±0.01	±0.01	±0.02
	[1.81, 2.37]	1.03	±0.01	±0.01	±0.01	±0.01	±0.01	±0.01	±0.02
SingleSi	[0.0, 0.3]	2.05	±0.01	±0.10	±0.01	±0.01	±0.01	±0.01	±0.10
	[0.3, 0.6]	1.57	±0.01	±0.02	±0.01	±0.01	±0.01	±0.01	±0.02
	[0.6, 1.0]	1.50	±0.01	±0.05	±0.01	±0.01	±0.02	±0.01	±0.05
	[1.0, 1.37]	1.25	±0.01	±0.01	±0.02	±0.01	±0.01	±0.02	±0.03
	[1.52, 1.81]	0.96	±0.01	±0.03	±0.02	±0.01	±0.01	±0.02	±0.04
	[1.81, 2.37]	1.13	±0.01	±0.01	±0.01	±0.01	±0.01	±0.01	±0.01
SingleTRT	[0.0, 0.3]	1.55	±0.01	±0.03	±0.01	±0.01	±0.01	±0.01	±0.03
	[0.3, 0.6]	1.48	±0.01	±0.11	±0.04	±0.01	±0.02	±0.05	±0.13
	[0.6, 1.0]	1.11	±0.01	±0.02	±0.02	±0.01	±0.01	±0.04	±0.05
	[1.0, 1.37]	1.04	±0.01	±0.05	±0.01	±0.01	±0.01	±0.01	±0.05
	[1.52, 1.81]	0.96	±0.01	±0.01	±0.01	±0.01	±0.01	±0.02	±0.02
	[1.81, 2.37]	1.03	±0.01	±0.01	±0.01	±0.01	±0.01	±0.02	±0.03
DoubleSi	[0.0, 0.3]	0.98	±0.01	±0.01	±0.01	±0.01	±0.01	±0.01	±0.02
	[0.3, 0.6]	0.96	±0.01	±0.03	±0.01	±0.01	±0.01	±0.01	±0.04
	[0.6, 1.0]	0.91	±0.01	±0.01	±0.01	±0.01	±0.01	±0.01	±0.02
	[1.0, 1.37]	0.94	±0.01	±0.02	±0.02	±0.01	±0.01	±0.01	±0.03
	[1.52, 1.81]	0.87	±0.01	±0.01	±0.02	±0.01	±0.01	±0.02	±0.03
	[1.81, 2.37]	0.88	±0.01	±0.02	±0.01	±0.01	±0.01	±0.01	±0.02
DoubleTRT	[0.0, 0.3]	1.25	±0.03	±0.02	±0.15	±0.01	±0.01	±0.02	±0.15
	[0.3, 0.6]	1.13	±0.03	±0.03	±0.02	±0.01	±0.02	±0.05	±0.07
	[0.6, 1.0]	1.07	±0.03	±0.02	±0.01	±0.01	±0.05	±0.12	±0.14
	[1.0, 1.37]	1.10	±0.01	±0.01	±0.03	±0.01	±0.01	±0.02	±0.04
	[1.52, 1.81]	1.13	±0.01	±0.01	±0.02	±0.01	±0.01	±0.08	±0.08
	[1.81, 2.37]	1.27	±0.02	±0.02	±0.02	±0.01	±0.01	±0.04	±0.06
DoubleSiTRT	[0.0, 0.3]	1.53	±0.04	±0.13	±0.04	±0.01	±0.05	±0.12	±0.19
	[0.3, 0.6]	1.28	±0.02	±0.05	±0.09	±0.01	±0.01	±0.02	±0.11
	[0.6, 1.0]	1.02	±0.02	±0.01	±0.01	±0.01	±0.01	±0.01	±0.03
	[1.0, 1.37]	1.07	±0.01	±0.01	±0.02	±0.01	±0.01	±0.02	±0.03
	[1.52, 1.81]	1.04	±0.01	±0.01	±0.01	±0.01	±0.01	±0.02	±0.03
	[1.81, 2.37]	1.00	±0.01	±0.01	±0.01	±0.01	±0.01	±0.02	±0.02

8.1.4 Validation: photon kinematics in the validation region

The derived scale factors are applied and validated in the $Z \to e\gamma$ validation region, which is kinematically similar to the analysis signal region. Figure 8.3 shows the photon pseudorapidity and conversion-type distributions before and after applying the scale factors. Before as well as after applying the corrections, the MC prediction exceeds the data yields by about 5%, consistent with residual mismodeling not directly addressed by the $e \to \gamma$ scale factors. After applying the scale factors, the agreement between the shapes of the distributions in data and MC improves, indicating that the corrections derived in the control regions are applicable to a topology close to the signal region. This provides confidence in the robustness of the $e \to \gamma$ background estimation.

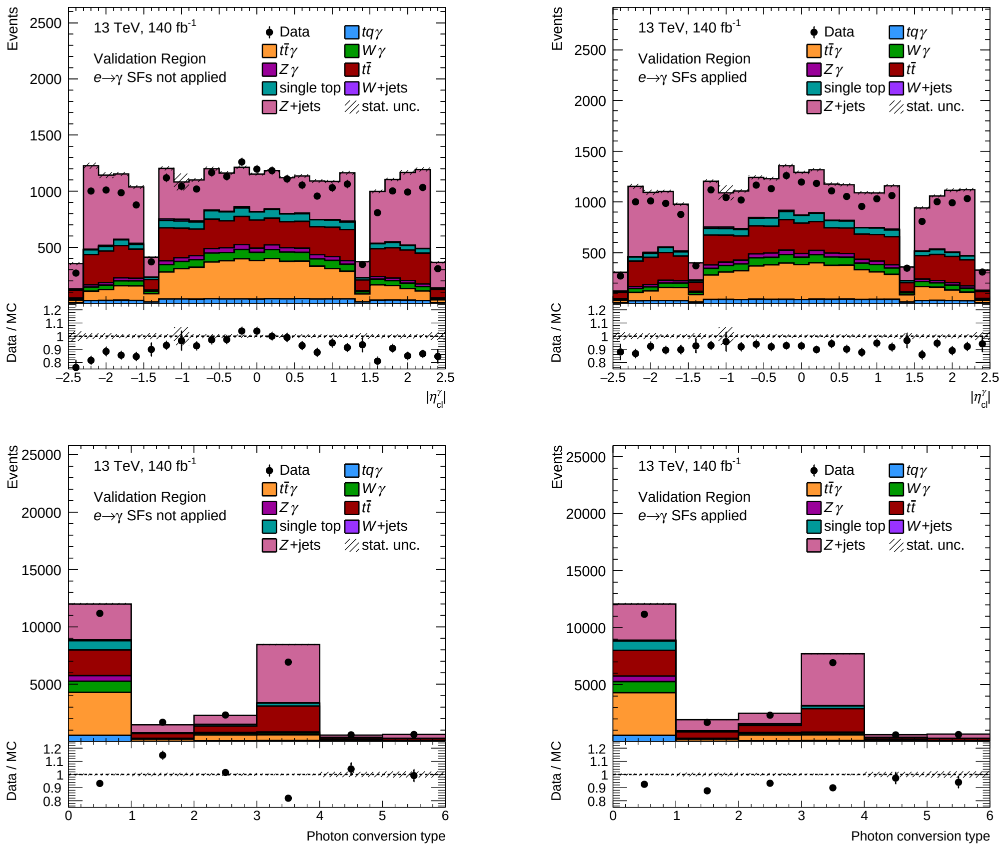

Figure 8.3: Photon pseudorapidity (top) and conversion type (bottom) distributions with statistical uncertainties indicated by the hatched band, in the $Z \to ee$ validation region, shown before (left) and after (right) applying the $e \to \gamma$ scale factors.

8.2 Estimation of background contribution from non-prompt photons as well as hadrons misidentified as photons

The main sources of $h \to \gamma$ fakes are neutral mesons, predominantly neutral pions, which decay into pairs of photons ($\pi^0 \to \gamma\gamma$) before reaching the calorimeters. These photons can be sufficiently collimated to overlap and mimic a single isolated photon in the detector. Additionally, non-prompt photons may originate from secondary decays, for example in jets containing heavy-flavor hadrons.

To estimate this background contribution, the ABCD method [113–115] is employed. The method, associated systematic uncertainties, the results, and validation are presented in the following.

8.2.1 Methodology: ABCD method

The ABCD method relies on constructing four orthogonal regions (region A, B, C, and D) based on two binary selection criteria that are approximately uncorrelated. Regions A, B, and C fail at least one of the two criteria and are therefore enriched in background events. These regions are used to estimate the background contribution in the target region D, which passes both selections.

For the $h \to \gamma$ fake estimation, all four ABCD regions are defined using the signal region as a baseline, but without the photon ID and isolation criteria, as illustrated in Figure 8.4. The isolation criterion is defined in Section 5.2 and used as one of the two ABCD region criteria. To obtain the second criterion, the SSVs used for photon ID are split into two groups as described in Chapter 6: narrow-strip variables and relaxed-tight variables. Because the narrow-strip variables describe the core of the photon shower, they are expected to be only weakly correlated to the photon isolation, which is instead sensitive to the surrounding activity. Consequently, they are used as the second ABCD region criterion. Additionally, all ABCD regions require the photon candidate to pass the relaxed-tight variable cuts. Therefore, passing all SSV cuts as well as isolation, the target region D corresponds to the signal region defined in Section 7.1.

Because of the expected weak correlation between isolation and the narrow-strip variables, the relation

$$\frac{N^{h\to\gamma}_{\text{data}}(A)}{N^{h\to\gamma}_{\text{data}}(B)} \approx \frac{N^{h\to\gamma}_{\text{data}}(D)}{N^{h\to\gamma}_{\text{data}}(C)} \tag{8.9}$$

can be assumed, with $N^{h\to\gamma}_{\text{data}}(X)$ being the $h \to \gamma$ fake yields in data for different regions X. However, in order to account for the actually non-zero correlation

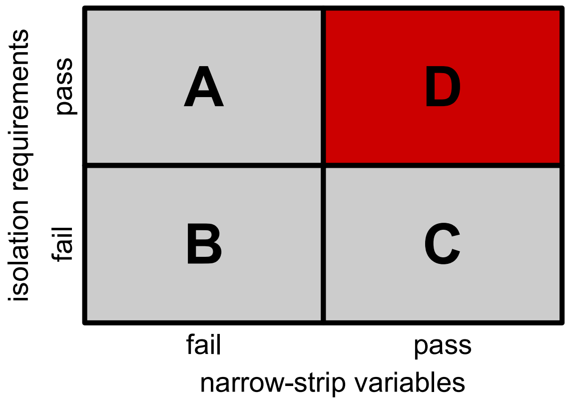

Figure 8.4: Schematic representation of the ABCD region definitions used for the $h \to \gamma$ fake estimation. All regions also require the photon candidate to pass the relaxed-tight variable selection. Regions A, B and C are enriched in $h \to \gamma$ fakes, while region D corresponds to the signal region.

between the two region criteria, a non-closure correction factor θ is calculated. This factor is derived from simulation as

$$\theta = \frac{N_{\text{MC}}^{h\to\gamma}(B)}{N_{\text{MC}}^{h\to\gamma}(A)} \cdot \frac{N_{\text{MC}}^{h\to\gamma}(D)}{N_{\text{MC}}^{h\to\gamma}(C)} \tag{8.10}$$

and applied to Equation (8.9). This leads to:

$$N_{\text{data}}^{h\to\gamma}(D) = \frac{N_{\text{data}}^{h\to\gamma}(A) \cdot N_{\text{data}}^{h\to\gamma}(C)}{N_{\text{data}}^{h\to\gamma}(B)} \cdot \theta. \tag{8.11}$$

The respective $h \to \gamma$ fake yields in data for the background regions are obtained by subtracting the prompt photon and $e \to \gamma$ fake contributions, estimated from MC, from the total yields:

$$N_{\text{data}}^{h\to\gamma}(X) = N_{\text{data}}(X) - N_{\text{MC}}^{\text{prompt}}(X) - \text{SF}^{e\to\gamma} \cdot N_{\text{MC}}^{e\to\gamma}(X) \tag{8.12}$$

The scale factor $\text{SF}^{e\to\gamma}$ is derived as explained in Section 8.1. Finally, data-to-MC scale factors for $h \to \gamma$ fakes are calculated as:

$$\text{SF}^{h\to\gamma} = \frac{N_{\text{data}}^{h\to\gamma}(D)}{N_{\text{MC}}^{h\to\gamma}(D)} \tag{8.13}$$

These scale factors, determined in bins of photon transverse momentum, absolute pseudorapidity and separately for converted and unconverted photons, are applied to all $h \to \gamma$ fake background contributions in MC.

8.2.2 Systematic uncertainties

Several systematic uncertainties are considered in the estimation of the $h \to \gamma$ fake background. These uncertainties arise from the limited size of the dataset, the modeling of the largest background processes and assumptions made during the calculation of $\mathrm{SF}^{h\to\gamma}$. Each source of uncertainty is described in the following. The total uncertainty is computed as the sum in quadrature of the individual components, assuming that the different sources are uncorrelated.

Limited data statistics
The uncertainty arising from limited data statistics is estimated using 1000 pseudo-experiments (PEs). In each experiment, all data yields are randomly varied according to Poisson statistics. For each pseudo-dataset, the full scale factor calculation is repeated, resulting in a Gaussian-like distribution of scale factors. The standard deviation of this distribution is taken as uncertainty.

PEs are used instead of analytic error propagation to capture non-linear effects and correlations in the scale factor calculation. Statistical uncertainties from MC samples are neglected, as the MC event counts are more than an order of magnitude larger than the corresponding data yields and therefore have a negligible impact.

Shower modeling of $t\bar{t}$
Since the $t\bar{t}$ process is the dominant source of $h \to \gamma$ fakes, shower modeling uncertainties are evaluated specifically for this process. For that, the nominal $t\bar{t}$ sample (produced with Pythia8) is replaced with the alternative Herwig7 sample described in Section 4.4.2. The scale factor is recalculated with this sample, and the difference to the nominal result is taken as uncertainty.

Renormalization and factorization scales of $t\bar{t}$ and $t\bar{t}\gamma$
The uncertainty is evaluated independently for the $t\bar{t}$ and $t\bar{t}\gamma$ MC samples by varying the renormalization (μ_R) and factorization (μ_F) scales. For each of the following combinations:

$$\{\mu_R, \mu_F\} \times \begin{Bmatrix} \{0.5, 0.5\}, & \{0.5, 1.0\}, & \{0.5, 2.0\}, \\ \{1.0, 0.5\}, & & \{1.0, 2.0\}, \\ \{2.0, 0.5\}, & \{2.0, 1.0\}, & \{2.0, 2.0\} \end{Bmatrix}$$

the full scale factor calculation is repeated for each variation, and the envelope of the deviations from the nominal result is taken as a symmetric uncertainty.

Cross-section of $t\bar{t}$
The $t\bar{t}$ cross-section is varied up and down by 6%, which reflects the theoretical uncertainty on its inclusive prediction (see Section 4.4.2). For each variation, the

full scale factor calculation is repeated. The larger of the two resulting deviations from the nominal value is taken as symmetric uncertainty.

Non-closure parameter θ
To estimate the uncertainty associated with the non-closure parameter θ, the previously described variations to the $t\bar{t}$ sample are applied in the calculation of θ. These include the use of the alternative Herwig7 sample instead of the nominal Pythia8 sample, variations of the renormalization and factorization scales, and the $\pm 6\%$ variation of the $t\bar{t}$ cross-section. In total, eleven θ values are derived from these variations and used in the scale factor calculation. The largest deviation of the resulting scale factor from the nominal value is taken as uncertainty.

Prompt photon modeling in background regions
To account for the mismodeling of prompt photon contributions in the background regions, the approach described in Ref. [116] is followed. The dominant $t\bar{t}\gamma$ contribution is varied up and down by 15%, while the contributions from other $V\gamma$+jets processes are varied simultaneously by 30% in the same direction. The $h \to \gamma$ scale factors are recalculated, and the larger of the two deviations from the nominal result is taken as uncertainty.

$\mathrm{SF}^{e\to\gamma}$ uncertainty
The impact of $\mathrm{SF}^{e\to\gamma}$ on the subtraction of the $e \to \gamma$ fake contribution from data is evaluated by varying the scale factor up and down within its uncertainty. For each variation, $\mathrm{SF}^{h\to\gamma}$ is recalculated, and the larger deviation from the nominal value is taken as uncertainty.

8.2.3 Results: SFs and uncertainties

To account for dependencies on kinematic properties, the estimation is performed in bins of the photon transverse momentum p_{T}^{γ}, absolute pseudorapidity of the associated calorimeter cluster $|\eta_{\mathrm{cl}}^{\gamma}|$, and separately for converted and unconverted photons:

- p_{T}^{γ} bins: $[20, 40)$ GeV, $[40, \infty)$ GeV
- $|\eta_{\mathrm{cl}}^{\gamma}|$ bins: $[0, 0.3), [0.3, 0.6), [0.6, 1.0), [1.0, 1.37), (1.52, 1.81), [1.81, 2.37]$
- photon conversion status: converted, unconverted

The detector transition region between $1.37 < |\eta_{\mathrm{cl}}^{\gamma}| < 1.52$ is excluded. For unconverted photons, the two highest $|\eta_{\mathrm{cl}}^{\gamma}|$ bins are merged due to limited statistics, resulting in a total of 22 bins.

Figure 8.5 shows the $h \to \gamma$ scale factors with statistical and total systematic uncertainties. The scale factors mostly lie between 1.0 and 1.4, reflecting a general underestimation of the hadron-to-photon fake contribution in simulation. Only in two bins, the scale factors are slightly smaller than one. No strong trends are observed across $|\eta^{\gamma}_{\mathrm{cl}}|$ or between the different p^{γ}_{T} bins. With relatively small statistical uncertainties, the measurement is mostly limited by systematic uncertainties. In addition, Tables 8.2 and 8.3 list the final scale factors in all bins for converted and unconverted photons, respectively, along with the corresponding non-closure parameters, individual uncertainty contributions, and the total uncertainty.

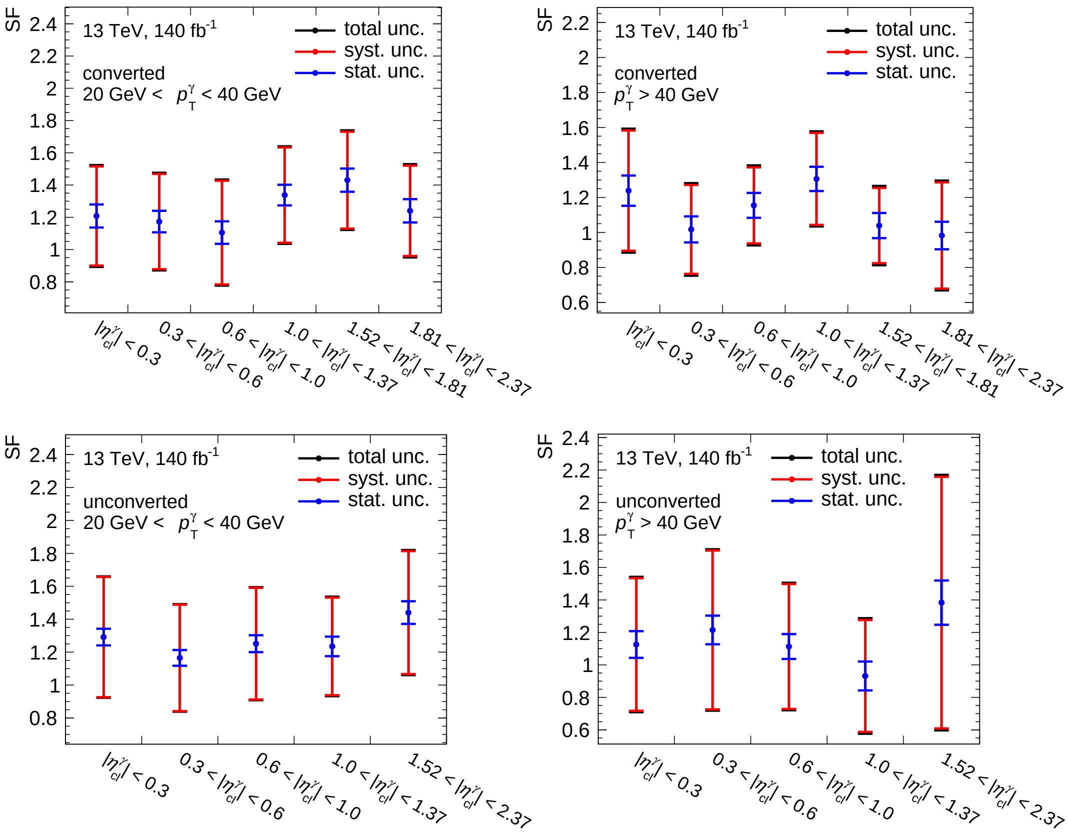

Figure 8.5: Resulting $h \to \gamma$ scale factors as function of $|\eta^{\gamma}_{\mathrm{cl}}|$. Statistical uncertainties, total systematic uncertainties, and the combined total uncertainties are shown. Results for converted photons are displayed in the upper row, results for unconverted photons in the lower row.

Table 8.2: The $h \to \gamma$ scale factor results and uncertainties in all photon absolute pseudorapidity $|\eta^{\gamma}_{\mathrm{cl}}|$ and transverse momentum p^{γ}_{T} bins for converted photons, obtained using the ABCD method.

$\lvert\eta^{\gamma}_{\mathrm{cl}}\rvert$	p^{γ}_{T} [GeV]	$\mathrm{SF}^{h\to\gamma}$	θ	stat	shower	scales $t\bar{t}$	$\sigma_{t\bar{t}}$	scales $t\bar{t}\gamma$	non-clos.	prompt	$\mathrm{SF}^{e\to\gamma}$	total
[0.0, 0.3]	[20, 40]	1.21	1.00	±0.07	±0.18	±0.21	±0.10	±0.05	±0.06	±0.04	±0.02	±0.32
	[40, ∞]	1.24	1.07	±0.09	±0.10	±0.23	±0.11	±0.05	±0.20	±0.04	±0.02	±0.35
[0.3, 0.6]	[20, 40]	1.17	1.09	±0.07	±0.19	±0.19	±0.09	±0.05	±0.01	±0.05	±0.01	±0.30
	[40, ∞]	1.02	1.11	±0.08	±0.03	±0.19	±0.09	±0.05	±0.12	±0.04	±0.03	±0.27
[0.6, 1.0]	[20, 40]	1.11	0.99	±0.07	±0.24	±0.18	±0.09	±0.05	±0.01	±0.05	±0.01	±0.33
	[40, ∞]	1.15	1.08	±0.07	±0.06	±0.18	±0.08	±0.03	±0.05	±0.03	±0.01	±0.23
[1.0, 1.37]	[20, 40]	1.34	1.03	±0.06	±0.16	±0.21	±0.10	±0.05	±0.06	±0.05	±0.01	±0.30
	[40, ∞]	1.31	1.10	±0.07	±0.11	±0.19	±0.09	±0.04	±0.10	±0.03	±0.01	±0.27
[1.52, 1.81]	[20, 40]	1.43	1.15	±0.07	±0.01	±0.23	±0.10	±0.05	±0.15	±0.05	±0.01	±0.31
	[40, ∞]	1.04	1.08	±0.07	±0.05	±0.17	±0.08	±0.04	±0.07	±0.04	±0.01	±0.23
[1.81, 2.37]	[20, 40]	1.24	1.03	±0.07	±0.01	±0.24	±0.11	±0.05	±0.04	±0.05	±0.01	±0.29
	[40, ∞]	0.98	1.10	±0.08	±0.11	±0.24	±0.11	±0.04	±0.07	±0.04	±0.03	±0.31

Table 8.3: The $h \to \gamma$ scale factor results and uncertainties in all photon absolute pseudorapidity $|\eta^{\gamma}_{\mathrm{cl}}|$ and transverse momentum p^{γ}_{T} bins for unconverted photons, obtained using the ABCD method.

$\lvert\eta^{\gamma}_{\mathrm{cl}}\rvert$	p^{γ}_{T} [GeV]	$\mathrm{SF}^{h\to\gamma}$	θ	stat	shower	scales $t\bar{t}$	$\sigma_{t\bar{t}}$	scales $t\bar{t}\gamma$	non-clos.	prompt	$\mathrm{SF}^{e\to\gamma}$	total
[0.0, 0.3]	[20, 40]	1.29	0.99	±0.05	±0.26	±0.18	±0.09	±0.11	±0.06	±0.09	±0.01	±0.37
	[40, ∞]	1.13	1.04	±0.08	±0.23	±0.21	±0.09	±0.17	±0.10	±0.15	±0.02	±0.42
[0.3, 0.6]	[20, 40]	1.17	0.98	±0.05	±0.22	±0.17	±0.08	±0.10	±0.05	±0.09	±0.01	±0.33
	[40, ∞]	1.22	1.00	±0.09	±0.35	±0.21	±0.10	±0.17	±0.07	±0.16	±0.02	±0.50
[0.6, 1.0]	[20, 40]	1.25	1.00	±0.05	±0.24	±0.18	±0.09	±0.10	±0.01	±0.09	±0.01	±0.34
	[40, ∞]	1.11	0.99	±0.08	±0.23	±0.19	±0.09	±0.15	±0.10	±0.13	±0.02	±0.39
[1.0, 1.37]	[20, 40]	1.23	0.95	±0.06	±0.19	±0.18	±0.08	±0.08	±0.01	±0.07	±0.00	±0.30
	[40, ∞]	0.93	1.00	±0.09	±0.22	±0.15	±0.07	±0.13	±0.08	±0.13	±0.02	±0.36
[1.52, 2.37]	[20, 40]	1.44	0.99	±0.08	±0.20	±0.24	±0.11	±0.11	±0.03	±0.12	±0.01	±0.38
	[40, ∞]	1.38	1.07	±0.14	±0.62	±0.33	±0.15	±0.18	±0.11	±0.18	±0.03	±0.79

Figure 8.6 shows the breakdown of individual uncertainty sources contributing to the total uncertainty. The dominant contributions across most bins come from $t\bar{t}$ shower modeling and renormalization/factorization scale variations. This is expected, given that most $h \to \gamma$ fakes originate from $t\bar{t}$ events.

The $t\bar{t}$ shower uncertainty is noticeably smaller in some converted-photon bins at high p^{γ}_{T} and at low p^{γ}_{T} in the end-cap regions. Conversely, it is noticeably larger in the unconverted-photon, high-p^{γ}_{T}, end-cap bin.

The $e \to \gamma$ scale factor uncertainty is negligible in all bins. Other uncertainties contribute at moderate levels, depending on the bin.

The uncertainty associated with the non-closure parameter θ varies significantly. It is generally small for unconverted photons, where θ also stays relatively close to unity across all bins. For some converted-photon bins, the uncertainty is notably larger.

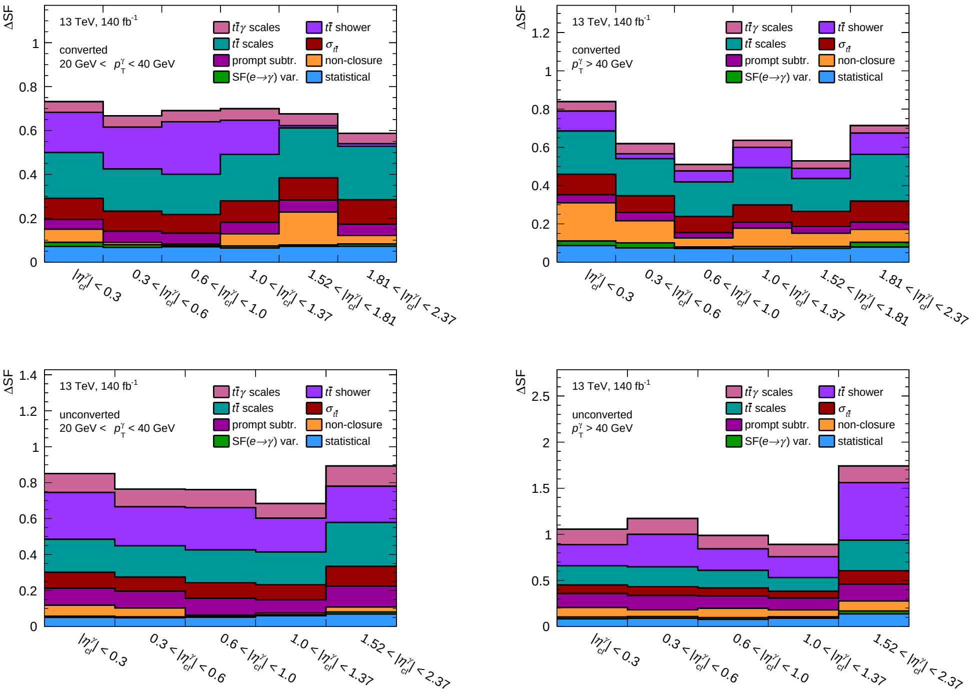

Figure 8.6: Breakdown of systematic uncertainties for the $h\to\gamma$ scale factors as a function of $|\eta_{\text{cl}}^{\gamma}|$, for converted (top) and unconverted (bottom) photons with low (left) and high (right) transverse momentum.

In these, θ can deviate by up to 15% from unity, suggesting that the assumptions of the ABCD method may not hold as well in these kinematic regions. However, the non-closure uncertainty, being evaluated using an envelope of variations, is sensitive to statistical fluctuations in any of these variations. No systematic trend or clear underlying cause is observed. The larger non-closure uncertainties in certain bins are therefore likely due to an unfavorable combination of limited statistics and systematic effects, and can be considered conservative.

8.2.4 Validation: kinematic distributions of photons

Figure 8.7 shows the $|\eta_{\text{cl}}^{\gamma}|$ distributions in the background regions A, B, and C, shown here for the low-p_{T}^{γ} bin. Corresponding distributions for the high-p_{T}^{γ} bin are included in Appendix C. The distributions generally agree in shape between data and simulation, with data yields exceeding simulation by up to around 20%. These higher data yields are consistent with the previously derived $h\to\gamma$ scale factors being mostly larger than one.

Figure 8.8 shows the $|\eta_{\mathrm{cl}}^{\gamma}|$ distribution in the target region D for the low-p_{T}^{γ} bin, before and after applying the $h \rightarrow \gamma$ scale factors. Distributions for the high-p_{T}^{γ} bin are provided in Appendix C. As in the background regions, data yields tend to exceed simulation by up to around 20%. In the target region, the discrepancy is more pronounced for converted photons, particularly in the end-cap regions. Applying the scale factors significantly reduces this discrepancy, especially for converted photons. This confirms that the derived scale factors improve the modeling of the $h \rightarrow \gamma$ fake contribution in the signal region, bringing it into better agreement with the observed data.

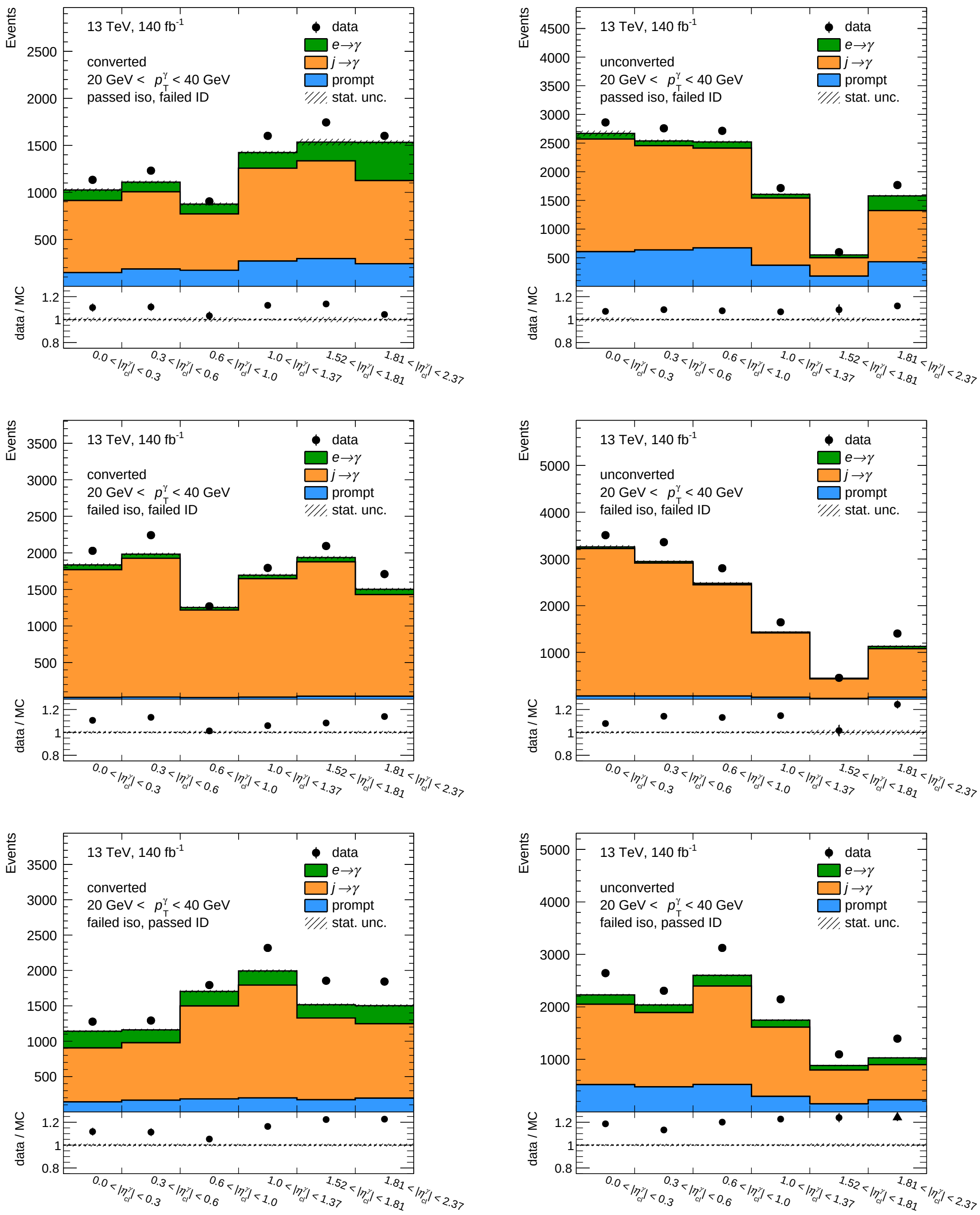

Figure 8.7: Distributions of $|\eta^{\gamma}_{\mathrm{cl}}|$ in the background regions (A, B, C) for converted (left) and unconverted photons (right). The hatched bands represent statistical uncertainties.

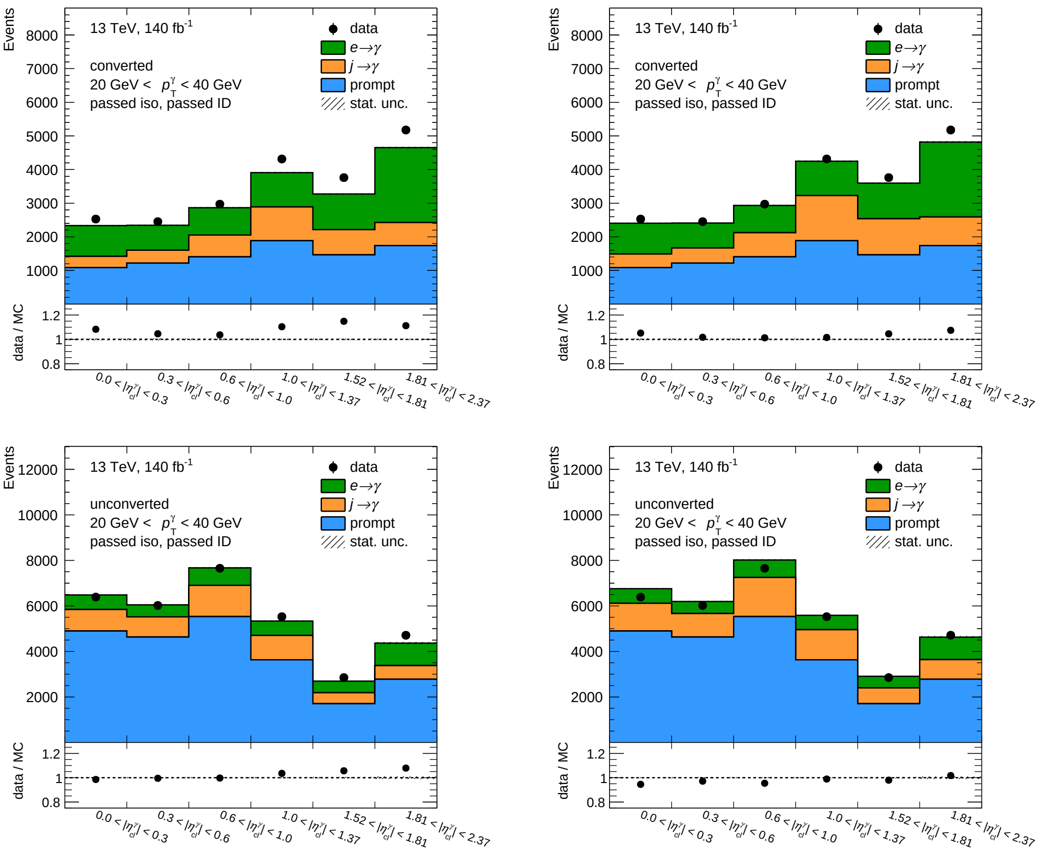

Figure 8.8: Distributions of $|\eta^{\gamma}_{\mathrm{cl}}|$ in the target region (D) for converted (top) and unconverted photons (bottom) before applying the $h\rightarrow\gamma$ scale factors (left) and after applying them (right). The hatched bands represent statistical uncertainties.

9 Signal identification with Neural Networks

The signal region defined in Section 7.1 is enriched in $tq\gamma$ events but still dominated by background processes. To enhance the signal-to-background ratio, a discriminating variable is constructed based on the available observables of the selected objects and event topology. This is achieved using a feed-forward Neural Network trained to distinguish signal-like events from background-like events.

9.1 Introduction to feed-forward Neural Networks

Neural Networks (NNs) are a class of machine learning models capable of approximating complex nonlinear functions. They are widely used in high-energy physics to exploit correlations between multiple observables and improve the discrimination between signal and background processes [117].

9.1.1 Basic structure of a feed-forward Neural Network

A feed-forward NN consists of an input layer, one or more hidden layers, and an output layer. The schematic structure is outlined in Figure 9.1. Each input node corresponds to one input feature (or observable) describing an event. The value of that observable for a given event is propagated to all *neurons* in the first hidden layer. Each hidden layer contains multiple neurons, and each neuron computes a weighted sum z_j of its inputs from the previous layer x_i plus a bias term b_j:

$$z_j = \sum_{i=1}^{N} w_{ij} x_i + b_j = \sum_{i=0}^{N} w_{ij} x_i, \tag{9.1}$$

where N is the number of inputs to the neuron j and w_{ij} are the weights connecting input i to neuron j. The bias term allows the neuron to shift its output independently of the inputs, enabling the NN to account for systematic offsets in the input values. It can equivalently be incorporated into the weight vector by defining $b_j = w_{0j}$ and $x_0 = 1$.

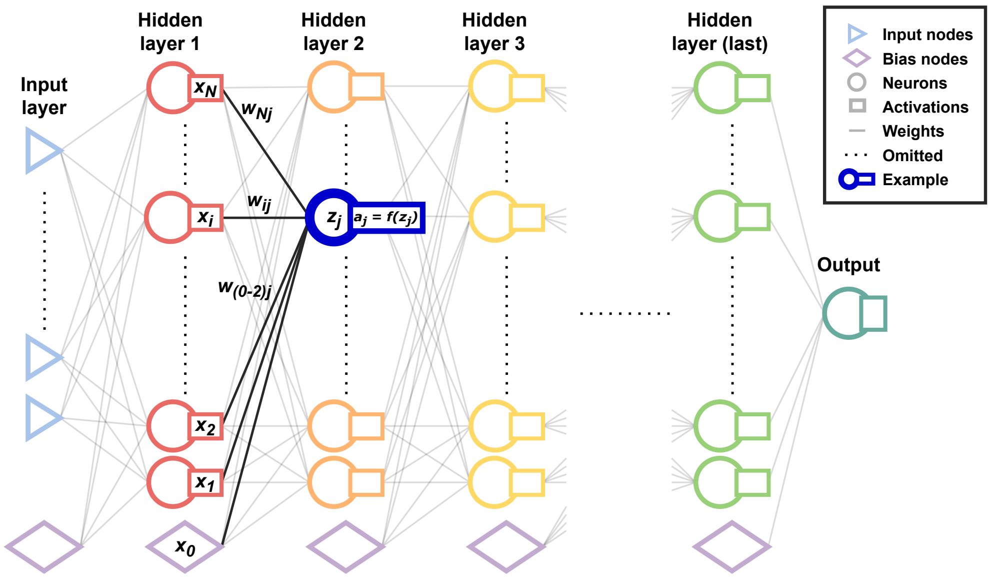

Figure 9.1: Conceptual structure of a feed-forward Neural Network with input, hidden, and output layers. The example neuron illustrates the weighted sum, bias term, and activation function.

An activation function $f(z_j)$ is applied to the weighted sum to produce the output

$$a_j = f(z_j), \tag{9.2}$$

which is then passed as input to all neurons in the next layer. Activation functions introduce non-linearity, enabling the NN to model complex dependencies between input variables. Common activation functions include the sigmoid, tangens hyperbolicus, and *Rectified Linear Unit* (ReLU) functions. In this analysis, the *Leaky ReLU* activation function is used for the hidden layers:

$$f(x) = \begin{cases} x, & \text{if } x \geq 0 \\ \alpha x, & \text{if } x < 0 \end{cases}, \tag{9.3}$$

where α is a small positive number. This function outputs positive values unchanged, which typically form the main contribution to the abstract representation of features in the layer's input. Negative inputs are scaled by α, allowing neurons to make subtle adjustments to the feature representation. This also ensures that neurons never become completely inactive, unlike with the standard ReLU function where negative inputs are set to zero.

The output layer aggregates all outputs from the last hidden layer to produce the NN prediction. In binary classification, a single neuron with a sigmoid activation function is commonly used. The sigmoid function is defined as

$$f(x) = \frac{1}{1 + e^{-x}}, \tag{9.4}$$

mapping input values to the range $(0, 1)$. This output is interpreted as the probability that the event is signal-like.

9.1.2 Training procedure

In high-energy physics, NNs are often trained in a supervised manner using MC events, where the true classification of each event (the *label*) is known. A representative subset of the full MC sample, called the *training set*, is used for this purpose. The goal of the training is to iteratively adjust the NN weights to minimize a loss function that quantifies the difference between predicted and true labels. In this analysis, the *binary cross-entropy* loss function is employed:

$$\mathcal{L} = -\frac{1}{N} \sum_{i=1}^{N} \Big[y_i \log(\hat{y}_i) + (1 - y_i) \log(1 - \hat{y}_i) \Big], \tag{9.5}$$

where N is the number of training events, y_i is the true label of event i, and $\hat{y}_i$ is the predicted probability of the event being signal-like.

Gradients of the loss with respect to the NN weights are computed using *backpropagation* [118]. These gradients are then used by an *optimizer* algorithm to update the weights. Common algorithms include the stochastic gradient descent [119], RMSProp [120], and Adam [121] optimizers. In this analysis, the Adam optimizer is used, which combines adaptive learning rates for each parameter with momentum-based updates to improve convergence and training stability.

During training, the training set is divided into *batches*, which are random subsets of the full training set. After each batch is processed, the weights are updated. The NN is trained over multiple *epochs*, where one epoch corresponds to one full iteration over the entire training set.

9.1.3 Techniques for stable training and generalization

To ensure stable training and that the NN does not simply memorize the training set (a phenomenon known as *overfitting*) but learns features that generalize to unseen events, several standard techniques are often employed. These include:

Input scaling
A common approach is to scale input features to zero mean and unit variance (also called *standard scaling*) to prevent features with large numerical ranges from dominating the gradient updates. Alternative approaches, such as *min-max* normalization, also exist [122]. The scaler is fitted on the training sample and then applied to all events.

Batch normalization
Batch normalization [123] normalizes the outputs of each layer within a batch to have approximately zero mean and unit variance. Batch normalization is typically applied before the activation function, though it can also be applied after. Each neuron has two additional trainable parameters, a scale and a shift, which allow the NN to adjust the normalized values and therefore represent features across a wide range of numeric values. Batch normalization typically leads to faster convergence during training and provides a mild regularization effect, as the mean and variance used for the normalization fluctuate slightly across batches.

Dropout
Dropout [124] is a regularization technique in which the output of a fraction of neurons (chosen at random) is zeroed for each training batch. This prevents the NN from relying too heavily on specific neurons and encourages it to learn redundant, more general feature representations. The fraction of dropped neurons, referred to as the dropout rate, is typically chosen between 0.1 and 0.5 depending on the model complexity and training set size. Dropout is mostly applied in early or middle layers. Later hidden layers are often left intact to allow for the NN to form stable, high-level representations just before the NN output.

Sample splitting and cross-validation
A common approach to assess the generalization performance of a NN is to divide the available MC sample into independent subsets. Typically, the majority of events is used as the already mentioned training set. A smaller subset, the *validation set*, is used to monitor the model performance during training. For example, the NN loss can be evaluated on the validation set after each epoch to detect overfitting. In many applications, a separate *test set* is also reserved to evaluate the final NN performance on fully unseen events.

When MC statistics are limited, reserving separate validation and test sets may significantly reduce the effective training sample size. In such cases, k-fold cross-validation provides an efficient alternative to assess the generalization performance of a NN. The full MC sample is divided into k equally sized and statistically independent subsets, or *folds*. Then, k independent models are trained, each using a different fold as validation set and the remaining $k-1$ folds as training set. Each model is applied to the events of the corresponding validation fold, providing predictions on unseen events. Performance metrics, such as the NN loss, are computed for each fold and averaged across all folds to obtain an overall performance estimate. This approach is computationally more expensive but allows for an efficient use of limited MC statistics, as all events are used for both training and validation. Additionally, cross-validation reduces the dependence on a single random train-validation split. In practice, ATLAS studies most often employ $k = 2$, i.e., two-fold cross-validation, which ensures a robust performance estimation with reasonable computational costs.

9.2 Neural Network input samples and variables

The nominal MC signal and background samples described in Sections 4.3 and 4.4 are used to train and evaluate the NN. In addition, alternative generator samples for the $tq\gamma$, $t\bar{t}\gamma$, and $t\bar{t}$ processes, as well as top-quark-mass variations for the $t\bar{t}$ process, described in Sections 4.3.1, 4.3.2, 4.4.1 and 4.4.2, are included to increase the available statistics for the training. The inclusion of alternative generator samples also reduces the sensitivity to variations in the MC generator setup. For all samples, only events passing the signal-region selection, described in Section 7.1, are used.

Each event is assigned a training weight that determines its relative contribution to the loss function during the NN optimization. These weights are derived from the nominal MC event weights, which already include cross-section normalization and calibration scale factors. For NLO MC samples, events with negative weights can occur. They mainly arise from the subtraction of overlapping contributions between the matrix element calculation and the parton shower algorithm. Events with negative MC weights cannot be used directly for the NN training, as they reverse the sign of the loss contribution and can lead to unstable and poorly behaved gradient updates for the binary cross-entropy loss function. Instead, the absolute values of the weights are used. The negative weights are generally small and are found not to have a large impact on the distributions of the NN input variables. While taking the absolute values increases the overall normalization, the shapes of kinematic distributions are preserved. The normalization is subsequently corrected in the following scaling steps, which also ensure statistically representative and numerically stable training conditions, following the procedure described in Ref. [125]:

1. The top-quark-mass-variation samples contain fewer events than the nominal or generator-variation samples and are therefore assigned proportionally smaller weights.

2. For each process represented by multiple samples (nominal, generator variation, mass variation), the weights are scaled to preserve the overall nominal cross-section.

3. The total sum of weights of signal and background events is equalized while maintaining the internal ratios, including the production-to-decay ratio of $tq\gamma$ events described in Section 4.3. This prevents the NN training from being dominated by the more abundant background events.

The input variables used for the NN are based on the reconstructed final-state objects described in Section 7.1. Low-level features include the transverse momentum (p_{T}), pseudorapidity (η), and azimuthal angle (ϕ) of the photon, lepton, b-tagged jet, and forward jet, defined as the highest-p_{T}^{j} jet with $|\eta| > 2.5$, as well as the missing transverse momentum $E_{\mathrm{T}}^{\mathrm{miss}}$. If no forward jet is present in an event, the corresponding input features are set to a default value. To make it easier for the NN to learn characteristic event topologies, several high-level observables are derived. These include kinematic properties of composite final-state objects (such as the reconstructed W boson, top quark, or combinations of multiple final-state objects), angular distances, and event quantities such as the number of jets and the total scalar transverse momentum H_{T}. An overview of all 39 input features is given in Table 9.1.

Table 9.1: Overview of input features used for Neural Network training. All quantities are derived from reconstructed final-state objects which are the photon (γ), lepton (ℓ), b-tagged jet (b), and forward jet (f), as well as from the reconstructed missing transverse momentum ($E_{\mathrm{T}}^{\mathrm{miss}}$). Lorentz vectors of the W boson and the top quark (t) as well as other composite systems are reconstructed from these objects.

Feature	Description
p_{T}^{X}	transverse momentum of $X \in \{\gamma, \ell, b, f, (\gamma, b), (\gamma, t)\}$
$E_{\mathrm{T}}^{\mathrm{miss}}$	missing transverse momentum
H_{T}	total scalar transverse momentum
E^{X}	energy of $X \in \{(\gamma, f), W\}$
η^{X}	pseudorapidity of $X \in \{\gamma, \ell, b, f\}$
ϕ^{X}	azimuthal angle of $X \in \{\gamma, \ell, b, f, E_{\mathrm{T}}^{\mathrm{miss}}\}$
$\Delta\theta^{X,Y}$	polar-angle distance for $(X, Y) \in \{(f, \gamma), (t, \gamma)\}$
m^{X}	invariant mass of $X \in \{(\gamma, \ell), (\gamma, b), (\gamma, f), (\ell, b), (b, f), t\}$
m_{T}^{X}	transverse mass for $X \in \{(\gamma, \ell, E_{\mathrm{T}}^{\mathrm{miss}}), (\ell, E_{\mathrm{T}}^{\mathrm{miss}}), (\ell, b, E_{\mathrm{T}}^{\mathrm{miss}})\}$
$\Delta\eta^{X,Y}$	pseudorapidity difference for $(X, Y) \in \{(\gamma, b), (\gamma, f), (\ell, b)\}$
$\Delta R^{X,Y}$	angular distance for $(X, Y) \in \{(\gamma, \ell), (\gamma, f), (\ell, b), (\ell, f)\}$
γ_{conv}	photon conversion flag
n_{jets}	number of reconstructed jets

To ensure numerical stability and comparable scales across variables, transformations are applied to several input features. Momentum- and energy-related quantities are expressed on a logarithmic scale to achieve a more even spread across their value ranges. Angles and angle distances (ϕ^X and $\Delta\theta^{X,Y}$) are transformed using their cosine values to account for their periodic nature.

9.3 Neural Network setup

The NN model used in this analysis is implemented using KERAS [126] with a TENSORFLOW [127] backend. It is a fully connected feed-forward NN with an input layer for the 39 features, which are transformed using standard scaling (see Section 9.1.3). The NN has four hidden layers with decreasing sizes of 256, 128, 64, and 32 neurons. The pre-activation output of each hidden layer is followed by batch normalization and then passed through a Leaky ReLU activation with $\alpha = 0.1$ (Equation (9.3)). Dropout with a rate of 0.3 is applied to all hidden layers except the last. The output layer consists of a single neuron with a sigmoid (Equation (9.4)) activation. A schematic overview of the NN architecture is shown in Figure 9.2.

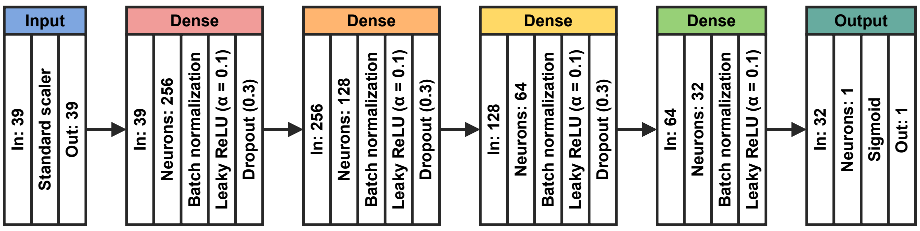

Figure 9.2: Architecture of the feed-forward Neural Network used in this analysis. Each block represents one layer of the model, showing dimensions as well as applied normalizations, activations, and dropout. The model has about $5.4 \cdot 10^4$ trainable weights in total.

The weights of all layers with trainable parameters are initialized using Glorot uniform initialization [128]. The NN is trained with the ADAM optimizer using a learning rate of 10^{-3} and the binary cross-entropy loss function (Equation (9.5)). The batch size is set to 2048 events, and training is performed for 200 epochs. Two-fold cross-validation as described in Section 9.1.3 is applied.

9.4 Results: signal identification

The training progress of the NN is monitored through the training and the validation loss and signal purity evaluated after each epoch. Figure 9.3 shows the evolution of these quantities. The signal purity is determined at a fixed selection cut on the NN output. This cut is chosen such that, after accounting for MC weights, a total of 800 signal events are selected. This value provides a practical compromise between sufficiently high event count and signal purity. It is chosen to be representative of the signal yield in the subsequent differential measurement.

The signal purity after the first training epoch is approximately 57%. The NN further improves the separation during training, with the loss decreasing and the purity increasing up to about 70% for the training set. For the validation set, both the loss and purity gradually converge after approximately 100 epochs, reaching a purity of about 63%. Since convergence occurs well before the final 200$^{\text{th}}$ epoch, the chosen number of epochs is deemed sufficient. The training and validation metrics show a modest difference, indicating stable training and comparable performance on both sets.

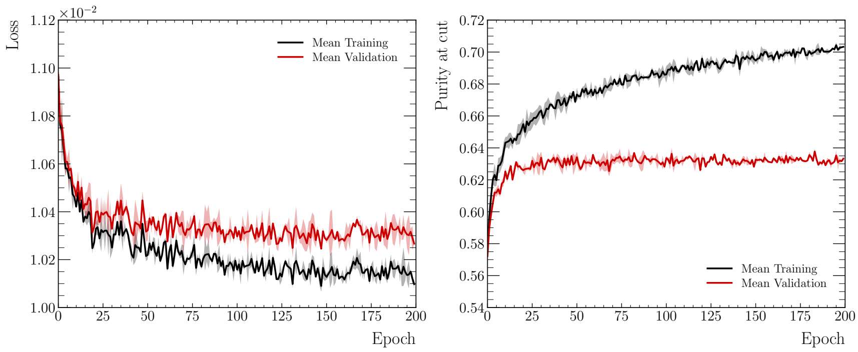

Figure 9.3: Training and validation loss (left) and signal purity at a fixed NN output cut (right) as a function of training epoch. The cut is chosen such that, including event weights, a total of 800 signal events are selected. The solid lines represent the mean across the cross-validation folds, while the shaded areas indicate the envelope spanned by the folds.

The discriminative performance of the trained NN is evaluated on the full input sample using the two-fold cross-validation procedure. Figure 9.4 shows the resulting NN output distribution for all considered processes, alongside the corresponding receiver operating characteristic (ROC) curve. The ROC curve shows the signal efficiency (true positive rate) as a function of the background efficiency (false positive rate) for different NN cut values. The output distribution shows good separation, with background events concentrated near low NN scores, around 0.1, while the signal events predominantly populate the high-score region near 1. The ROC curve quantifies this performance, yielding an area under the curve of 0.87, which indicates strong discriminative power.

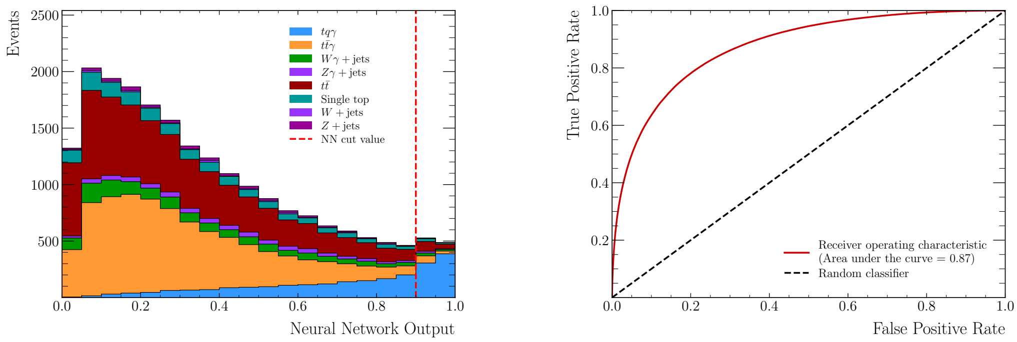

Figure 9.4: Output distribution of the Neural Network for signal and background processes (left), and corresponding Receiver Operating Characteristic curve (right). The Neural Network shows clear separation between signal- and background-dominated regions, with an area under the curve of 0.87.

Overall, the NN successfully distinguishes signal from background, showing stable training behavior and a clear separation in the output distribution. In the following, signal-region events with an NN output larger than 0.9 are referred to as the *NN pass* signal region, while those failing this requirement are referred to as the *NN fail* signal region. The resulting event yields in the signal and control regions are summarised in Table 9.2. The NN pass signal region retains 814 signal events, corresponding to a signal efficiency of about 35% with respect to the inclusive signal region, and a signal purity of about 57%, compared to about 11% before applying the NN selection. This demonstrates that the NN output is a powerful discriminant, providing a solid basis for subsequent differential measurements. The largest background contribution arises from top-quark pair production, contributing about 27%, followed by top-quark pair production in association with a photon at about 7%, while all other backgrounds are subdominant.

The composition of the signal region before and after the NN selection is illustrated in Figure 9.5. A substantial enrichment of the $tq\gamma$ signal contribution is observed. This improvement is primarily driven by a strong suppression of the $t\bar{t}\gamma$ background, whose relative contribution is reduced from about 38% to about 7%. In contrast, backgrounds from misidentified electrons are only mildly reduced, remaining at a level of about 28% in the NN pass signal region. This indicates that $e \to \gamma$ fakes exhibit kinematic properties similar to prompt photons, making them more challenging to distinguish from the signal. The contribution from $h \to \gamma$ fakes is suppressed more strongly, although it remains subdominant in both regions.

Table 9.2: Event yields in the signal region, split by Neural Network selection, and in the two control regions. Uncertainties correspond to statistical uncertainties from the Monte Carlo samples.

Process	NN pass SR	NN fail SR	$t\bar{t}\gamma$ CR	$W\gamma$ CR
$tq\gamma$	814 ± 6	1486 ± 13	605 ± 6	1132 ± 8
$t\bar{t}\gamma$	104 ± 2	7912 ± 16	7739 ± 16	6447 ± 14
$W\gamma$+jets	28 ± 2	1413 ± 17	399 ± 8	$15\,733 \pm 70$
$Z\gamma$+jets	18 ± 1	598 ± 11	164 ± 7	4162 ± 33
$t\bar{t}$	394 ± 8	6526 ± 33	6098 ± 31	5085 ± 28
single top	58 ± 3	1354 ± 15	686 ± 11	1300 ± 15
W+jets	4 ± 2	144 ± 13	29 ± 3	1881 ± 134
Z+jets	15 ± 2	317 ± 11	67 ± 3	1445 ± 55
Total MC	1435 ± 11	$19\,751 \pm 49$	$15\,788 \pm 38$	$37\,184 \pm 169$
Data	1447	19 883	15 182	37 627

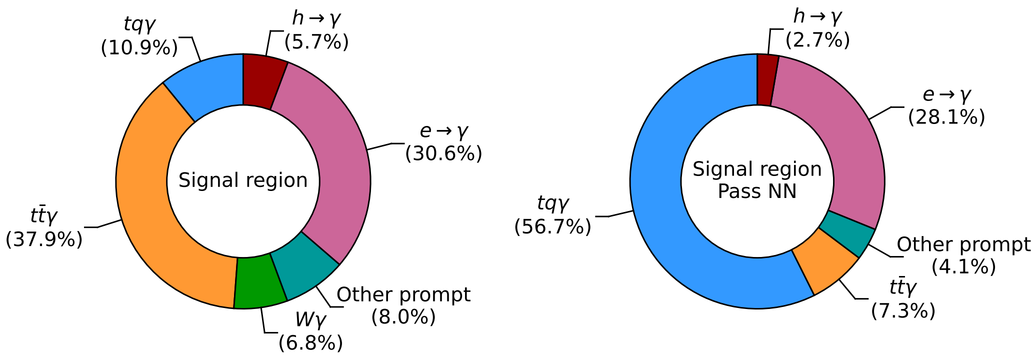

Figure 9.5: Composition of the signal region before (left) and after (right) the Neural Network selection. Shown are the relative contributions of prompt-photon processes, while background processes without matrix-element photon radiation are separated into $e \to \gamma$ and $h \to \gamma$ fakes. The category *Other prompt* includes prompt-photon contributions from these backgrounds as well as all other prompt-photon contributions below 5%.

A comparison between data and simulation in the NN pass signal region as well as the two control regions is shown in Figure 9.6. For the NN pass signal region, the total event yield is in agreement with the prediction at the level of about one percent, well within statistical uncertainties. No significant deviation from the SM expectations is observed. The differential distributions of the photon transverse momentum p_{T}^{γ} and calorimeter-cluster pseudorapidity $\eta_{\mathrm{cl}}^{\gamma}$ show fluctuations consistent with statistical uncertainties, with most bins agreeing within one standard deviation. For the angular distance between the top quark and the photon $\Delta R^{t\gamma}$, good agreement is observed in the central region of the distribution. In the lowest $\Delta R^{t\gamma}$ bins, the data yields tend to be slightly below the prediction, while the highest $\Delta R^{t\gamma}$ bins show a tendency toward slightly higher yields in data. All observed deviations remain within two statistical standard deviations. In the control regions, small deviations between data and simulation are observed. A slight trend towards higher data yields at larger transverse momenta is observed, in particular in the $W\gamma$ control region. Given that only statistical uncertainties are considered at this stage, these deviations do not indicate any significant issue in the modeling of the dominant prompt-photon backgrounds.

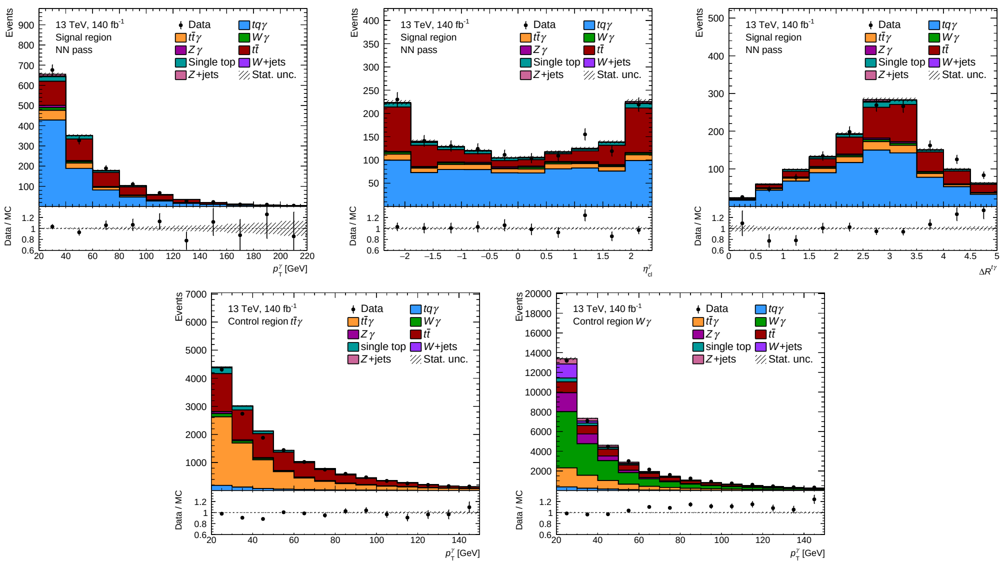

Figure 9.6: Comparison between data and simulation in the signal and control regions. In the signal region, a requirement on the Neural Network output to be greater than 0.9 is applied. Shown are reconstruction-level distributions of the photon transverse momentum p_{T}^{γ} (top left), pseudorapidity $\eta_{\mathrm{cl}}^{\gamma}$ (top center), and the angular distance between the reconstructed top quark and the photon $\Delta R^{t\gamma}$ (top right) in the signal region, as well as p_{T}^{γ} in the $t\bar{t}\gamma$ control region (bottom left) and $W\gamma$ control region (bottom right), with statistical uncertainties.

10 Conclusions and outlook

A detailed study of t-channel single top-quark production in association with a photon ($tq\gamma$) at the ATLAS experiment was presented, using the full Run 2 dataset of proton-proton collisions at a center-of-mass energy of 13 TeV. The $tq\gamma$ process is among the rarest top-quark production modes in the Standard Model (SM). The process has attracted particular interest following previous measurements by the CMS collaboration and the ATLAS collaboration, both of which reported an excess with a significance of about two standard deviations [21, 22]. The analysis components presented and validated in this thesis under updated software and reconstruction conditions are intended to serve as groundwork for a future differential measurement.

A central aspect of the $tq\gamma$ analysis is the modeling of the $tq\gamma$ signal. The simulation of this process requires special treatment, as photon radiation during the decay of the top quark is only available at leading order in dedicated $tq\gamma$ samples. To address this limitation, a stitching procedure was implemented, following the strategy established in the previous inclusive measurement, which combines next-to-leading-order $tq\gamma$ events describing photon radiation in the production stage with single-top t-channel events where photon radiation arises from the decay via the parton shower. The resulting stitched sample provides an effective next-to-leading-order description of the full $tq\gamma$ process. Extensive validation studies at particle and reconstruction level demonstrate that this procedure yields stable kinematic distributions and does not introduce distortions in observables relevant for the analysis.

A precise understanding of the ATLAS photon identification efficiency is essential for the $tq\gamma$ analysis. A measurement of the photon identification efficiency at high photon energies was presented using the Matrix Method, which exploits differences in track isolation properties between prompt and non-prompt photon candidates. The method was validated under the updated ATLAS software and reconstruction conditions. In combination with complementary measurements at lower photon energies, this provides a consistent description of photon identification efficiencies across the full energy range relevant for ATLAS analyses.

The estimation of backgrounds involving misidentified photons constitutes one of the dominant challenges in the $tq\gamma$ analysis. In particular, backgrounds from electrons and hadrons misidentified as photons, as well as non-prompt photons mostly originating from hadron decays, contribute significantly to the signal region. These backgrounds were estimated using data-driven techniques, thereby reducing the reliance on simulation, as photon misidentification is known to be difficult to model accurately. The derived scale factors lead to improved agreement between data and simulation for the studied photon kinematic distributions.

To enhance the separation between signal and background, a Neural-Network-based classifier was trained using kinematic and topological observables. The Neural Network (NN) exhibits effective discrimination power. For events with a NN output greater than 0.9, the selected sample is strongly enriched in $tq\gamma$ events, with a purity of about 57%, compared to about 11% before the NN selection. Good agreement between data and simulation is observed in the NN-selected signal region, with no significant deviations from the SM expectation.

Building on the results presented here, several directions for future work can be outlined. Further gains in signal separation could be achieved through additional optimization of the NN or by employing more advanced architectures, such as Graph Neural Networks, for which a modest performance improvement has already been demonstrated in related studies [125]. The next step, currently under development, is a differential cross-section measurement of the $tq\gamma$ process, which requires unfolding reconstructed distributions to particle level. Candidate observables include photon kinematics and angular separations, which are sensitive to the radiation pattern and the underlying dynamics of the process. With increased statistics expected from Run 3, such measurements can be extended into higher-energy kinematic regions, where potential deviations from the SM may become more pronounced.

In addition, differential $tq\gamma$ measurements can be interpreted in the framework of effective field theories (EFTs). Such EFT interpretations parameterize possible effects of physics beyond the SM through higher-dimensional operators. In this analysis, operators affecting the interaction of the top quark with electroweak gauge bosons are of particular relevance, especially the operators O_{tW} and O_{tB}. The O_{tW} operator modifies the coupling between the top quark and the $\mathrm{SU}(2)_L$ gauge fields. As aconsequence, the $tq\gamma$ process is sensitive to O_{tW} through the production and the decay of the top quark, as well as photon radiation from the top quark. The O_{tB} operator modifies the coupling between the top quark and the $\mathrm{U}(1)_Y$ gauge field. As a result, O_{tB} affects interactions involving neutral gauge bosons, such as photons. Differential $tq\gamma$ measurements are therefore sensitive to both operators. Figure 10.1 summarizes the current constraints on these operators from individual ATLAS and CMS measurements. The O_{tW} operator is constrained by several measurements, with the strongest bounds obtained from a CMS combination of multiple top-quark production processes. In contrast, O_{tB} is currently constrained primarily by ATLAS measurements of top-quark pair production in association with a Z boson or a photon, resulting in somewhat weaker constraints. This highlights the potential of a differential $tq\gamma$ measurement to provide additional sensitivity and further constrain these operators. The work presented in this thesis establishes a validated analysis framework for $tq\gamma$ studies under updated reconstruction conditions and provides a solid basis for such future measurements.

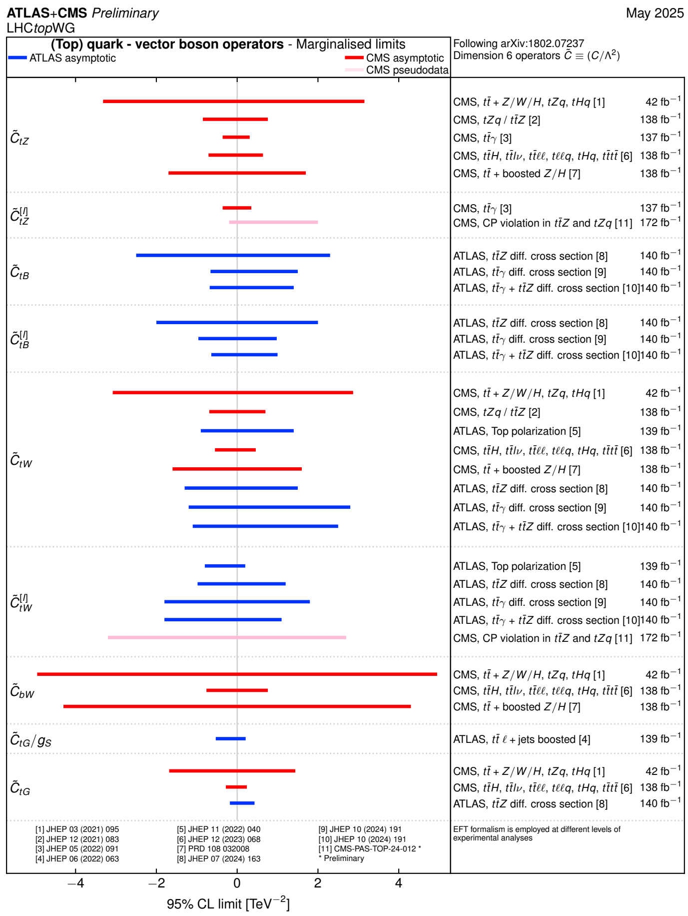

Figure 10.1: Summary of 95% confidence level constraints on selected EFT operators affecting top-quark interactions with gauge bosons, compiled from individual ATLAS and CMS measurements available as of 2025. The horizontal bars indicate 95% confidence limits on so-called *Wilson coefficients* $\tilde{C}$, which quantify the possible strength of new physics contributions at a given energy scale Λ. For the operator O_{tB}, constraints are currently provided by the ATLAS ttZ and $tt\gamma$ measurements, while O_{tW} is constrained by several analyses, with the strongest limits arising from CMS measurements of several top-quark production processes. Figure taken from Ref. [129].

Bibliography

[1] S. L. Glashow, *Partial Symmetries of Weak Interactions*, Nucl. Phys. **22** (1961) 579.

[2] S. Weinberg, *A Model of Leptons*, Phys. Rev. Lett. **19** (1967) 1264.

[3] A. Salam, *Weak and Electromagnetic Interactions*, Conf. Proc. C **680519** (1968) 367.

[4] S. W. Herb et al., *Observation of a dimuon resonance at 9.5 GeV in 400-GeV proton-nucleus collisions*, Phys. Rev. Lett. **39** (1977) 252.

[5] ATLAS Collaboration, *Observation of a new particle in the search for the Standard Model Higgs boson with the ATLAS detector at the LHC*, Phys. Lett. B **716** (2012) 1.

[6] CMS Collaboration, *Observation of a new boson at a mass of 125 GeV with the CMS experiment at the LHC*, Phys. Lett. B **716** (2012) 30.

[7] S. Navas et al., *Review of Particle Physics*, Phys. Rev. D **110** (2024) 030001.

[8] Planck Collaboration, *Planck 2018 results. VI. Cosmological parameters*, Astron. Astrophys. **641** (2020) A6.

[9] A. D. Sakharov, *Violation of CP Invariance, C asymmetry, and baryon asymmetry of the Universe*, JETP Lett. **5** (1967) 24.

[10] ATLAS Collaboration, *The ATLAS experiment at the CERN Large Hadron Collider: a description of the detector configuration for Run 3*, JINST **19** (2024) P05063.

[11] ATLAS Collaboration, *Software Performance of the ATLAS Track Reconstruction for LHC Run 3*, Comput. Softw. Big Sci. **8** (2024) 9.

[12] ATLAS Collaboration, *Development of ATLAS Primary Vertex Reconstruction for LHC Run 3*, ATL-PHYS-PUB-2019-015, 2019, URL: `https://cds.cern.ch/record/2670380`.

[13] ATLAS Collaboration, *Transforming jet flavour tagging at ATLAS*, Nat. Commun. **17** (2026) 541.

[14] C. Bierlich et al., *A comprehensive guide to the physics and usage of PYTHIA 8.3*, SciPost Phys. Codebases (2022) 8.

[15] E. Bothmann et al., *Event generation with Sherpa 3*, JHEP **12** (2024) 156.

[16] G. Bewick et al. *Herwig 7.3 Release Note*. 2024. URL: `https://doi.org/10.1140/epjc/s10052-024-13211-9`.

[17] DØ Collaboration, *Observation of the Top Quark*, Phys. Rev. Lett. **74** (1995) 2632.

[18] CDF Collaboration, *Observation of Top Quark Production in $p\bar{p}$ Collisions*, Phys. Rev. Lett. **74** (1995) 2626.

[19] A. Djouadi, *The anatomy of electroweak symmetry breaking Tome II: The Higgs bosons in the Minimal Supersymmetric Model*, Phys. Rep. **459** (2008) 1.

[20] W. Bernreuther, *Top quark physics at the LHC*, J. Phys. G **35** (2008) 083001.

[21] CMS Collaboration, *Evidence for the Associated Production of a Single Top Quark and a Photon in Proton-Proton Collisions at $\sqrt{s} = 13$ TeV*, Phys. Rev. Lett. **121** (2018) 221802.

[22] ATLAS Collaboration, *Observation of Single-Top-Quark Production in Association with a Photon Using the ATLAS Detector*, Phys. Rev. Lett. **131** (2023) 181901.

[23] ATLAS Collaboration, *Top cross section summary plots*, 2025, URL: `https://atlas.web.cern.ch/Atlas/GROUPS/PHYSICS/PUBNOTES/ATL-PHYS-PUB-2025-024/`, (accessed 2026-01-19).

[24] C. Burgard and D. Galbraith, *Standard model of physics*, 2012, URL: `https://texample.net/tikz/examples/model-physics/`, (accessed 2024-10-22).

[25] Super-Kamiokande Collaboration, *Evidence for Oscillation of Atmospheric Neutrinos*, Phys. Rev. Lett. **81** (1998) 1562.

[26] SNO Collaboration, *Direct Evidence for Neutrino Flavor Transformation from Neutral-Current Interactions in the Sudbury Neutrino Observatory*, Phys. Rev. Lett. **89** (2002) 011301.

[27] M. Fael and T. Gehrmann, *Probing top quark electromagnetic dipole moments in single-top-plus-photon production*, Phys. Rev. D **88** (2013) 033003.

[28] S. M. Etesami, S. Khatibi, and M. M. Najafabadi, *Measuring anomalous $WW\gamma$ and $t\bar{t}\gamma$ couplings using top+γ production at the LHC*, Eur. Phys. J. C **76** (2016) 533.

[29] ATLAS Collaboration, *Measurement of single top-quark production in the s-channel in proton-proton collisions at $\sqrt{s}$ = 13 TeV with the ATLAS detector*, JHEP **06** (2023) 191.

[30] N. Kidonakis and N. Yamanaka, *Higher-order corrections for tW production at high-energy hadron colliders*, JHEP **05** (2021) 278.

[31] J. Campbell, T. Neumann, and Z. Sullivan, *Single-top-quark production in the t-channel at NNLO*, JHEP **02** (2021) 040.

[32] L. Evans and P. Bryant, *LHC Machine*, JINST **3** (2008) S08001.

[33] ALICE Collaboration, *The ALICE experiment at the CERN LHC*, JINST **3** (2008) S08002.

[34] LHCb Collaboration, *The LHCb Detector at the LHC*, JINST **3** (2008) S08005.

[35] CMS Collaboration, *The CMS Experiment at the CERN LHC*, JINST **3** (2008) S08004.

[36] ATLAS Collaboration, *The ATLAS Experiment at the CERN Large Hadron Collider*, JINST **3** (2008) S08003.

[37] ATLAS Collaboration, *Production and integration of the ATLAS Insertable B-Layer*, JINST **13** (2018) T05008.

[38] ATLAS Collaboration, *ATLAS Insertable B-Layer Technical Design Report*, CERN-LHCC-2010-013; ATLAS-TDR-19, 2010, URL: `https://cds.cern.ch/record/1291633`.

[39] ATLAS Collaboration, *ATLAS Insertable B-Layer Technical Design Report Addendum*, CERN-LHCC-2012-009; ATLAS-TDR-19-ADD-1, 2012, URL: `https://cds.cern.ch/record/1451888`.

[40] E. Lopienska, *The CERN accelerator complex, layout in 2022. Complexe des accélérateurs du CERN en janvier 2022*, 2022, URL: `https://cds.cern.ch/record/2800984`, (accessed 2026-01-19).

[41] ATLAS Collaboration, *Luminosity determination in pp collisions at $\sqrt{s} =$ 13 TeV using the ATLAS detector at the LHC*, Eur. Phys. J. C **83** (2023) 982.

[42] ATLAS Collaboration, *Luminosity Public Results Run 2*, 2025, URL: `https://twiki.cern.ch/twiki/bin/view/AtlasPublic/LuminosityPublicResultsRun2`, (accessed 2026-07-22).

[43] ATLAS Collaboration, *Operation of the ATLAS trigger system in Run 2*, JINST **15** (2020) P10004.

[44] J. C. Collins, D. E. Soper, and G. Sterman, *Factorization of Hard Processes in QCD*, Perturbative Quantum Chromodynamics, Adv. Ser. Direct. High Energy Phys **5** (1989) 1.

[45] B. Andersson et al., *Parton Fragmentation and String Dynamics*, Phys. Rept. **97** (1983) 31.

[46] B. Andersson, *The Lund model*, Nucl. Phys. A **461** (1987) 513.

[47] B. R. Webber, *A QCD Model for Jet Fragmentation Including Soft Gluon Interference*, Nucl. Phys. B **238** (1984) 492.

[48] JC. Winter, F. Krauss, and G. Soff, *A modified cluster-hadronisation model*, Eur. Phys. J. C **36** (2004) 381.

[49] T. Sjöstrand, S. Mrenna, and P. Skands, *A brief introduction to PYTHIA 8.1*, Comput. Phys. Commun. **178** (2008) 852.

[50] ATLAS Collaboration, *Measurement of the Inelastic Proton-Proton Cross Section at $\sqrt{s}$ = 13 TeV with the ATLAS Detector at the LHC*, Phys. Rev. Lett. **117** (2016) 182002.

[51] NNPDF Collaboration, *Parton distributions with LHC data*, Nucl. Phys. B **867** (2013) 244.

[52] J. Alwall et al., *The automated computation of tree-level and next-to-leading order differential cross sections, and their matching to parton shower simulations*, JHEP **07** (2014) 079.

[53] S. Frixione, G. Ridolfi, and P. Nason, *A positive-weight next-to-leading-order Monte Carlo for heavy flavour hadroproduction*, JHEP **09** (2007) 126.

[54] P. Nason, *A new method for combining NLO QCD with shower Monte Carlo algorithms*, JHEP **11** (2004) 040.

[55] S. Frixione, P. Nason, and C. Oleari, *Matching NLO QCD computations with parton shower simulations: the POWHEG method*, JHEP **11** (2007) 070.

[56] S. Alioli et al., *A general framework for implementing NLO calculations in shower Monte Carlo programs: the POWHEG BOX*, JHEP **06** (2010) 043.

[57] M. Bähr et al., *Herwig++ physics and manual*, Eur. Phys. J. C **58** (2008) 639.

[58] D. J. Lange, *The EvtGen particle decay simulation package*, Nucl. Instrum. Meth. A **462** (2001) 152.

[59] E. Bothmann et al., *Event generation with Sherpa 2.2*, SciPost Phys. **7** (2019) 034.

[60] GEANT4 collaboration, *GEANT4 - A Simulation Toolkit*, Nucl. Instrum. Meth. A **506** (2003) 250.

[61] ATLAS Collaboration, *The ATLAS Simulation Infrastructure*, Eur. Phys. J. C **70** (2010) 823.

[62] P. Artoisenet et al., *Automatic spin-entangled decays of heavy resonances in Monte Carlo simulations*, JHEP **03** (2013) 015.

[63] NNPDF Collaboration, *Parton distributions for the LHC run II*, JHEP **04** (2015) 040.

[64] ATLAS Collaboration, *ATLAS Pythia 8 tunes to* 7 *TeV data*, ATL-PHYS-PUB-2014-021, 2014, URL: `https://cds.cern.ch/record/1966419`.

[65] J. Bellm et al., *Herwig 7.0/Herwig++ 3.0 release note*, Eur. Phys. J. C **76** (2016) 196.

[66] J. Bellm et al., *Herwig 7.2 release note*, Eur. Phys. J. C **80** (2020) 452.

[67] T. Sjöstrand et al., *An introduction to PYTHIA 8.2*, Comput. Phys. Commun. **191** (2015) 159.

[68] M. Aliev et al., *HATHOR – HAdronic Top and Heavy quarks crOss section calculatoR*, Comput. Phys. Commun. **182** (2011) 1034.

[69] P. Kant et al., *HatHor for single top-quark production: Updated predictions and uncertainty estimates for single top-quark production in hadronic collisions*, Comput. Phys. Commun. **191** (2015) 74.

[70] J. Bellm et al., *Herwig 7.1 Release Note*, arXiv:1705.06919, 2017.

[71] M. Cacciari, G. P. Salam, and G. Soyez, *The Catchment Area of Jets*, JHEP **04** (2008) 005.

[72] K. Melnikov, M. Schulze, and A. Scharf, *QCD corrections to top quark pair production in association with a photon at hadron colliders*, Phys. Rev. D **83** (2011) 074013.

[73] M. Czakon and A. Mitov, *Top++: A Program for the Calculation of the Top-Pair Cross-Section at Hadron Colliders*, Comput. Phys. Commun. **185** (2014) 2930.

[74] J. Butterworth et al., *PDF4LHC recommendations for LHC Run II*, J. Phys. G **43** (2016) 023001.

[75] A. D. Martin et al., *Parton distributions for the LHC*, Eur. Phys. J. C **63** (2009) 189.

[76] A. D. Martin et al., *Uncertainties on α_S in global PDF analyses and implications for predicted hadronic cross sections*, Eur. Phys. J. C **64** (2009) 653.

[77] L. Hung-Liang et al., *New parton distributions for collider physics*, Phys. Rev. D **82** (2010) 074024.

[78] J. Gao et al., *CT10 next-to-next-to-leading order global analysis of QCD*, Phys. Rev. D **89** (2014) 033009.

[79] S. Frixione et al., *Single-top hadroproduction in association with a W boson*, JHEP **07** (2008) 029.

[80] S. Höche et al., *QCD matrix elements and truncated showers*, JHEP **05** (2009) 053.

[81] T. Gleisberg and S. Höche, *Comix, a new matrix element generator*, JHEP **12** (2008) 039.

[82] F. Cascioli, P. Maierhöfer, and S. Pozzorini, *Scattering Amplitudes with Open Loops*, Phys. Rev. Lett. **108** (2012) 111601.

[83] A. Denner, S. Dittmaier, and L. Hofer, *Collier: A Fortran-based complex one-loop library in extended regularizations*, Comput. Phys. Commun. **212** (2017) 220.

[84] F. Buccioni et al., *OpenLoops 2*, Eur. Phys. J. C **79** (2019) 866.

[85] R. Frederix and S. Frixione, *Merging meets matching in MC@NLO*, JHEP **12** (2012) 061.

[86] S. Höche et al., *QCD matrix elements + parton showers. The NLO case*, JHEP **4** (2013) 027.

[87] S. Catani et al., *QCD matrix elements + parton showers*, JHEP **11** (2001) 063.

[88] T. Cornelissen et al., *The new ATLAS track reconstruction (NEWT)*, J. Phys.: Conf. Ser. **119** (2008) 032014.

[89] ATLAS Collaboration, *Performance of the ATLAS track reconstruction algorithms in dense environments in LHC Run 2*, Eur. Phys. J. C **77** (2017) 673.

[90] R. Frühwirth, *Application of Kalman filtering to track and vertex fitting*, Nucl. Instrum. Meth. A **262** (1987) 444.

[91] ATLAS Collaboration, *Muon reconstruction and identification efficiency in ATLAS using the full Run 2 pp collision data set at $\sqrt{s} = 13\,\text{TeV}$*, Eur. Phys. J. C **81** (2021) 578.

[92] ATLAS Collaboration, *Electron and photon efficiencies in LHC Run 2 with the ATLAS experiment*, JHEP **5** (2024) 162.

[93] ATLAS Collaboration, *Electron and photon performance measurements with the ATLAS detector using the 2015-2017 LHC proton-proton collision data*, JINST **14** (2019) P12006.

[94] ATLAS Collaboration, *Measurement of the photon identification efficiencies with the ATLAS detector using LHC Run 2 data collected in 2015 and 2016*, Eur. Phys. J. C **79** (2019) 205.

[95] ATLAS Collaboration, *Jet reconstruction and performance using particle flow with the ATLAS Detector*, Eur. Phys. J. C **77** (2017) 466.

[96] G. P. Salam M. Cacciari and G. Soyez, *The anti-k_t jet clustering algorithm*, JHEP **04** (2008) 063.

[97] ATLAS Collaboration, *Performance of pile-up mitigation techniques for jets in pp collisions at $\sqrt{s} = 8$ TeV using the ATLAS detector*, Eur. Phys. J. C **76** (2016) 581.

[98] ATLAS Collaboration, *The performance of missing transverse momentum reconstruction and its significance with the ATLAS detector using 140 fb^{-1} of $\sqrt{s} = 13$ TeV pp collisions*, Eur. Phys. J. C **85** (2025) 606.

[99] ATLAS Collaboration, *Reconstruction of primary vertices at the ATLAS experiment in Run 1 proton–proton collisions at the LHC*, Eur. Phys. J. C **77** (2017) 332.

[100] ATLAS Collaboration, *ATLAS b-jet identification performance and efficiency measurement with $t\bar{t}$ events in pp collisions at $\sqrt{s} = 13$ TeV*, Eur. Phys. J. C **79** (2019) 970.

[101] ATLAS Collaboration, *Secondary vertex finding for jet flavour identification with the ATLAS detector*, ATL-PHYS-PUB-2017-011, 2017, URL: https://cds.cern.ch/record/2270366.

[102] ATLAS Collaboration, *Identification of Jets Containing b-Hadrons with Recurrent Neural Networks at the ATLAS Experiment*, ATL-PHYS-PUB-2017-003, 2017, URL: https://cds.cern.ch/record/2255226.

[103] ATLAS Collaboration, *Topological b-hadron decay reconstruction and identification of b-jets with the JetFitter package in the ATLAS experiment at the LHC*, ATL-PHYS-PUB-2018-025, 2018, URL: ttps://cds.cern.ch/record/2645405.

[104] A. Höcker et al., *TMVA – Toolkit for Multivariate Data Analysis*, PoS (PhyStat2007) 040 (2007).

[105] J. L. Späh, *Data-driven corrections to shower shape variables for photon identification at the ATLAS experiment*, Master's thesis, Technical University Dortmund, (2021).

[106] ATLAS Collaboration, *Electron reconstruction and identification in the ATLAS experiment using the 2015 and 2016 LHC proton–proton collision data at $\sqrt{s} = 13$ TeV*, Eur. Phys. J. C **79** (2019) 639.

[107] ATLAS Collaboration, *Photon identification in 2015 ATLAS data*, ATL-PHYS-PUB-2016-014, 2016, URL: https://cds.cern.ch/record/2203125.

[108] ATLAS Collaboration, *Measurement of the photon identification efficiencies with the ATLAS detector using LHC Run-1 data*, Eur. Phys. J. C **76** (2016) 666.

[109] ATLAS Collaboration, *Performance of electron and photon triggers in ATLAS during LHC Run 2*, Eur. Phys. J. C **80** (2020) 47.

[110] A. Valassi and R. Chierici, *Information and treatment of unknown correlations in the combination of measurements using the BLUE method*, Eur. Phys. J. C **74** (2014) 2717.

[111] ATLAS Collaboration, *TRExFitter*, version 1.6.0 (2025), URL: `https://doi.org/10.5281/zenodo.14845712`, (accessed 2026-01-20).

[112] F. James and M. Roos, *Minuit - a system for function minimization and analysis of the parameter errors and correlations*, Comput. Phys. Commun. **10** (1975) 343.

[113] S. Choi and H. Oh, *Improved extrapolation methods of data-driven background estimations in high energy physics*, Eur. Phys. J. C **81** (2021) 643.

[114] G. Kasieczka et al., *Automating the ABCD method with machine learning*, Phys. Rev. D **103** (2021) 035021.

[115] M. R. Rahman, *Background estimation in the search for single production of vector-like quarks decaying into Wb in pp collisions using a data-driven method at $\sqrt{s} = 13$ TeV with the ATLAS detector*, arXiv:2106.03961, 2021.

[116] ATLAS Collaboration, *Measurement of the $Z(\rightarrow \ell^+\ell^-)\gamma$ production cross-section in pp collisions at $\sqrt{s} = 13\,\text{TeV}$ with the ATLAS detector*, JHEP **3** (2020) 54.

[117] I. Goodfellow, Y. Bengio, and A. Courville, *Deep Learning*, MIT Press (2016). Available at: `https://www.deeplearningbook.org/`.

[118] D. E. Rumelhart, G. E. Hinton, and R. J. Williams, *Learning representations by back-propagating errors*, Nature **323** (1986) 533.

[119] H. Robbins and S. Monro, *A Stochastic Approximation Method*, Ann. Math. Stat. **22** (1951) 400.

[120] A. Graves, *Generating Sequences With Recurrent Neural Networks*, arXiv:1308.0850, 2014.

[121] Diederik P. Kingma and Jimmy Ba, *Adam: A Method for Stochastic Optimization*, arXiv:1412.6980, 2017.

[122] F. Pedregosa et al., *Scikit-learn: Machine Learning in Python*, 2011, URL: `https://scikit-learn.org/stable/`, (accessed 2026-01-20).

[123] S. Ioffe and C. Szegedy, *Batch Normalization: Accelerating Deep Network Training by Reducing Internal Covariate Shift*, arXiv:1502.03167, 2015.

[124] N. Srivastava et al., *Dropout: A Simple Way to Prevent Neural Networks from Overfitting*, J. Mach. Learn. Res. **15** (2014) 1929.

[125] M. Andreß, *Using Neural Networks to Identify Pure Signal Regions for $tq\gamma$ Production at the ATLAS Experiment*, Master's thesis, Technical University Dortmund, (2025).

[126] F. Chollet et al., *Keras*, 2015, URL: `https://keras.io`, (accessed 2026-01-20).

[127] M. Abadi et al., *TensorFlow: A system for large-scale machine learning*, arXiv:1605.08695, 2016.

[128] X. Glorot and Y. Bengio, *Understanding the difficulty of training deep feedforward neural networks*, Proceedings of the Thirteenth International Conference on Artificial Intelligence and Statistics (AISTATS) **9** (2010) 249.

[129] ATLAS and CMS Collaborations, *(Top) quark - vector boson operators*, 2025, URL: `https://atlas.web.cern.ch/Atlas/GROUPS/PHYSICS/PUBNOTES/ATL-PHYS-PUB-2025-028/`, (accessed 2026-04-07).

Appendices

A Single-top-quark + photon signal modeling

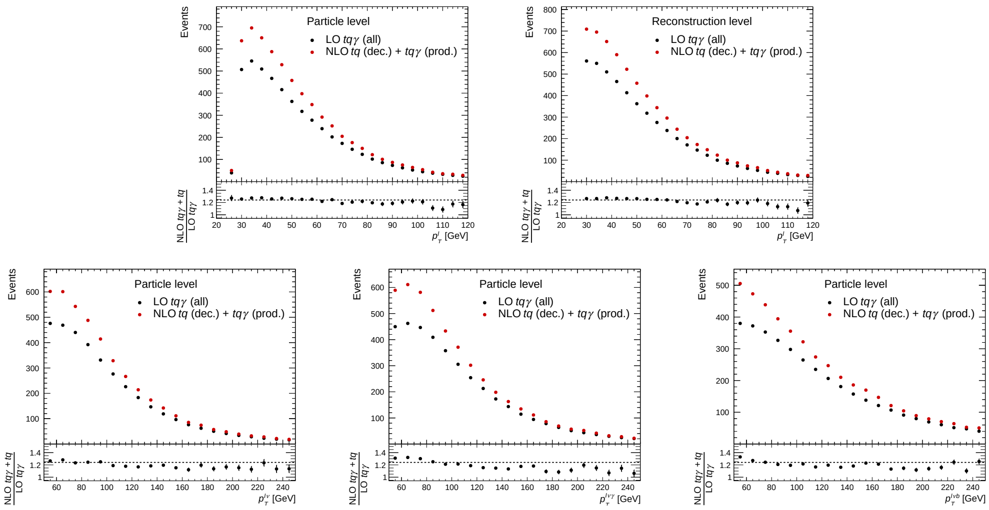

Figure A.1: Transverse momentum distributions for the $tq\gamma$ LO sample and the stitched signal sample. The upper row shows the lepton transverse momentum p_{T}^{ℓ} at particle-level (left) and reconstruction-level (right). The lower row shows particle-level transverse momenta of the systems formed by the lepton and neutrino $p_{\mathrm{T}}^{\ell\nu}$, the lepton, neutrino and photon $p_{\mathrm{T}}^{\ell\nu\gamma}$, as well as the lepton, neutrino and b-jet $p_{\mathrm{T}}^{\ell\nu b}$. The lower panels display the ratios between the stitched and LO samples.

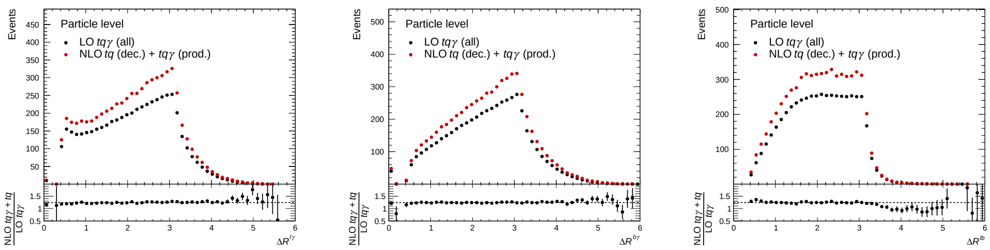

Figure A.2: Particle-level angular separation of the lepton and the photon $\Delta R^{\ell\gamma}$ (left), the b-jet and the photon $\Delta R^{b\gamma}$ (middle), as well as the lepton and the b-jet $\Delta R^{\ell b}$ (right), for the $tq\gamma$ LO sample and the stitched signal sample. The lower panels display the ratios between the stitched and LO samples.

B Photon identification efficiency measurement at ATLAS at high photon energies

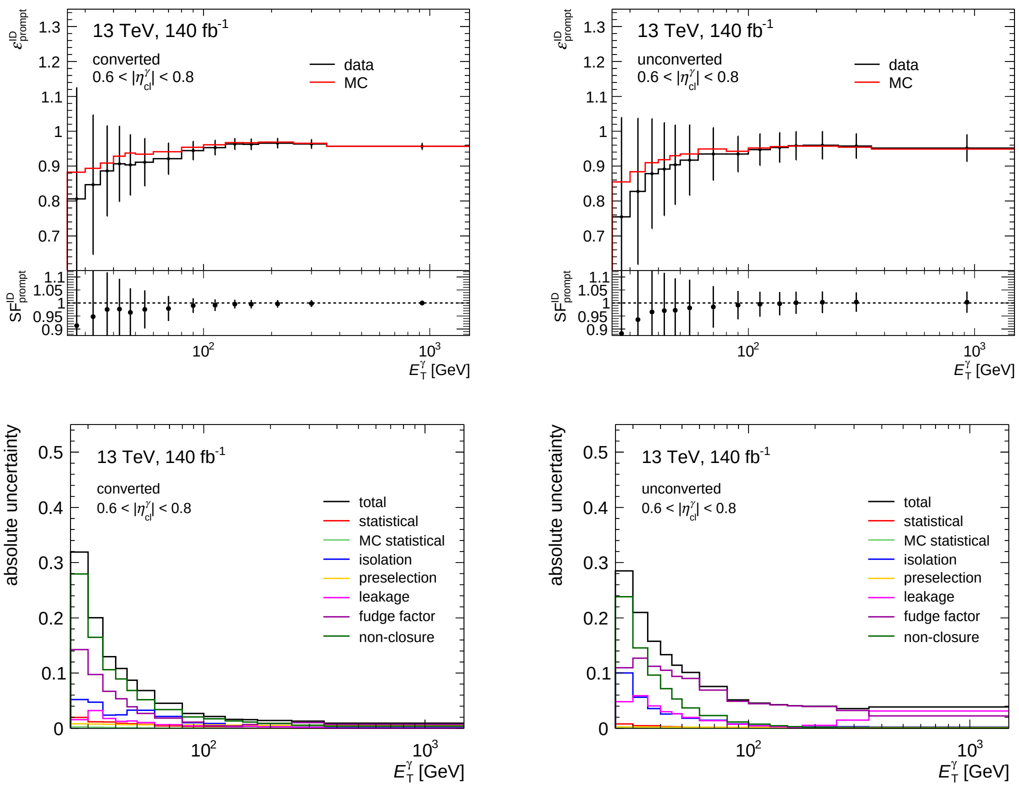

Figure B.1: Prompt photon identification efficiencies with total uncertainties in data and simulation and resulting scale factors for $0.6 < |\eta_{\mathrm{cl}}^{\gamma}| < 0.8$ (upper row) for converted photons (left) and unconverted photons (right). Corresponding breakdowns of individual uncertainties in the lower row.

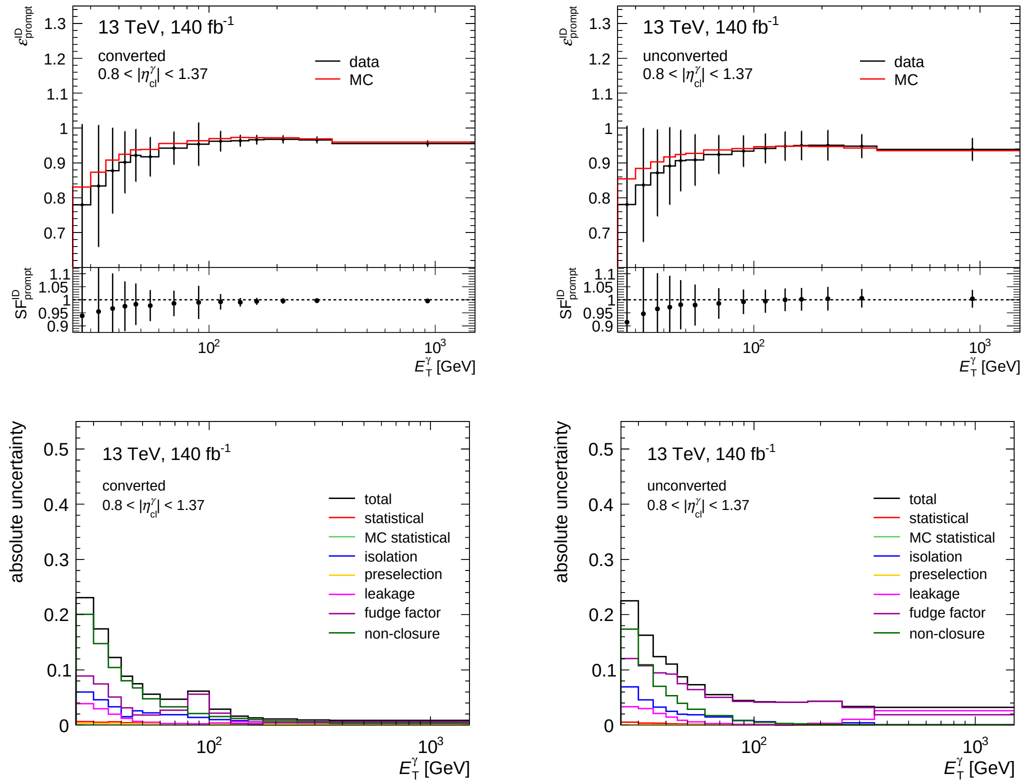

Figure B.2: Prompt photon identification efficiencies with total uncertainties in data and simulation and resulting scale factors for $0.8 < |\eta_{\mathrm{cl}}^{\gamma}| < 1.37$ (upper row) for converted photons (left) and unconverted photons (right). Corresponding breakdowns of individual uncertainties in the lower row.

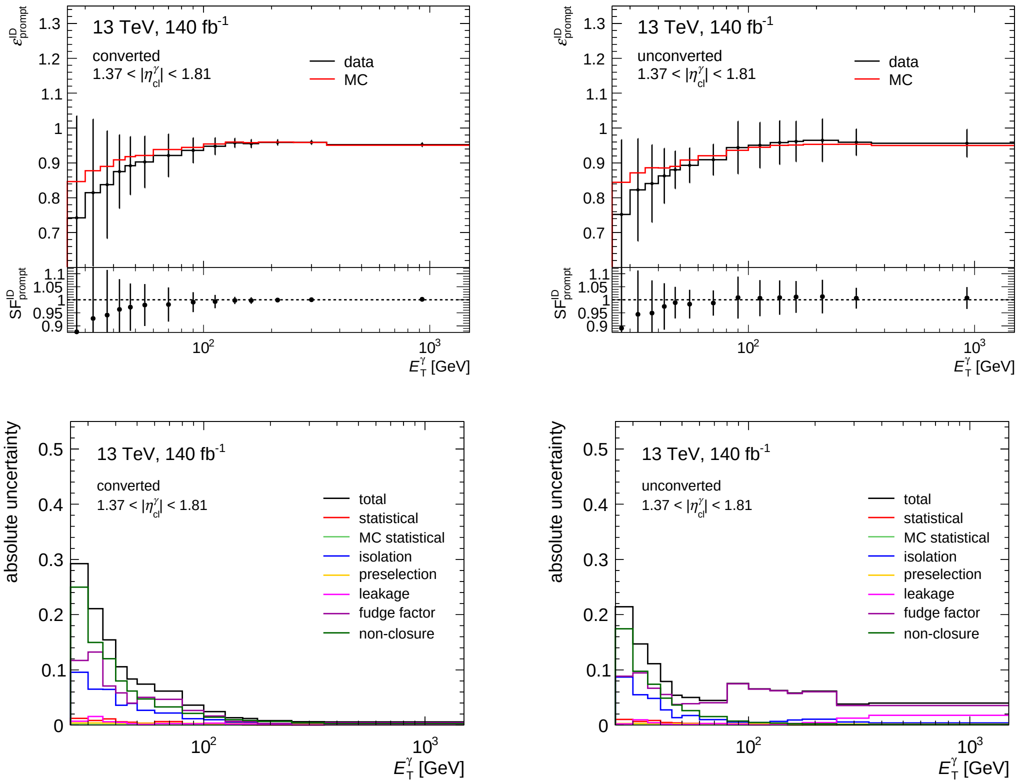

Figure B.3: Prompt photon identification efficiencies with total uncertainties in data and simulation and resulting scale factors for $1.52 < |\eta^{\gamma}_{\mathrm{cl}}| < 1.81$ (upper row) for converted photons (left) and unconverted photons (right). Corresponding breakdowns of individual uncertainties in the lower row.

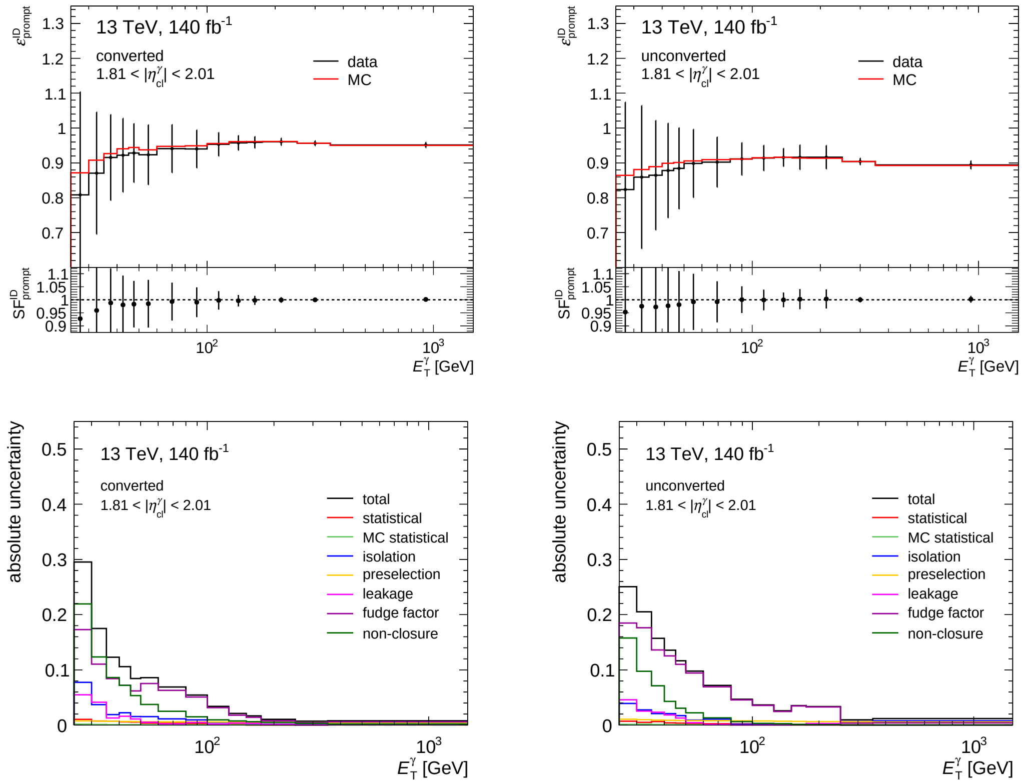

Figure B.4: Prompt photon identification efficiencies with total uncertainties in data and simulation and resulting scale factors for $1.81 < |\eta_{cl}^{\gamma}| < 2.01$ (upper row) for converted photons (left) and unconverted photons (right). Corresponding breakdowns of individual uncertainties in the lower row.

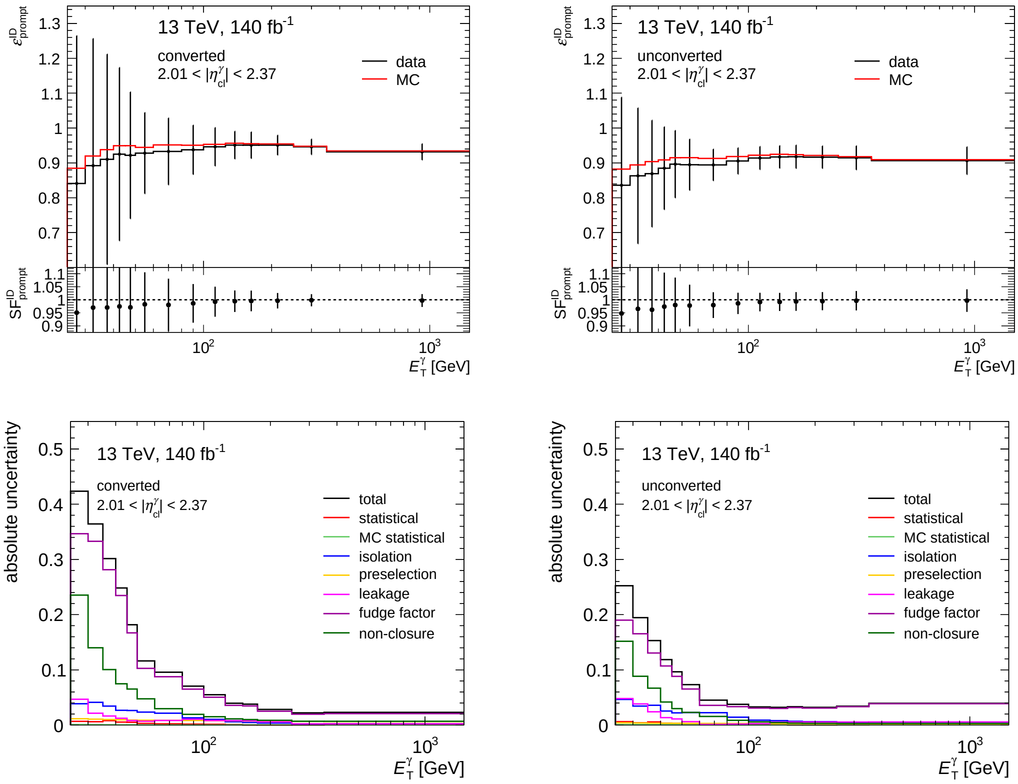

Figure B.5: Prompt photon identification efficiencies with total uncertainties in data and simulation and resulting scale factors for $2.01 < |\eta_{\text{cl}}^{\gamma}| < 2.37$ (upper row) for converted photons (left) and unconverted photons (right). Corresponding breakdowns of individual uncertainties in the lower row.

C Estimation of background contribution from non-prompt photons as well as hadrons misidentified as photons

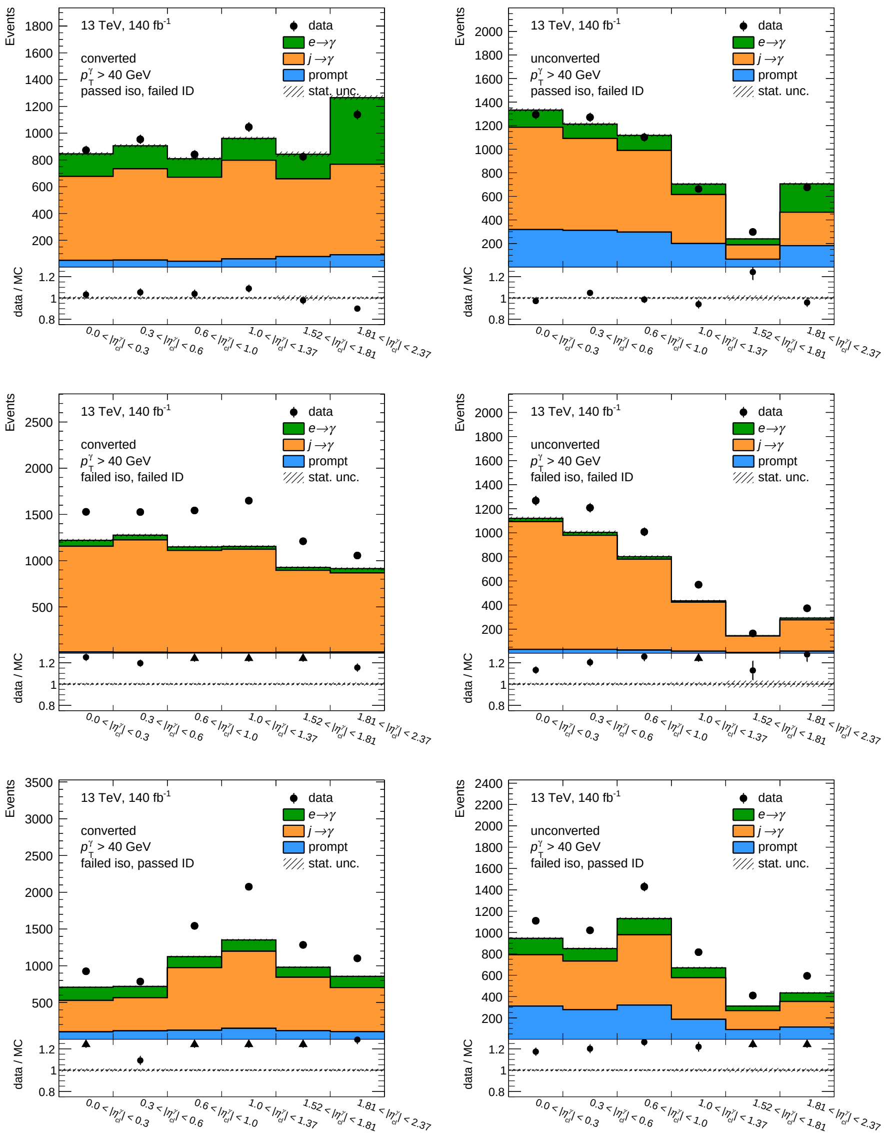

Figure C.1: Distributions of $|\eta^{\gamma}_{\text{cl}}|$ in the background regions (A, B, C) for converted (top) and unconverted photons (bottom). The error bands represent statistical uncertainties.

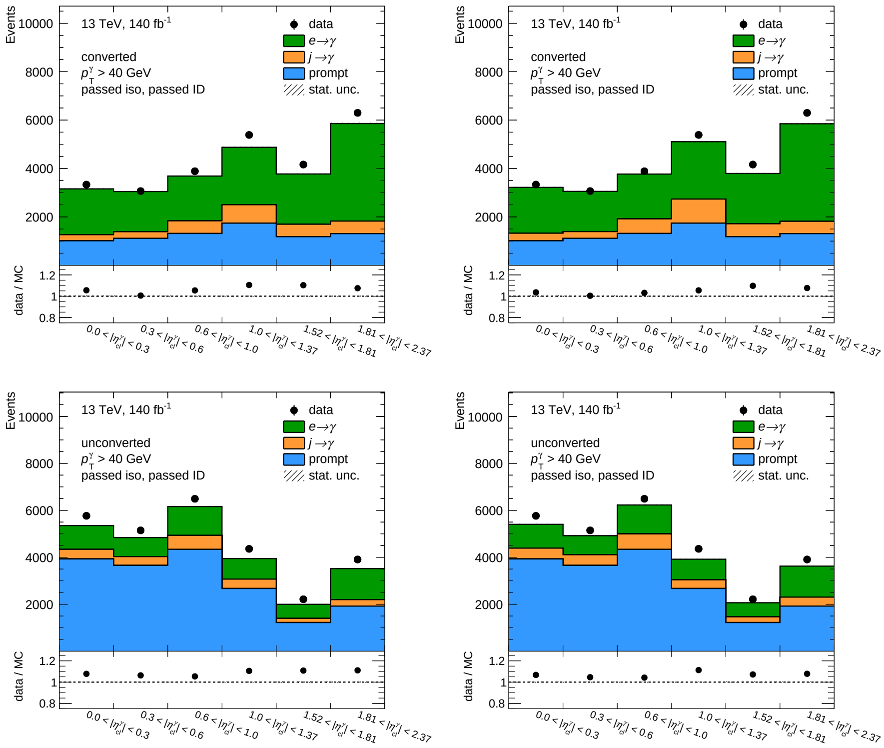

Figure C.2: Distributions of $|\eta^\gamma_{\mathrm{cl}}|$ in the target region (D) for converted (top) and unconverted photons (bottom) before applying the $h\to\gamma$ scale factors (left) and after applying them (right). The error bands represent statistical uncertainties.

Danksagung

Ich danke Herrn Prof. Kröninger für die Betreuung dieser Arbeit sowie für die Möglichkeit, sie in einem sehr angenehmen Arbeitsumfeld durchzuführen. Ebenso danke ich Chris Delitzsch für die Übernahme des Zweitgutachtens. Mein besonderer Dank gilt Andrea Knue und Tomas Dado für die kontinuierliche Unterstützung, das Mutmachen (auch an Jens Weingarten!), die vielen hilfreichen Diskussionen, die geduldige Begleitung und das Feedback während des gesamten Projekts. Lucas danke ich für die enge Zusammenarbeit und den Austausch im Rahmen der Analyse. Ich danke der ATLAS-Kollaboration für die Bereitstellung der Daten und die Rahmenbedingungen dieser Arbeit. Weiterhin danke ich allen Kolleg:innen der Arbeitsgruppe für die schöne Atmosphäre, viele klasse Bergfeste, sowie insbesondere Andrea, Björn, Donna, Julia, Lasse, Lucas, Salvo, Till und Tomas für das Korrekturlesen dieser Arbeit. Ein besonderer Dank gilt außerdem Andrea Teichmann und Mike für die organisatorische Unterstützung und den zusätzlichen Austausch. Ihr seid natürlich das Herz des Lehrstuhls! Ich danke meinen Freunden für den Ausgleich und die Unterstützung während dieser Zeit. Ganz besonders danke ich meiner Familie und meiner Freundin für ihre Geduld und ihren Rückhalt.